Dissertation
submitted to the
Combined Faculties for the Natural Sciences and for Mathematics
of the Ruperto-Carola University of Heidelberg, Germany
for the degree of
Doctor of Natural Sciences

presented by
Diplom-Physiker Peter Schuller
born in Bucharest
Oral examination: 16th October 2002

Calibration of MIDI,
the Mid-infrared Interferometer for the VLTI

Referees: **Prof. Dr. Christoph Leinert**
Prof. Dr. Wolfgang Duschl

Abstract

Calibration of MIDI, the Mid-infrared Interferometer for the VLTI

MIDI is the MID-infrared Interferometric Instrument at the Very Large Telescope Interferometer (VLTI). It will perform long-baseline stellar interferometry in the N band (8…13 µm). In the run-up of setting up MIDI, some preparatory tasks had to be solved concerning the calibration of the instrument in the laboratory. Being a crucial sub-system of MIDI, the Internal Delay Line was thoroughly tested in order to characterise its performance. Light sources for different purposes were provided and equipped with appropriate optical layout. Spectral references were also included. The interrelation of a calibrated Internal Delay Line and spectral calibration is presented.

For calibration of the instrument during observations, calibrator stars are used. As part of the selection process of suitable objects for a database of such stars, a sub-sample of candidates was checked by interferometric observations in the K′ band (2.0…2.3 µm). Special attention was payed to differential effects in narrow sub-bands.

The potential of stellar interferometry is shown in the case of some late type stars. High spatial resolution data were used to constrain model parameters of the circumstellar envelopes of these objects.

Zusammenfassung

Kalibration von MIDI, dem Mittelinfrarot-Interferometer für das VLTI

Das MIDI-Instrument (MID-infrared Interferometric Instrument) wird am VLTI (Very Large Telescope Interferometer) stellare Langbasisinterferometrie im N-Band (8…13 µm) durchführen. Im Vorfeld des Aufbaus von MIDI waren einige vorbereitende Aufgaben zu lösen, die die Kalibrierung des Instruments im Labor betrafen. Die interne Verzögerungsstrecke, die eine wesentliche Untereinheit von MIDI darstellt, wurde sorgfältig getestet, um Aussagen über deren Güte zu treffen. Lichtquellen für verschiedene Zwecke wurden bereitgestellt und mit geeigneten Optiken versehen. Spektrale Referenzen wurden ebenfalls einbezogen. Die Wechselbeziehung zwischen einer kalibrierten Verzögerungsstrecke und spektraler Kalibration wird aufgezeigt.

Zur Kalibration des Instruments während der Beobachtung werden Kalibratorsterne benutzt. Als Teil des Auswahlverfahrens von geeigneten Objekten für eine Datenbank von solchen Sternen wurde eine Auswahl von Kandidaten durch interferometrische Beobachtungen im K′-Band (2.0…2.3 µm) überprüft. Besonderes Augenmerk wurde dabei auf unterschiedliches Verhalten in schmalen Teilbändern gelegt.

Die Möglichkeiten stellarer Interferometrie werden am Beispiel einiger Sterne späten Types aufgezeigt. Daten mit hoher räumlicher Auflösung wurden benutzt, um Modellparameter der zirkumstellaren Hüllen dieser Objekte einzugrenzen.

A motto for scientists:
"Great are the works of the LORD*;*
They are studied *by all who delight in them."*
(The Bible, Psalm 111:2)

Ein Motto für Wissenschaftler:
„Groß sind die Werke des HERRN*;*
wer sie erforscht*, der hat Freude daran."*
(Die Bibel, Psalm 111, 2)

Contents

List of Figures

List of Tables

Chapter 1

Introduction

1.1 Historical Remarks and Overview

Throughout the history of astronomy, technical advancements were driven by the desire to look at celestial objects closer and even closer or, to put it in modern scientific terms, with higher spatial resolution. Up to the beginning of the seventeenth century, mechanical devices like sextants were used to measure positions on the sky. Representative of this era, one might name *Tycho Brahe* (1546 - 1601) who developed his well-known mural quadrant and performed some of the most precise and substantial astronomical observations of his time. A big step forward in observational techniques was initiated when optical devices were used for astronomical purpose for the first time. This fundamental change in instrumentation is usually associated with the name of *Galileo Galilei* (1564 - 1642). In 1609, he applied strong improvements to prototype telescopes originally invented in the Netherlands[1]. It was up to *Johannes Kepler* (1571 - 1630) to penetrate both the astronomical observations and the new technique with theory and thorough calculations, leading to the three Kepler Laws and a comprehensive treatment of the optics known at that time. This triumvirate might be regarded as prototypical for a fruitful linkage of instrumentation, observation, and theory in astronomy.

Ever since, telescopes have been improved and grown in size in order to see increasingly resolved details on the sky. However, every enlargement of the optics and mechanics involved had to be traded for technical feasibility that was and is possible at a time. And still for a long time stars remained unresolved. Yet, in 1868 *Armand Fizeau* (1819 - 1896) suggested an interferometric method to measure stellar diameters by placing a mask with two holes in front of a telescope's aperture (Fizeau, 1868). He had calculated that the resulting interferometric fringes would vanish at a separation related to the size of the star. The first successful application of interferometry to astronomy was performed by *Albert Michelson* (1852 - 1931) in 1891 by measuring the diameter of Jovian moons (Michelson, 1891). Not until 1920 did Michelson also apply this method to stars which revealed for the first time the angular and, knowing its parallax, the linear diameter of a giant star (Michelson and Pease, 1921). For these measurements, Michelson used a setup that would become a major principle for modern stellar interferometry. On a very rigid bearing construction fixed to the aperture of the largest available telescope, he placed two independent mirrors at a distance exceeding the telescope's diameter. Their light was combined at a point where the paths of the produced beams were well matched, i.e., in

---

[1] There are, though, earlier reports of stellar observations in 1608, made mainly out of curiosity by Dutch lens makers. The first lunar drawings appeared in England made by *Thomas Harriot* in summer 1609 (Helden, 1995).

the telescope's focal plane. Even though Michelson still performed the combination by means of one telescope, this setup can be considered the first step beyond astronomy with monolithic telescopes.

The field remained widely dormant, largely due to technological demands that were to be solved for a further extension. But beginning in the 1950s the issue of interferometry in astronomy was under study once again. Radio interferometry was introduced (Ryle, 1952) which does not suffer from the difficulties governing optical interferometry. Interferometry at radio wavelengths is a well-established technique and presently an active area of research (Thompson et al., 2001; Finley and Goss, 2000). Likewise, the technique of intensity interferometry was developed and demonstrated at optical wavelengths, using for the first time two independent telescopes (Hanbury Brown and Twiss, 1956b,a). Compared with Michelson's amplitude interferometer this technique had the advantages of being less demanding in mechanical respect and of being essentially unaffected by seeing, i.e., moving and spreading of a star's image due to atmospheric turbulence.

Then in the 1970s it was demonstrated that the technological demands on mechanical stability, which is necessary for performing Michelson's experiment with two separate telescopes, had become solvable (Labeyrie, 1975). With this kind of interferometer a sensitivity much higher than with an intensity interferometer was obtainable. Starting in the 1970s, a number of optical interferometers were established, using different techniques of beam combination. Today, there are several long baseline stellar interferometers in operation mainly working at visible and near-infrared wavelengths (CHARA, COAST, GI2T, IOTA, NPOI, PTI, SUSI; see Léna and Quirrenbach (2000), Session 3, for update reports). In the mid-infrared regime, there is the heterodyne interferometer ISI (Hale et al., 2000), mixing the telescope beams with light from a reference laser working at 11 µm.

And again, building on their experience, upcoming interferometers which are currently being constructed (VLTI, KECK (Léna and Quirrenbach, 2000, Sessions 1 and 2), also LBT and OHANA (Léna and Quirrenbach, 2000, Session 3)) will take a further step in technological refinement to open an even "sharper view of the stars" (Hajian and Armstrong, 2001). They will provide high spatial resolution with unprecedented sensitivity towards faint objects. In this way many more objects will be observable interferometrically and also new classes of objects. Future projects (DARWIN, SIM) are already planned to carry out interferometry in space (Léna and Quirrenbach, 2000, Session 4). An overview of the current status of optical interferometry is presented by Quirrenbach (2001). A comprehensive collection of online resources is found at the OLBIN website (see bibliography).

The Very Large Telescope (VLT) project of the European Southern Observatory (ESO) is currently being established on Mount Paranal in Chile (Appenzeller, 2001). Four telescopes with a diameter of 8 m are installed and will gradually be equipped with a variety of optical imaging and spectrometric systems covering the visible, near-infrared, and mid-infrared wavelength range. Apart from being used individually, these telescopes will also be combined to form the Very Large Telescope Interferometer (VLTI). Together with presently three additional 1.8-m telescopes, this facility will have a spatial resolution corresponding to a 200-m telescope. Like the VLT, also the VLTI beam combining instruments will eventually cover a wide optical range. One of these instruments will be MIDI, the MID-infrared Interferometric Instrument. It will allow access to a wavelength range which until now remains largely unexplored by interferometry, yet where many interesting astrophysical processes can be observed, e.g., the circumstellar environments of young and evolved stars (see section 3.2.1). MIDI will be complemented by the VLT Imager and Spectrometer for the mid-InfraRed (VISIR) in the photometric regime and by the Astronomical Multiple BEam Recombiner (AMBER) as a near-infrared interferometer. Also the CONICA camera will be an important complement, allowing observations up to wavelengths almost reaching the regime of MIDI. These new instruments will be an excellent set of tools to observe again closer, find challenging astrophysics, and so further explore the universe.

1.2 Outline of Thesis

In Chapter 2, a brief introduction to long baseline stellar interferometry is given as far as the MIDI instrument is concerned. A few resulting aspects of the expected signal in MIDI are discussed in sections 2.3 and 3.2. As MIDI will be closely linked with the VLTI, the main sub-systems of the VLTI are outlined in section 3.1 together with short descriptions of the other interferometric instruments. The MIDI instrument itself with its sub-units is described in section 3.3.

The overall framework of this work was the calibration of MIDI. Testing and characterising the Internal Delay Line (IDL), as crucial sub-unit of MIDI, was one task whose results are presented in section 4.2. Another group of sub-units is the calibration equipment. Section 4.3 shows a further task which was to design and provide narrow and broad band light sources that would be used for laboratory testing and also partly on Paranal. For the narrow band source, a backup system was successfully searched and provided. For a spectral calibration, related means were added which are described in section 4.4. The principles of laboratory calibration methods should be demonstrated inasmuch the general status of the project would allow it. A calibration routine is proposed in section 4.5.

During observations, instrumental and atmospheric conditions will be calibrated by taking measurements on calibrator stars. These are objects with well-known properties stored in a database. Preparatory interferometric measurements were taken and are described in section 5.1.

An example of applying interferometry to an astronomical subject is given in section 5.2. Interferometric data taken at different wavelengths on late type stars are compared to the output of a radiation transfer model considering spherical dust envelopes. Thus, object parameters are constrained and limitations of such models are outlined.

Chapter 2

Aspects of Stellar Interferometry

This chapter contains an overview of some aspects of stellar interferometry. It will focus on issues that are relevant to the MIDI instrument. The goal is to describe the basic form of the expected interferogram. A comprehensive introduction to this field can be found, for example, in Lawson (2000).

2.1 Principles – Monochromatic Unresolved Source

Instrumental Setup Figure 2.1 depicts the principle of stellar interferometry with two independent telescopes. Two telescopes, spanning the baseline vector $\mathbf{B}$, are pointed in direction $\mathbf{n}$ towards a source on the sky. Since this source is a great distance away, and therefore considered to be unresolved or "point-like" for the interferometer, the incoming light may be regarded as arriving in plane wavefronts with the wave vector $\mathbf{k_0}$ where $|\mathbf{k_0}| = k_0 = 2\pi/\lambda_0$ is the wave number[1] and λ_0 the wavelength. Therefore, $\mathbf{n}$ is the negative, normalised wave vector of the incident plane wave, i.e., $\mathbf{n} = -\mathbf{k_0}/k_0$.

The two aperture A1 and A2 each collect a certain section from these wavefronts. The resulting beams are directed by guiding optics towards a beam combination unit where the beams are mixed and therefore interference is produced. This unit may have different configurations depending, for example, on whether the beams are combined in an image plane or in a pupil plane of the telescopes. In an image plane interferometer, the sky is imaged on a detector where the beams are interfered. This will be the case, for example, for the AMBER instrument at the VLTI and the LINC-NIRVANA interferometer on the LBT. In contrast, in a pupil plane interferometer like MIDI, images of the telescope pupils are overlapped and thus interfered (see Figure 2.2).

Another aspect is the direction in which the interfering beams propagate while they are mixed. Co-axial beams are mixed while propagating in the same direction whereas multi-axial beams propagate in different directions. A pupil plane interferometer with a multi-axial setup shows spatially detectable interferometric fringes, whereas a co-axial setup yields a flat tint. In this case, the interferometric modulation is achieved by a variation of the Optical Path Difference (OPD) between the beams (see below).

MIDI is a co-axial pupil plane interferometer, with the detection taking place in the image plane. All the following considerations are specialised for the MIDI case.

---

[1] Apart from a factor $(c/2\pi)$, the wave number corresponds to the wave frequency $\nu_0 = c/\lambda_0$ (c: speed of light).

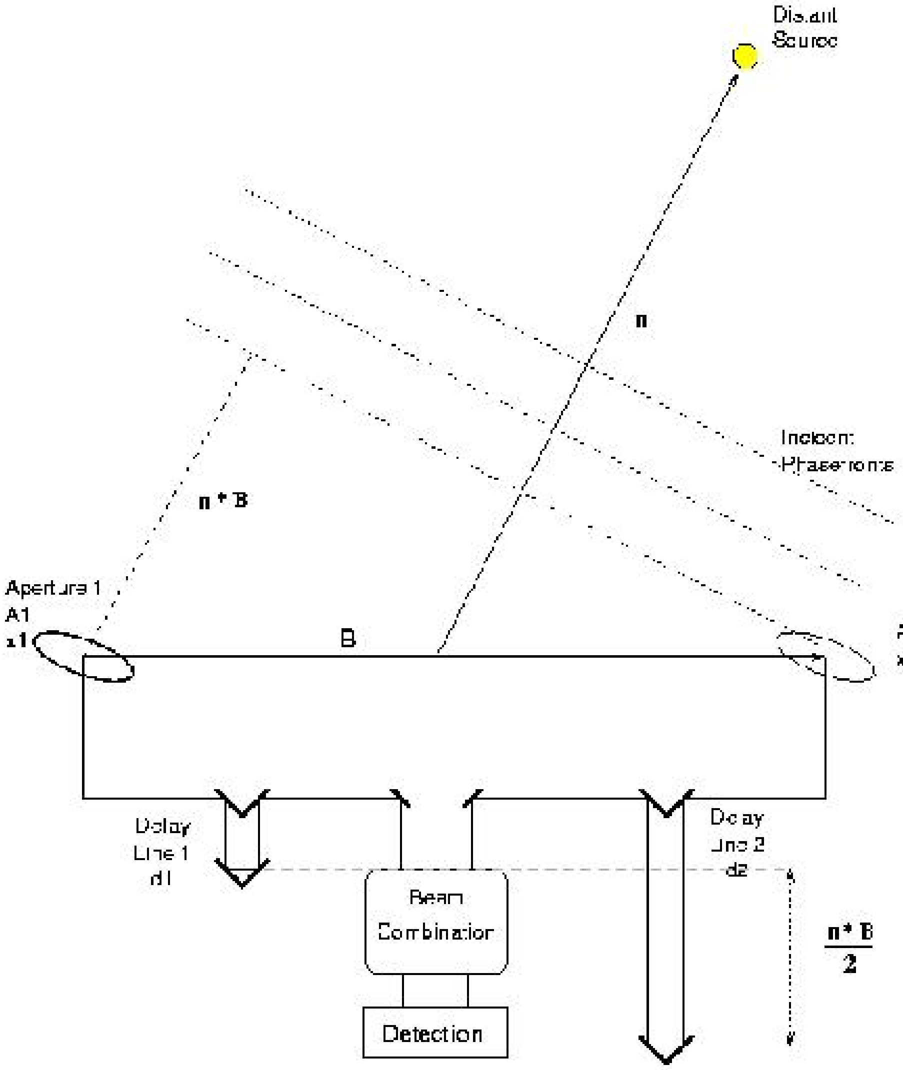

Figure 2.1: Principle of stellar interferometry with two independent telescopes. *Two telescopes collect light of a source which is directed towards a beam combination unit. The Optical Path Difference between the beams is equalised by Delay Lines. The resulting interference pattern contains information about the observed object. (Drawing adapted from Boden (2000))*

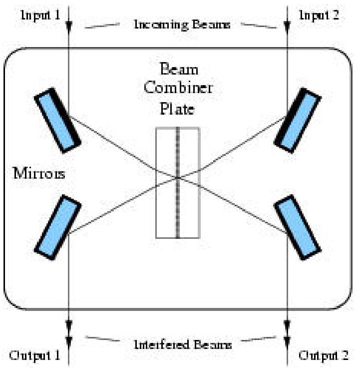

Figure 2.2: Pupil plane beam combiner. *The beam combiner plate contains a thin beam splitter layer of symmetric behaviour, i.e., an incident beam is treated the same no matter from which side it occurs. In this drawing, it is assumed that the layer is sandwiched by two glass plates.*

Light Waves and Interference Let the complex number $\mathbf{E}$ denote the electro-magnetic wave associated with a beam emerging from the beam combiner into one interferometric output, with $\hat{E}$ being its modulus and ϕ the phase. $\mathbf{E}$ contains the reflected fraction $\mathbf{E_r}$ from the corresponding input beam and the transmitted part $\mathbf{E_t}$ of the other beam. For example, if one looks at Output 1 in Figure 2.2, it contains a reflected fraction of Input 1 and a transmitted part of Input 2. If $\hat{E}_r$, $\hat{E}_t$, ϕ_r and ϕ_t are the respective moduli and phases, $\mathbf{E}$ can be written as

$$\mathbf{E} = \mathbf{E_r} + \mathbf{E_t} \quad \text{with} \quad \mathbf{E_r} = \hat{E}_r \cdot \exp(i\phi_r) \quad \text{and} \quad \mathbf{E_t} = \hat{E}_t \cdot \exp(i\phi_t). \tag{2.1}$$

As mentioned before, this description concentrates on interference of the incoming beams that are collected from the same incoming wavefront (see Figure 2.1). Losses and phase shifts that are *common* in both beams are not considered for this purpose. Therefore, it is possible to choose one of the beams as a reference and assign to the other beam all *relative* differences between the beams, that might be introduced by various effects.

The following effects will be considered explicitly:

- An important aspect are atmospheric effects that introduce relative perturbations, which are accounted by a relative atmospheric transfer function

  $$\mathbf{T_a} = T_a \cdot e^{i\phi_a}, \tag{2.2}$$

  where T_a is its modulus and ϕ_a its phase.

  Writing $\mathbf{T_a}$ in this form assumes that the dominant effects of the atmosphere are extinction and the piston effect (see section 3.2.3). In particular, relative spatial fluctuations of phase across the aperture pupil do not enter. This assumption is legitimate when the aperture size is clearly smaller than the scale length r_0 of the atmospheric turbulence, or the phase fluctuations were corrected by spatial filtering or the application of an Adaptive Optics (AO) system.

- In each optical train there is a movable mirror which together with some fixed mirrors forms an optical delay line (see Figure 2.1). If the movable mirror is at a distance d away from its zero position, and one assumes a double-pass optical train, an additional optical path of $2d$ is introduced. The total Optical Path Difference (OPD), introduced by purely geometric differences between beam 1 and 2, is then

  $$OPD = \mathbf{n} \cdot \mathbf{B} + 2(d_1 - d_2) \equiv \delta. \tag{2.3}$$

  The corresponding phase shift ϕ_{geom} leads to the complex factor

  $$f_{geom} = e^{i\phi_{geom}} \quad \text{with} \quad \phi_{geom} = -k_0 \cdot \delta. \tag{2.4}$$

- Instrumental properties that introduce stationary differences between the two beams (e.g., different aperture sizes or bulky optics, like the entrance window, traversed by the beams) can be described by a relative instrumental transfer function

  $$\mathbf{T_i} = T_i \cdot e^{i\phi_i} \tag{2.5}$$

  in analogy to the relative atmospheric transfer function.

- In particular, the effect of the beam combiner as the central part of an interferometer is described separately by the number

  $$\mathbf{T_{bc}} = T_{bc} \cdot e^{i\phi_{bc}}. \tag{2.6}$$

  The beam combiner is assumed to be a thin beam splitter layer of symmetric behaviour, i.e., incident beams are treated the same no matter from which side they occur.

Now let $\mathbf{E_r}$ be the reference beam. It follows for the individual contributions in the overlapped beam

$$\begin{aligned} \mathbf{E_r} &= \hat{E}_r \cdot \exp(i\phi_r), \\ \mathbf{E_t} &= \hat{E}_t \cdot \exp(i\phi_t) \;=\; \mathbf{E_r} \cdot f_{geom} \mathbf{T_a} \mathbf{T_i} \mathbf{T_{bc}} \\ &= \hat{E}_r \cdot T_a T_i T_{bc} \cdot \exp[i(\phi_r + \phi_{geom} + \phi_a + \phi_i + \phi_{bc})] \end{aligned} \tag{2.7}$$

and thus for the total interfered beam

$$\mathbf{E} = \mathbf{E_r} + \mathbf{E_t} = \hat{E}_r \exp(i\phi_r) \cdot [1 + T_i T_a T_{bc} \cdot \exp(i(-k_0\delta + \phi_a + \phi_i + \phi_{bc}))]. \tag{2.8}$$

The measured signal power P in this interferometric output is therefore

$$P = \mathbf{E} \cdot \mathbf{E}^* = \hat{E}_r^2 \cdot [1 + T_i^2 T_a^2 T_{bc}^2 + 2\, T_i T_a T_{bc} \cdot \cos(k_0\delta - \phi_a - \phi_i - \phi_{bc})]. \tag{2.9}$$

Specialisations For simplification, it may be assumed that the atmosphere only introduces disturbances in phase, i.e., $T_a = 1$. Further, let the design of the two optical paths be ideally matched so that $\mathbf{T_i} = 1$ and $T_{bc} = 1$, the latter implying that the beam splitter exactly halves the incident beams. Then, the power P_0 collected by one aperture of area A from the incoming flux density $F_0 = F(\lambda_0)$ is $P_0 = AF_0 = 2\hat{E}_r^2$. With these simplifications, equation (2.9) becomes

$$P = AF_0 \cdot [1 + \cos(k_0\delta - \phi_a - \phi_{bc})] = P_0 \cdot [1 + \cos(k_0\delta - \phi_a - \phi_{bc})], \quad [P] = 1\,\mathrm{W}. \tag{2.10}$$

For pupil plane interferometers, this last expression can be further evaluated. If the OPD δ is adjusted to zero, then by the symmetry of the interferometer, both interfered output beams should contain equal energy. Changing the OPD will increase the output power of one beam while the other beam will be decreased by the same amount so that the total amount of energy is conserved. This can be explained by the fact that a thin, symmetric beam combiner introduces a phase difference of exactly $|\phi_{bc}| = \pi/2$ between reflected and transmitted beams (Traub, 2000) which also accounts for the complementarity of the two beams.

Therefore, it follows with $\phi_{bc} = \pi/2$ for the power contained in one interferometric output

$$P_+ = AF_0 \cdot [1 + \sin(k_0\delta - \phi_a)] = P_0 \cdot [1 + \sin(k_0\delta - \phi_a)] \tag{2.11}$$

and, in analogy, for the complementary output

$$P_- = AF_0 \cdot [1 - \sin(k_0\delta - \phi_a)] = P_0 \cdot [1 - \sin(k_0\delta - \phi_a)]. \tag{2.12}$$

This means that, when changing the OPD, brightness cycles will be observable in the two outputs. Constructive interference will appear in one output and after an OPD step of $\lambda_0/2$ in the other one. The full modulation corresponds to the total power $2P_0$ collected by the telescopes.

2.2 Application – Polychromatic Extended Source

2.2.1 General Case

Real astronomical objects have a certain extent on the sky occupying a solid angle Ω. The modified observation vector $\mathbf{n}' = (\mathbf{n} + \mathbf{\Delta n})$ varies with the offset $\mathbf{\Delta n}$ on the sky perpendicular to the pointing direction $\mathbf{n}$. From equation (2.3), the OPD is now given by

$$OPD' = (\mathbf{n} + \mathbf{\Delta n}) \cdot \mathbf{B} + 2(d_1 - d_2) = \mathbf{\Delta n} \cdot \mathbf{B} + \delta. \tag{2.13}$$

Likewise, the brightness distribution may vary with position on the sky and wave number so that it should be written as $F_s(\mathbf{n} + \mathbf{\Delta n}, k)$ ($[F_s] = \mathrm{W\,m^{-2}\,\mu m\,sr^{-1}}$). Because the projected area collecting light also changes with the offset from the pointing direction, it has to be written $A(\mathbf{n} + \mathbf{\Delta n})$. Another instrument specific may be a response function $\eta(k)$ that is given by spectral filtering behaviour.

In order to derive equation (2.11), the interferogram of a single unresolved 'point' source radiating at wavelength λ_0 was calculated. Having now an extended source, one can consider it as compound of many mutually independent point sources. Furthermore, it can be shown that mixed electric fields of several monochromatic components are incoherent (Born and Wolf, 1999, Section 7.5.8). Therefore, one can integrate over all positions of point sources and their spectral range. In general[2], equation (2.11) then reads (where the index is dropped):

$$\begin{aligned} P(\mathbf{n}, \mathbf{B}, \delta) &= \int dk\, \eta(k) \int_{\mathbf{\Delta n}} d\Omega\, A(\mathbf{n} + \mathbf{\Delta n}) F_s(\mathbf{n} + \mathbf{\Delta n}, k) \cdot [1 + \sin(k \cdot OPD' + \phi_a)] \qquad (2.14) \\ &= P_0 + \int dk\, \eta(k) \int_{\mathbf{\Delta n}} d\Omega\, A(\mathbf{n} + \mathbf{\Delta n}) F_s(\mathbf{n} + \mathbf{\Delta n}, k) \cdot \sin(k(\mathbf{\Delta n} \cdot \mathbf{B} + \delta) + \phi_a). \end{aligned}$$

P_0 is the total power collected by one telescope:

$$P_0 = \int dk\, \eta(k) \int_{\mathbf{\Delta n}} d\Omega\, A(\mathbf{n} + \mathbf{\Delta n}) F_s(\mathbf{n} + \mathbf{\Delta n}, k). \tag{2.15}$$

At this point, one can introduce the *correlated flux density* $\mathbf{C}$ of the brightness distribution F_s and the aperture function A as

$$\mathbf{C}(\mathbf{n}, \mathbf{B}, k) = Ce^{i\psi} = \int_{\mathbf{\Delta n}} d\Omega\, A(\mathbf{n} + \mathbf{\Delta n}) F_s(\mathbf{n} + \mathbf{\Delta n}, k)\, e^{-ik\mathbf{\Delta n} \cdot \mathbf{B}}, \tag{2.16}$$

where C is the modulus and ψ the complex phase with the phase reference at $\mathbf{n}$. It should be noted that the expression for $\mathbf{C}$, which is the response of the interferometer in a certain configuration, describes a two-dimensional Fourier transformation of the aperture efficiency weighted brightness distribution on the sky. This could also be expected from the *van Cittert-Zernike Theorem* in the case of an incoherent source and in small-field approximation, as it is usually present in astronomy.

It is useful to normalise $\mathbf{C}$ by the spectral power P_k received at a certain wave number from the whole source, i.e.,

$$P_k = \int_{\mathbf{\Delta n}} d\Omega\, A(\mathbf{n} + \mathbf{\Delta n}) F_s(\mathbf{n} + \mathbf{\Delta n}, k) \quad , \quad [P_k] = \mathrm{W\,\mu m}. \tag{2.17}$$

---

[2] Note the simplifications leading to equation (2.11).

This normalisation yields the *complex*[3] *visibility* $\mathbf{V}$:

$$\mathbf{V}(\mathbf{n}, \mathbf{B}, k) = \frac{\mathbf{C}}{P_k} = \frac{Ce^{i\psi}}{P_k} = Ve^{i\psi}. \tag{2.18}$$

Written in this form, the visibility $\mathbf{V}$ is independent of intrinsic instrumental properties, except of course the baseline used, and characteristic for the object under study.

Introducing $\mathbf{V}$ in equation (2.14) yields

$$\begin{aligned} P(\mathbf{n}, \mathbf{B}, \delta) &= P_0 - \int dk\ \eta(k)\ \Im\{\mathbf{C}e^{-i\phi_a}e^{-ik\delta}\} \\ &= P_0 + \int dk\ \eta(k)\ P_k V(\mathbf{n}, \mathbf{B}, k) \cdot \sin(k\delta + \phi_a - \psi). \end{aligned} \tag{2.19}$$

2.2.2 Uniform Disk

In order to evaluate equation (2.19) in a more concrete case, one can assume a circular disk source on the sky with angular diameter Θ and spatially uniform brightness distribution F_s. Furthermore, F_s is assumed as constant over the spectral range of the instrument and evaluated at a wave number k_0 which is an effective wave number averaging the spectral behaviour of the intensity distribution of the source (Hanbury Brown et al., 1974, and references therein) (see below). Likewise, Θ should be sufficiently small, so the aperture function may be regarded as constant. Thus, if ρ is the angular distance from the centre of the source, the assumptions read

$$F_s(\rho \leq \Theta/2, k_0) = F_0 \quad \text{and} \quad A(\mathbf{n} + \mathbf{\Delta n}) = A_0, \tag{2.20}$$

so that the spectral power P_k contained at k_0 is

$$P_{k_0} = F_0 \cdot A_0 \cdot \pi(\Theta/2)^2, \quad [P_{k_0}] = \mathrm{W\,\mu m}. \tag{2.21}$$

Under these assumptions, it can be shown (Boden, 2000) that the correlated flux density for a uniform disk (UD) is

$$\mathbf{C}^{UD}(\Theta, B_\perp, \lambda_0 = 2\pi/k_0) = C^{UD} \cdot e^{i\psi^{UD}} = P_{k_0}\frac{2J_1(\pi\Theta B_\perp/\lambda_0)}{\pi\Theta B_\perp/\lambda_0} \cdot e^{i\psi^{UD}}, \tag{2.22}$$

where $B_\perp$ is the baseline projected in the direction of observation. J_1 is the so-called first-order Bessel function of the first kind. The visibility is then given through equation (2.18) by

$$\mathbf{V}^{UD}(\Theta, B_\perp, \lambda_0) = V^{UD} \cdot e^{i\psi^{UD}} = \frac{2J_1(\pi\Theta B_\perp/\lambda_0)}{\pi\Theta B_\perp/\lambda_0} \cdot e^{i\psi^{UD}}. \tag{2.23}$$

As the light has to pass through the atmosphere, the interferometer detects in principle $\mathbf{C}^{UD} \cdot e^{-i\phi_a} = P_{k_0}V^{UD} \cdot \exp[i(\psi^{UD} - \phi_a)]$, which enters into equation (2.19). Yet, by the turbulent nature of the atmosphere changing the phase ϕ_a randomly and thus corrupting the phase information, the phase factor $\exp[i(\psi^{UD} - \phi_a)]$ is not defined. Therefore, with a two beam stellar interferometer it is usually only possible to access the modulus $P_{k_0}V^{UD}$ of the complex visibility. Figure 2.3 shows the absolute value $|V^{UD}|$ of the modulus of the visibility as a function of its argument $(\Theta B_\perp/\lambda_0)$ which can be thought of the source diameter Θ in units of $(\lambda_0/B_\perp)$.

Inserting these findings in equation (2.19) yields

$$P(\mathbf{n}, \mathbf{B}, \delta) = P_0 + P_{k_0}\left|\frac{2J_1(\pi\Theta B_\perp/\lambda_0)}{\pi\Theta B_\perp/\lambda_0}\right| \int dk\ \eta(k)\ \sin(k\delta). \tag{2.24}$$

---

[3] For historic reasons, the absolute value $|V|$ of the modulus V is often sloppily referred by the term “visibility”.

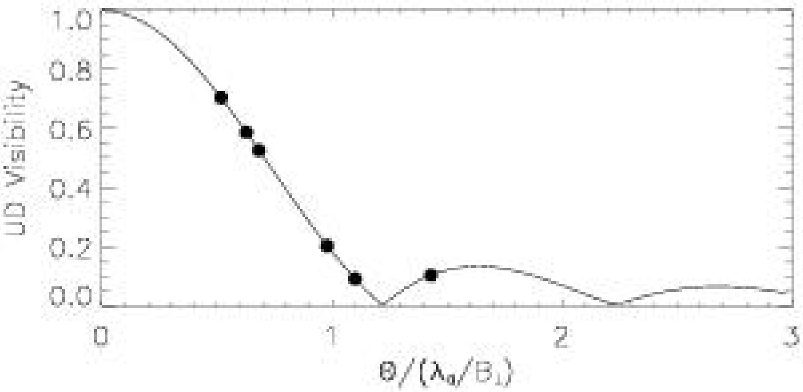

Figure 2.3: Visibility of a Uniform Disk. *The absolute value of the modulus of the complex visibility is plotted. The dots indicate visibilities as they would ideally be observed at 10 µm with the six baselines provided by the VLTI Unit Telescopes (see section 3.1) on a source with a uniform disk diameter of 22 mas.*

2.2.3 Effect of a Finite Bandwidth

In the last step, an example for the effects of a finite spectral bandwidth is presented. Let the overall spectral response η of the instrument be a rectangular bandpass of amplitude $\eta_0 = 1$ in the range $(k_0 \pm \Delta k/2)$ with $|\Delta k| = 2\pi\Delta\lambda/\lambda_0^2$ and zero elsewhere. The total power collected by one aperture may be $P_0 = P_{k_0} \cdot \Delta k$. Then the integral in equation (2.24) can easily be evaluated, and the power in one interferometric beam, normalised to the total power P_0 received by one telescope, becomes

$$\frac{P(\mathbf{n},\mathbf{B},\delta)}{P_0} = 1 + \underbrace{\left|\frac{2J_1(\pi\Theta B_\perp/\lambda_0)}{\pi\Theta B_\perp/\lambda_0}\right|}_{V_{obj}} \cdot \underbrace{\frac{\sin(\pi\delta\Delta\lambda/\lambda_0^2)}{\pi\delta\Delta\lambda/\lambda_0^2}}_{S_{inst}} \cdot \underbrace{\sin(2\pi\delta/\lambda_0)}_{I_{exp}} . \tag{2.25}$$

The underbraced terms are discussed in the following section.

2.3 Discussion

Basic Oscillation In expression (2.25), I_{exp} defines the fundamental interference. It is evoked by the experiment when scanning the OPD δ. The frequency is determined by the observing wavelength λ_0.

Instrumental Properties S_{inst} describes the instrument as used for measurements. In general, S_{inst} is a product of several factors that describe the state of the instrument like, e.g., unequal aperture size, overlap of the beams, angular alignment, or surface quality of the optics (see section A.1). It can be seen as a modulation of the amplitude of the interference and thus as an envelope of the interference. In the present case, a finite wavelength response was considered which results in the given sinc function.

It should be noted that the sinc function contains the coherence length

$$L_{coh} = \lambda_0^2/\Delta\lambda, \tag{2.26}$$

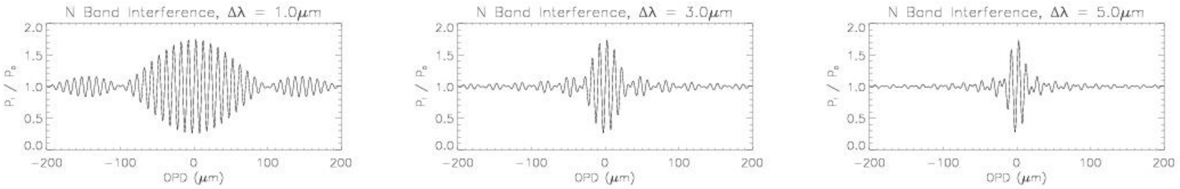

Figure 2.4: Calculated N band interference patterns. *The interferometric flux given by equation (2.25), normalised by the total power received by one aperture, is plotted versus the OPD. Assumptions are an object visibility of 0.75, full transmission in these bands, and a spectral width of 1 µm, 3 µm and 5 µm respectively.*

which is the scale length up to which the OPD of the interfering beams must be matched in order to achieve interference. For $|\delta| = L_{coh}$ the modulation falls to zero. This is seen in Figure 2.4 where some calculated interferogram are plotted as they could be expected for MIDI. They are drawn for $\lambda_0 = 10\,\mu\mathrm{m}$, $V_{obj} = 0.75$, and for the case that S_{inst} is only determined by the spectral instrumental properties. One can see how the width of the central wave package varies with spectral width. For comparison, Figure 2.5 shows an interferogram for a spectral width of roughly 5.5 µm like it was recorded during laboratory tests of MIDI. For an OPD larger than L_{coh}, i.e., $|\delta| > L_{coh}$, interference is strongly suppressed.

Coherence Length This latter behaviour can be made plausible in the following way (Born and Wolf, 1999, Section 7.5.8). In the interferometer, each single *monochromatic* component produces a different interference pattern. All these patterns are *superposed incoherently*, a fact that was actually used to put up equation (2.14) and which in the end yielded the envelope of the total interference pattern. As the OPD increases, the component patterns mutually average each other to a constant level because of their different wavelengths. The coherence length is the typical length of the OPD at which this happens[4].

Therefore, in reality when scanning the OPD the visibility of interference fringes decreases with increasing OPD, so that interference is mainly to be expected within the central lobe of the envelope where $|\delta| < L_{coh}$.

---

[4] In the case of single spectral lines, it is interesting to note that the quantised and statistical nature of light offers an alternative view supposing wave trains of finite length (Born and Wolf, 1999, Section 7.5.8). They can only interfere if the OPD is shorter than their roughly common length.

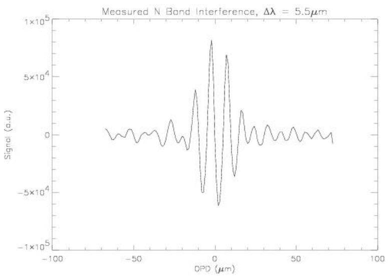

Figure 2.5: Measured broad N band interference pattern. *The signal is averaged over four scans and given in arbitrary units. A filter with a spectral width of about 5.5 µm was used.* (*Przygodda, 2001*)

Object Visibility Finally, V_{obj} is the actual figure of interest which describes the astronomical object. The aim of interferometry is to retrieve V_{obj} from an interferometric experiment. For doing so, all the other factors have to be well-known or possible to be calibrated. In order to obtain an estimation for these factors, two major steps must be taken. First, hardware components must be characterised for their behaviour, e.g., the exact shape of the spectral response or the device by which the OPD is scanned (Internal Delay Line; see section 4.2). This is done prior to the experiment. To have a handle on instrumental effects during observations, and assuming that the instrument is stable over a time scale of at least several minutes, a second measure is taken. If one can assume V_{obj} as well-known for an object, the instrumental factor S_{inst} can be calibrated. In stellar interferometry this is done by observing so-called calibrator stars. Their observations deliver an estimation of S_{inst} so that, in return, V_{obj} can be derived for the science object which is under investigation.

For a brief outline of the data acquisition process, refer to section 2.4.

Object Modeling The full procedure for gaining information about the source is to repeat the measurements and the data reduction process with different baselines. As indicated in Figure 2.3, this will yield an according number of visibility points. The proportions between the baselines were chosen in accordance to the ones provided by the Unit Telescopes of the VLTI. These data can be fitted by applying a model, for example, of a uniform disk to the data points which in turn will yield the source diameter.

In the general case, the source might not be well-described by a uniform disk model because the object brightness becomes fainter towards the edge (limb-darkening effect) or there is effectively no sharply defined edge like, for example, in dust distributions. Retrieving a diameter then might be less obvious. Nevertheless, as it was mentioned with equation (2.16), the measured visibility is determined by the Fourier transform of the source brightness distribution. Therefore, comparing models of astrophysical objects with results from stellar interferometry can help constrain model parameters and improve the understanding of astrophysical processes (see section 5.2).

2.4 A Simple Visibility Measuring Algorithm

As indicated in section 2.3, scanning the OPD is the basic principle of data acquisition in coaxial pupil plane interferometry. This results in an interference signal whose amplitude is the product of an instrumental factor V_{inst} and the object visibility V_{obj}. If it is assumed that V_{inst} can be calibrated, then the full amplitude M of the interference, which corresponds to the object visibility V_{obj}, can be restored.

For the MIDI instrument several data acquisition modes are anticipated to retrieve[5] the visibility. A quite straightforward mode is called the ABCD method. It is similar to the procedure employed at the Palomar Testbed Interferometer (Colavita, 1999; Colavita et al., 1999). As indicated in Figure 2.6, the OPD is adjusted in four steps which are $\Delta\delta = \lambda_0/4$ apart. The associated signals then are (cf. equation (2.11)):

$$A = M \cdot \sin[(2\pi/\lambda_0) \cdot \delta_A + \phi_0] + const., \tag{2.27}$$

$$B = M \cdot \sin[(2\pi/\lambda_0) \cdot (\delta_A + 1 \cdot \lambda_0/4) + \phi_0] + const., \tag{2.28}$$

---

[5] See also Appendix B.

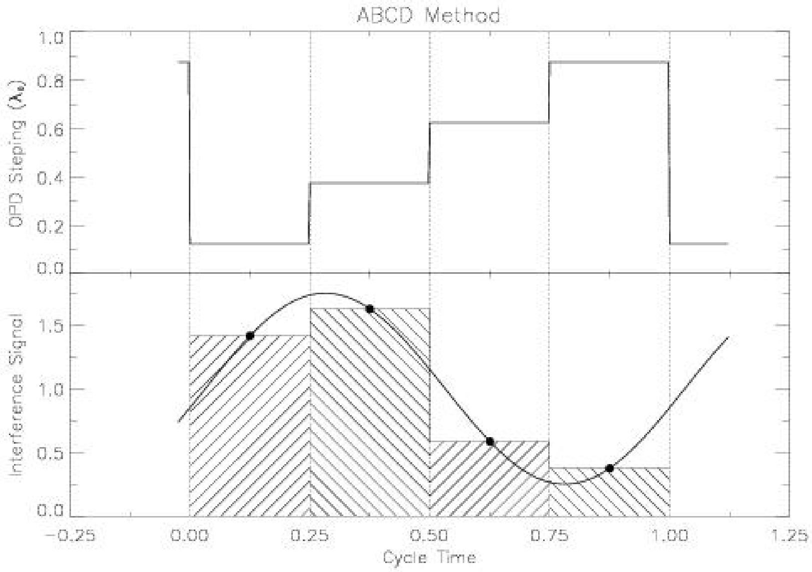

Figure 2.6: ABCD scan mode. *In the bottom diagram, the solid line shows the interferometric signal registered when the OPD were scanned continuously. In the ABCD mode, though, the OPD remains fixed during a quarter of the cycle time as sketched in the top diagram. During this period the interference signal (heavy dots) is integrated which is indicated by the hatched area.*

$$C = M \cdot \sin[(2\pi/\lambda_0) \cdot (\delta_A + 2 \cdot \lambda_0/4) + \phi_0] + \mathit{const.}, \tag{2.29}$$

$$D = M \cdot \sin[(2\pi/\lambda_0) \cdot (\delta_A + 3 \cdot \lambda_0/4) + \phi_0] + \mathit{const.}, \tag{2.30}$$

where δ_A is the OPD of the first measured point. ϕ_0 contingently summarises present phase shifts due to instrumental or atmospheric effects. The above set of relations can be rewritten into

$$A = M \cdot \sin[(2\pi/\lambda_0) \cdot \delta_A + \phi_0] + \mathit{const.}, \tag{2.31}$$

$$B = M \cdot \cos[(2\pi/\lambda_0) \cdot \delta_A + \phi_0] + \mathit{const.}, \tag{2.32}$$

$$C = -M \cdot \sin[(2\pi/\lambda_0) \cdot \delta_A + \phi_0] + \mathit{const.}, \tag{2.33}$$

$$D = -M \cdot \cos[(2\pi/\lambda_0) \cdot \delta_A + \phi_0] + \mathit{const.} \tag{2.34}$$

It follows that for the full modulation ($2M$) of the signal

$$2M = \sqrt{(A-C)^2 + (B-D)^2}. \tag{2.35}$$

The phase ϕ of the first data point with respect to zero OPD is

$$\phi = [(2\pi/\lambda_0) \cdot \delta_A + \phi_0] = \arctan\frac{(A-C)}{(B-D)}. \tag{2.36}$$

Also other combinations of (A, B, C, D) are possible in order to retrieve M and ϕ. For M, they may differ in the proportionality factor, which is 2 in equation (2.35).

It is clear that equations (2.27) through (2.30) apply to a single wavelength λ_0 at which the fringe contrast is evaluated. For a different wavelength λ' the OPD steps do not meet the condition of being one quarter of the wavelength. The four steps of width $\Delta\delta = \lambda_0/4$ each will cover more or less than λ'. Therefore, the ABCD method as presented above is only directly applicable in one spectral channel at a time, when MIDI is operated in a dispersive mode. Thereby, it is essential to have a well-calibrated wavelength axis on the detector so that the wavelength to enter is precisely known. Section 4.5 focuses on the calibration of the spectral axis as received on the detector. Another important aspect is the precision of the change in OPD, i.e., the displacement of the piezos in the IDL of MIDI. The characteristics of the piezos are presented in section 4.2.

Chapter 3

MIDI at the VLTI

This chapter will give an overview of the VLTI environment and its characteristics which are particularly relevant for MIDI. The scientific motivation for interferometry at 10 µm is outlined and the peculiarities of observing at this wavelength. Furthermore, the chapter discusses the MIDI instrument and its sub-units. For an overview, Table 3.1 shows a summary of some basic parameters of the VLTI and MIDI.

3.1 The VLTI Environment

3.1.1 Telescopes

Unit Telescopes (Koehler, 1998; Wallander et al., 2000) The main components of the VLTI are four Unit Telescopes (UT), each with a primary mirror of 8.2 m diameter (8.0 m clear aperture of input pupil). Figure 3.1 contains an aerial view and a geometric scheme. The VLTI telescopes are specified for operation at wavelengths between roughly 0.5 µm and 20 µm (Koehler et al., 2002). The angular resolution of a single telescope is defined as

$$\phi = \frac{\lambda}{D}, \tag{3.1}$$

which is the angular FWHM of its diffraction limited focal point (Airy disk), where λ is the observation wavelength and D the clear aperture. For a UT, the resolution at $\lambda = 10\,\mu\mathrm{m}$ is $\phi_{UT} = 0.26''$ ($\phi_{UT} = 0.21'' \ldots 0.34''$ for $\lambda = 8 \ldots 13\,\mu\mathrm{m}$). The total of six independent baselines B between two UTs range from 47 m to 130 m. Using two telescopes in interferometric mode, the resolution is again given by equation (3.1) where the baseline[1] B enters for the telescope diameter:

$$\phi_{ifm} = \frac{\lambda}{B}. \tag{3.2}$$

Thus, the baseline range translates in interferometric mode at 10 µm to a resolution range[2] between $\phi^{UT}_{ifm}(10\,\mu\mathrm{m}) = 0.044''$ and $\phi^{UT}_{ifm}(10\,\mu\mathrm{m}) = 0.016''$.

Auxiliary Telescopes (Koehler and Flebus, 2000) In addition to the stationary UTs, there will be up to three[3] additional Auxiliary Telescopes (AT), with an entrance pupil of 1.8 m and

---

[1] Strictly speaking, it is the baseline *projected* into observing direction. Here, zenith observation is assumed.

[2] For comparison, the angular diameter of the Sun with $D = 0.01$ AU as seen from our stellar neighbour α Cen at 1.3 pc distance is $0.007''$. The red giant star α Ori (Betelgeuse) at 60 pc distance with $D = 2.8$ au appears under $0.047''$.

[3] Negotiations are underway to procure a fourth AT.

Table 3.1: Basic parameters of MIDI and the VLTI (selection). *Calculated numbers are for 10 µm or, where ranges are given, for the N band (8. . . 13 µm) respectively.*

	UTs	ATs
Telescope aperture, D	8.0 m	1.8 m
VLTI baselines, B	47. . . 130 m	8. . . 202 m
Telescope Airy disk[a,b] (FWHM)	$0.26''$	$1.1''$
VLTI spatial resolution[a,b]	$0.044'' \ldots 0.016''$	$0.26'' \ldots 0.010''$
Field of view[c]	$\approx 1''$ radius	
Interferometric field of view[b,c,d]	$\pm 0.088'' \ldots 0.032''$	$\pm 0.52'' \ldots 0.020''$
Beam diameter at MIDI input	18 mm	
Wavelength range used by MIDI:	N band (8. . . 13 µm),	
expandable to	Q band (17. . . 26 µm)	
Differential dispersion	46 µm (1.6. . . 10 µm)	
in 100 m of dry air	0.9 µm (10. . . 20 µm)	
Atmospheric stability:		
turbulence[b] time scale	100 ms, for fringe motion ≤ 1 µm RMS	
thermal[b] time scale	200 ms, for chopping	
Background[b,d,e]:		
from VLTI mirrors	$1.5 \cdot 10^{11}$ photons/s	
from sky	$6.2 \cdot 10^{9}$ photons/s	
Signal of $N = 0$ mag (40 Jy) star[b,d,e]	$2.4 \cdot 10^{9}$ photons/s	$1.2 \cdot 10^{8}$ photons/s
MIDI limiting N magnitude (goal)[b,d,e]:		
without fringe tracking	4 mag (1 Jy)	0.8 mag (20 Jy)
external fringe tracking[f]	9 mag (10 mJy)	5.8 mag (200 mJy)
MIDI detector	pixel size $(50\,\mu\mathrm{m})^2$, 320×240 pixels full well capacity $\approx 10^7$ electrons read noise $\approx 10^3$ electrons per read	

[a] λ/D respectively λ/B

[b] $\lambda = 10\,\mu\mathrm{m}$

[c] see section 3.1.3

[d] with $\Delta\lambda = 5\,\mu\mathrm{m}$ (broadband)

[e] in Airy disk with radius λ/D at MIDI detector, see section A.1

[f] for a broadband on-source integration time of 1000 s

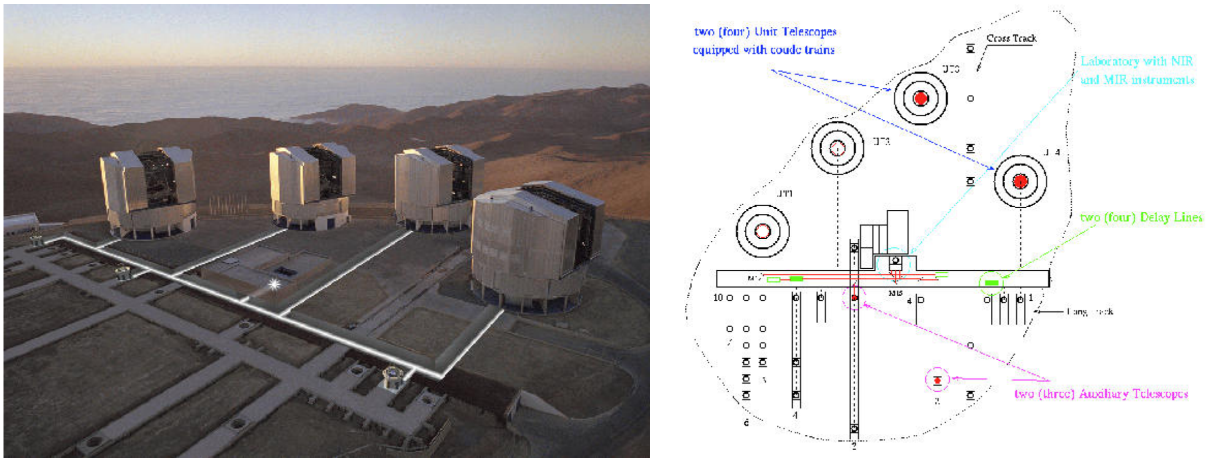

Figure 3.1: View and ground plan of the VLTI. *In the aerial view, the white lines indicate the optical path from the Unit Telescopes to the Interferometric Laboratory where the beams are combined. North is up in the layout drawing. (Images: ESO (2002))*

thus a resolution of $\phi_{AT}(10\,\mu\text{m}) = 1.1''$ ($\phi_{AT} = 0.92'' \ldots 1.5''$ for $\lambda = 8 \ldots 13\,\mu\text{m}$). Their special property is that they can be relocated to 30 different pre-defined positions with separations of 8 m to 202 m. This yields an interferometric resolution of $\phi^{AT}_{ifm}(10\,\mu\text{m}) = 0.26''$ down to $\phi^{AT}_{ifm}(10\,\mu\text{m}) = 0.010''$. The ATs will enable full time use of the VLTI facilities, while UT observing time is shared between single-telescope and interferometric instruments. The smaller diameter of the ATs, reduced by a factor ≈ 4.5 compared to the UTs, means that their light collecting area is $(4.5)^2 \approx 20$ times smaller. Considering equation (A.17), their limiting magnitude will be about 3.2 mag lower. They are therefore likely to be used for bright objects. The current schedule has the ATs becoming operational at Paranal end of 2003.

Siderostats (Derie et al., 2000) Besides the afore-mentioned telescopes, two siderostats (which can be installed at any of the AT locations) are currently available on Paranal. They offer apertures with 0.4 m diameter. Their intention is to provide a facility to test the interferometry subsystems and instruments with little impact on other programmes at the telescopes, but also allow to perform scientific observations on bright objects.

3.1.2 Delay Lines

In order to observe an object interferometrically, it is necessary to direct the beams from the observing telescopes to laboratory instruments that perform coherent superposition. In doing so, the optical paths of the beams must be equalised with a precision of roughly 1/10 of the observing wavelength. In Figure 3.1, the path of the beams through an underground tunnel is shown with white lines. The interferometric laboratory is at the location of the white star. The geometric OPD between two telescopes depends on the baseline vector $\boldsymbol{B}$ between these telescopes and the observing direction $\mathbf{n}$ by (cf. equation (2.3))

$$OPD_{geom} = \mathbf{n} \cdot \mathbf{B} = B \cdot \cos\theta, \tag{3.3}$$

where θ is the angle enclosed by $\mathbf{B}$ and $\mathbf{n}$. In Figure 3.2, OPD_{geom} is indicated by the line between Telescope 1 and the closest drawn wavefront. For a given object, this value of course changes with sidereal time. The compensation of OPD_{geom} is performed by a Delay Line (DL),

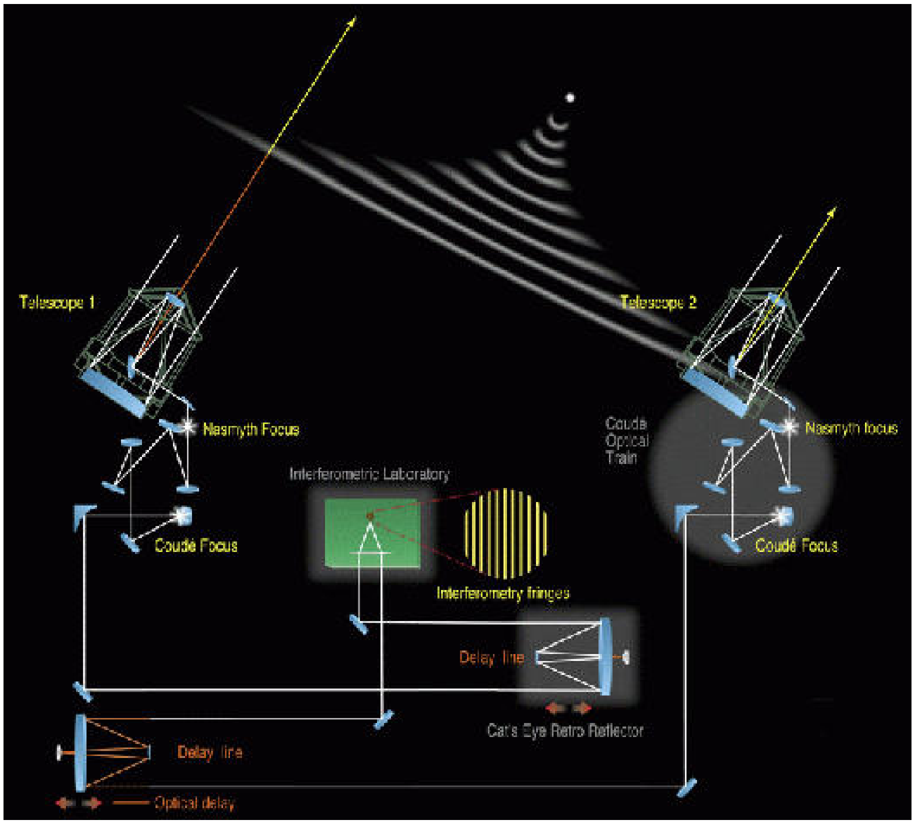

Figure 3.2: VLTI optical train. *Beam combination and interference pattern are drawn for an interferometer like AMBER. (Image: ESO (2002))*

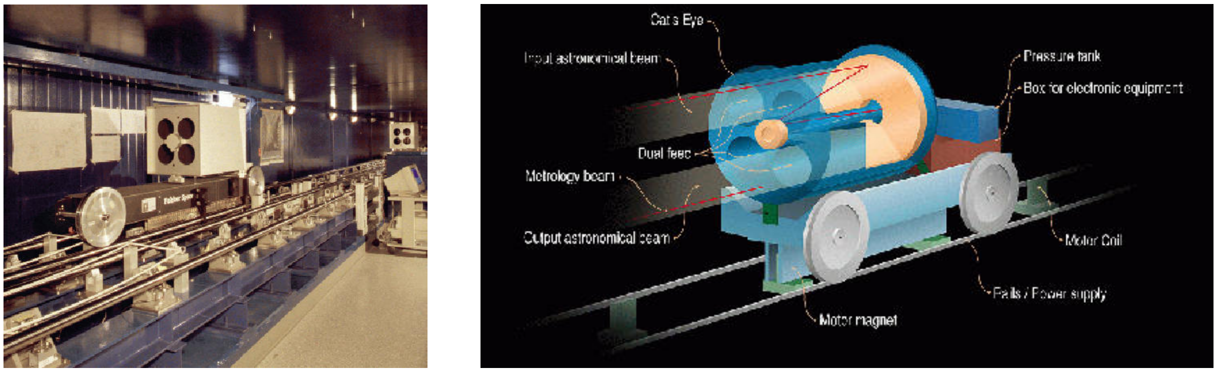

Figure 3.3: One of the VLTI Delay Lines. *Drawing and realisation of the Delay Line cart. (Images: ESO (2002))*

which is shown in Figure 3.3. In principle, the Delay Line is a movable mirror whose position is adjusted so that the OPD of the beams between the entrance pupils and the point of beam combination is nearly canceled. It is realised by a cat's eye reflector system which can be positioned with an accuracy of only a few dozen nanometers over a stroke length of 60 metres (Derie, 2000).

Cancellation of the OPD between two beams by the VLTI Delay Line is specified with an accuracy of ±2.5 mm. Besides the geometric OPD, there is also the additional OPD_{add} which is introduced by the atmosphere (see section 3.2.3) and the VLTI optical train. The total internal VLTI fluctuations are estimated to be 0.78 µm RMS at 10 µm observing wavelength in an exposure time of 290 ms (Koehler et al., 2002). Therefore, an interferometric instrument, requiring zero OPD for measurements, needs an additional Internal Delay Line (IDL) that provides a second step of rapid OPD correction to the precision mentioned before. The IDL for MIDI is discussed in section 4.2. Another possibility is to use a so-called fringe tracker that stabilises the fringe pattern by compensating OPD_{add} (see the PRIMA project mentioned in the following section).

3.1.3 Interferometric Instrumentation

After a further reduction of the diameter from 80 mm down to 18 mm and a total of 18 reflections (see Figure 3.2), the beams reach the Interferometric Laboratory where the main VLTI instruments are placed. Figure 3.4 shows a floor plan of the lab. At this point, the VLTI offers a Field Of View (FOV), projected back on the sky, of about 1″ radius. The full *interferometric* FOV Θ_{ifm} around the observing direction is given by the fact that the maximum allowed OPD $B \cdot (\Theta_{ifm}/2)$ *additional* to the geometric one from equation (3.3) must be shorter than the coherence length defined by the filter in use of width $\Delta\lambda$ and central (effective) wavelength λ_c (see equation (2.26)):

$$B \cdot (\Theta_{ifm}/2) < \frac{\lambda_c^2}{\Delta\lambda} \qquad \text{or} \qquad (\Theta_{ifm}/2) < \frac{\lambda_c}{B}\frac{\lambda_c}{\Delta\lambda} \quad . \tag{3.4}$$

B is again the baseline length[4] of the stellar interferometer. Observing with a baseline of 100 m at $\lambda_c = 10\,\mu\text{m}$ with $\Delta\lambda = 5\,\mu\text{m}$, this yields $\Theta_{ifm} \approx \pm 0.040''$. The wavefront error between two beams as delivered by the VLTI to the instruments is specified with 1.17 µm RMS for UT

---

[4] Note remark 1 on page 17.

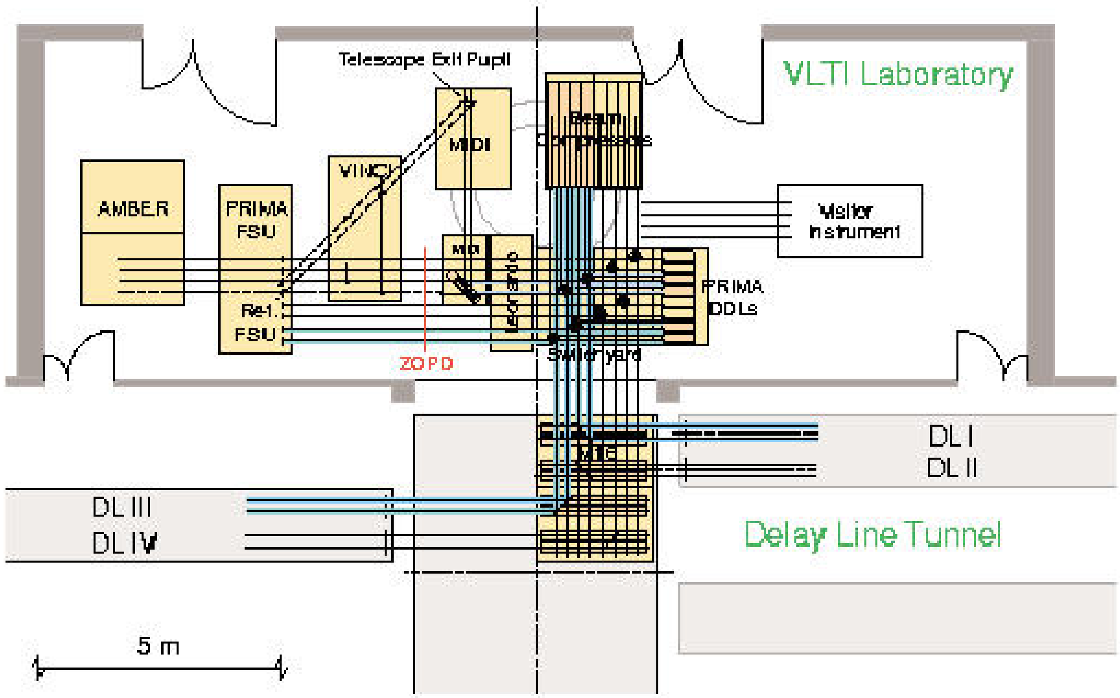

Figure 3.4: Ground plan of VLTI Interferometric Laboratory. *(Image: ESO (2001))*

beams and 0.33 µm RMS for AT beams without usage of an Adaptive Optics (see below) system (Koehler et al., 2002).

The following paragraphs shortly describe VLTI supporting units and the instruments in the Interferometric Laboratory except for MIDI. In section 3.3, the design and capabilities of MIDI are focused on.

MACAO (Donaldson et al., 2000) MACAO (Multiple Application Curvature Adaptive Optics) is an Adaptive Optics (AO) system which will be installed at several foci of the VLT. The term MACAO-VLTI indicates the application of this AO system for use by the VLT interferometer. All four VLT/UT Coudé foci will be equipped with such a system feeding the VLTI delay lines with a corrected (diffraction limited) IR beam in the range 1.0 . . . 13.0 µm. System performance is expected to show up to 50 % Strehl[5] ratio at 2.2 µm. The first MACAO-VLTI unit is scheduled for installation on Paranal by end of 2002. The final unit is foreseen to be installed by mid of 2003.

Part of MACAO is the System for Tip-tilt Removal with Avalanche Photodiodes (STRAP). As outlined in section 3.2.3, this unit alone will be able to perform a large part of signal correction for MIDI at 10 µm. Instruments at shorter wavelengths, like e.g. AMBER (see below), require the application of the full MACAO system.

VINCI (Kervella et al., 2000b) The fibre beam combiner VINCI (VLT INterferometer Commissionning Instrument) works in the K band around 2.2 µm. It uses a combination technique proven by the FLUOR (Fiber Linked Unit for Optical Recombination) instrument which has been operational at the IOTA (Infrared-Optical Telescope Array) stellar interferometer on

---

[5] See section A.3

Mt. Hopkins near Tucson, Arizona, USA since 1995 (Coudé Du Foresto et al., 1997; Perrin et al., 1998). Its main purpose is to show and characterise the functionality and performance of the VLTI facility in its first phase of installation. Astronomical observations made for this purpose should demonstrate the practicability of the science case and help prepare object lists that might serve as calibrator stars for the main VLTI science instruments (see section 5.1).

Furthermore, an important task of VINCI is measuring the zero optical path difference and serving as a reference point when aligning and recovering fringes after hardware and software upgrades of the VLTI respectively its different instruments.

Another feature is the provision of a set of unresolved and extended light sources, also referred to as “artificial stars”. These help in aligning the various VLTI instruments, e.g., by providing stable radiation sources. To date, the performance of these light sources is mainly specified at visible and near-infrared wavelengths. For the mid-infrared regime, development is still behind. Experiences gained with MIDI and its laboratory calibration sources (as described in section 4.3) will help constrain requirements and properties.

In the future, it is planned to source out the alignment sub-unit of VINCI and the calibration sources to a separate VLTI unit called ARAL.

AMBER (Petrov et al., 2000) The science instrument for the near-infrared regime is AMBER (Astronomical Multiple BEam Recombiner). Being designed for eventually interfering three beams in the pupil plane, this instrument will be able to construct *images by phase closure* techniques. In a first phase, AMBER will operate in the $1 \ldots 2.5\,\mu\mathrm{m}$ wavelength range with two UTs. The wavelength coverage will be extended down to $0.6\,\mu\mathrm{m}$ at the time the ATs become operational. Due to its working wavelength range, the performance of AMBER will strongly depend on availability of AO systems. In the K band around $2.2\,\mu\mathrm{m}$, for example, the Fried parameter is $r_0(2.2\,\mu\mathrm{m}) = 0.8\,\mathrm{m}$, which is roughly one tenth of the UT aperture size (see section 3.2.3). The magnitude limit of AMBER in the K band is expected to be 20 mag when a bright reference star for AO is available and 14 mag otherwise.

PRIMA (Delplancke et al., 2000) The objective of the planned PRIMA (Phase-Referenced Imaging and Microarcsecond Astrometry) project is to enable simultaneous interferometric observations of two objects that are separated by up to 1 arcmin, without requiring a large continuous FOV. The principle of operation relies on finding, within an area of about 1 arcmin around the science target, a sufficiently bright star that can be used as a reference star for the measurement and the stabilisation of the science fringe motion induced by atmospheric turbulence, namely the piston effect (see section 3.2.3). This fringe stabilisation will be performed by the FINITO (Fringe-tracking Instrument of NIce and TOrino) respectively an equivalent sub-unit of PRIMA. The performance is expected to yield an OPD fluctuation of less than $0.1\,\mu\mathrm{m}$ RMS (Koehler et al., 2002). By allowing longer integration times, this mode increases photometric sensitivity by an expected 3 mag or more. The other interferometric instruments will accordingly benefit from this fringe stabilisation.

Additionally, all optical path lengths of the reference star and of the science star inside the interferometer will be controlled with a laser metrology system, and fluctuations will be compensated for by adjusting the Differential Delay Line (DDL) which is also shown in Figure 3.4. It will therefore allow to preserve the visibility phase information. This introduces the capability of *phase-referenced imaging* of science objects with two telescopes and of determining the angular separation between two stars. Installation of first PRIMA sub-units at the VLTI is planned for the year 2004.

Visitor instrument Besides the instruments described so far, there is considerable spare space foreseen for experimental instruments by external visitors which can use the VLTI beams. An option would be to test here new technology instruments, for example nulling interferometers that highly suppress light from bright stars to detect faint emission from neighbouring dust and possibly massive extra-solar planets. The newly announced Ground-based European Nulling Interferometer Experiment (GENIE) (Gondoin et al., 2002) is a joined ESA/ESO project in order to study technological demands and gain experience in their solution. It could demonstrate the working principle of future space missions like, for example, DARWIN.

3.2 Mid-Infrared Interferometry with MIDI

3.2.1 Scientific motivation

The mid-infrared wavelength range around 10 µm is a regime where emission originating from dust plays an important role in astrophysical processes. For matter at temperatures 230 . . . 370 K, the maximum of blackbody emission lies in the N band. The main scientific topics that will be addressed with MIDI are:

- Star formation and Young Stellar Objects (YSO): size, geometry and structure of protostellar cores, circumstellar disks and envelopes; YSO multiplicity, determination of mass ratios
- Evolved stars: size, geometry and structure of dust and molecule envelopes around Asymptotic Giant Branch (AGB) stars; spatial pulsation of variable stars; surface structure (e.g., spots)
- Substellar objects: aiming at a direct detection and, where possible, spectroscopy of brown dwarfs and hot massive planets by differential interferometric techniques (observationally and technically demanding)
- Active Galactic Nuclei (AGN): existence, size, and possibly structure of dust tori
- Other programs: e.g., hot stars, the Galactic centre, volcanism in the solar system

With the VLTI, it will be possible to extend full interferometric resolution to fainter objects and therefore also to new classes of objects. A detailed description of the scientific prospects of interferometry, not only at 10 µm, is found, for example, in Paresce (1997).

3.2.2 Technical Aspects

Apart from this scientific motivation for interferometry in the mid-infrared regime, there is another advantage compared to the near-infrared or, to a greater extent, to the visible regime. Optical and mechanical requirements are less stringent since the demands relax and scale with the wavelength.

On the other side, the mid-infrared regime also suffers from high thermal background produced by the atmosphere, VLTI telescopes, and transfer optics. The signal of a 0 mag object

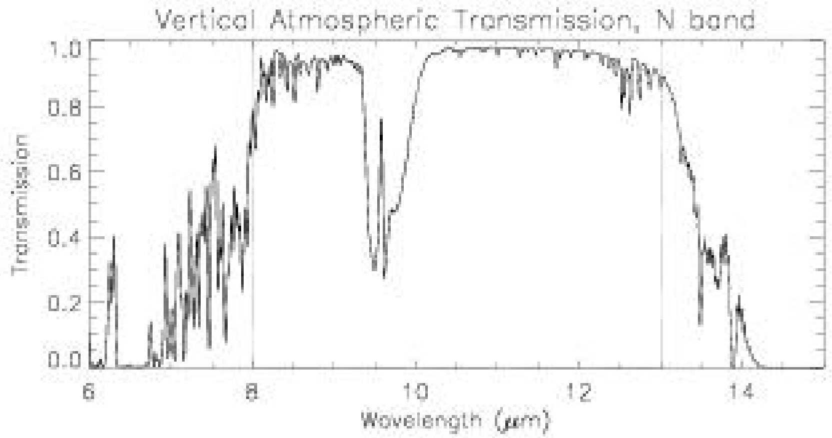

Figure 3.5: Atmospheric transmission in the N band. *Shown for the Mauna Kea observation site on Hawaii (Lord, 1992) at water vapour column of 1.0 mm and air mass AM* = 1.5. *(With z the zenith angle, the air mass is* $AM = 1/\cos z$ *(Léna et al., 1998).) Except for a strong absorption around* 9.5 μm *due to the ozone layer in the upper atmosphere and a few minor other lines, the atmosphere is highly transparent, in particular between 10 μm and 12 μm.*

is roughly 1 % of the optics background (see section A.1). Therefore, chopping is necessary to extract the source signal from the background. For a typical integration time of 25 ms, which is driven by the need to perform a full measurement within one atmospheric turbulence time scale (see below), the background signal produces about 10^9 electrons on the detector. Because the detector has a well depth of 10^7 electrons per pixel, another requirement is to spectrally disperse the signal over at least 100 pixels in order not to saturate or operate in a non-linear regime. Another option is to decrease the integration time and perform repeated short reads of the detector.

3.2.3 Atmospheric Conditions

Ground-based astronomy in the mid-infrared regime is made possible by the atmospheric transmission window in the so-called N band between 8 µm and 13 µm and in the Q band between 17 µm and 26 µm. The transmission for the N band is shown in Figure 3.5. The atmosphere also affects astronomical observations in respect to the stability of observing conditions. This is discussed in the following paragraphs.

Quantities from Turbulence Theory For a given wavelength λ, the Fried parameter r_0 describes the turbulent behaviour of the atmosphere integrated over its total height H. r_0 can be interpreted as a scale length, perpendicular to the line of sight, over which the phase of a light wavefront coming from a star may be considered as constant. The atmosphere can be seen as layers of air at a given height h moving at a wind speed v_w. Turbulence causes density variations and thus fluctuations of the refraction index. The quantity $C_n^2(h)$ describes these fluctuations. Observing at an angle z from the zenith, one yields for r_0 (Tyson, 1998):

$$r_0 \propto \lambda^{6/5} (\cos z)^{3/5} \left(\int_0^H C_n^2(h)\, dh \right)^{-3/5} . \tag{3.5}$$

Directly related to r_0 is the coherence time, $\tau_0 \propto r_0/v_w$, which describes the time scale over which atmospheric conditions may be considered as quasi-frozen and so the wavefront phase does not change perceivably.

Furthermore, the FWHM of the seeing α, which describes the ability of a telescope to resolve two point-like objects when observed through the atmosphere, can be shown to follow the relation $\alpha = 0.98\,\lambda/r_0$ (Glindemann et al., 2000).

Specifics at Paranal Because all these quantities depend on atmospheric properties, they can vary for specific sites, time of day etc. For the VLT(I) on Mt. Paranal, recent values of these quantities can be found in the ESO (1999) reference. Latest measurements appear in Martin et al. (2000). In the year 2000, the median seeing value on Paranal was $0.75''$, measured at $0.5\,\mu\mathrm{m}$ zenith pointing. This translates to a Fried parameter of $r_0(0.5\,\mu\mathrm{m}) = 0.14\,\mathrm{m}$. The median coherence time was 3.6 ms.

By means of equation (3.5), in particular using $r_0 \propto \lambda^{6/5}$, it is possible to derive the expected values of the discussed quantities for the N band, namely the Fried parameter $r_0^N = 5.0\,\mathrm{m}$, the seeing $\alpha^N = 0.40''$, and the coherence time $\tau_0^N = 130\,\mathrm{ms}$. These findings imply two main consequences:

1. Because r_0^N is roughly of the aperture size of one Unit Telescope (and, notably, larger than the ATs), the wavefront phase can be considered as almost constant over the aperture. Therefore, interferometry with the VLTI at $10\,\mu\mathrm{m}$ depends little on an Adaptive Optics system, which would correct mainly higher order aberrations in one aperture. Application of a tip-tilt correction provided by a mirror in the Coudé optical train already compensates signal variations to a high degree (see MACAO system in section 3.1.3).

   The main remaining atmospheric effect is the piston difference, i.e., the offset of the wavefront phase, introduced by the atmosphere between the two interfering telescope apertures. This piston effect, which is a random effect, causes fringe motion, i.e., a shift of the zero OPD position. At $10\,\mu\mathrm{m}$ observing wavelength and 290 ms exposure time, it is estimated as $0.63\,\mu\mathrm{m}$ RMS for the purely atmospheric contribution, i.e., outside the interferometer (Koehler et al., 2002). For a long exposure time, the peak-to-valley value is $30\,\mu\mathrm{m}$ (Glindemann, 2002).

2. As long as there is no fringe sensor unit installed which compensates for this remaining piston error, all exposures taken by MIDI must be qualitatively shorter than τ_0^N, in order to avoid smearing of the interference pattern.

   For a quantitative estimation of the maximum possible exposure time, Leinert et al. (1997) chose an approach different to that presented above. A tip-tilt corrected telescope was assumed with a diameter equal to the separation of UT1 and UT2 at the VLTI, i.e., 54 m. As a critical condition it was assumed that the corresponding image centroid would move less then 1/10 of the fringe spacing, i.e., $1\,\mu\mathrm{m}$. Considering the bandwidth requirements for such a system, a maximum exposure time of 120 ms was derived. This is essentially the same value derived above.

   The equivalence between the two approaches to derive an appropriate exposure time is given in the following argument, again taking into account a frozen atmospheric layer. As stated above, the phase of a wavefront is considered constant over r_0. With the layer moving at a wind speed v_w, the phase distribution in the aperture will have changed after the distance r_0 is covered and thus the image centroid will move. The time scale of this motion will be proportional to r_0/v_w, i.e., τ_0.

Therefore, to be on the safe side, the usual maximum time frame assumed for a full interferometric measurement with MIDI was adopted as 100 ms.

Sky Background Apart from turbulence affecting mainly the phase between the beams, there are, in addition, fluctuations in the photometric background of the sky due to temperature or opacity variations (see also section A.1). Thereby, the photometric estimation which is partially used in MIDI for fringe amplitude estimation may be falsified. Experience from the 10-µm camera MAX at the UKIRT telescope indicates that the typical time scale for these thermal fluctuations is $\tau_{sky} \approx 200\,\mathrm{ms}$ (Robberto and Herbst, 1998). This requires a chopping frequency of 5 Hz in order to calibrate for the sky background.

An expanded treatment of effects of atmospheric turbulence on visibility measurements with MIDI are presented by Porro et al. (2000).

3.3 The MIDI Instrument

MIDI, the MID-infrared Interferometric Instrument, will work in the N band between 8 µm and 13 µm (Leinert et al., 2000). In a later phase, it is expected to extend MIDI also to the Q band (17. . . 26 µm). Figure 3.6 contains a simplified schematic of MIDI. The optical table of MIDI expects two incoming beams of 18 mm diameter which are extracted from the VLTI beams and directed towards the MIDI optics.

3.3.1 Warm Optics

The extracted beams travel through the Warm Optics of MIDI which are mounted on an optical table in front of the instrument housing. Like the VLTI optics, the Warm Optics (and the Cold Optics within the cryostat) are designed such that the same number and kind of reflections occur in each light path. All mirrors involved are gold-coated in order to optimise their reflectivity[6] and tilt-adjustable. Both light paths are equipped with a piezoelectric stage carrying a roof mirror[7]. The piezos have a mechanical stroke of roughly 80 µm each and serve as the fast part of the Internal Delay Line and scanned according to operational mode (see section 2.4). The piezo stages are further focused on in section 4.2. One of the piezo stages is, in addition, mounted on a translation stage with a total mechanical stroke of about 25 mm. This allows static equalisation of the optical path of the beams (see section 3.1.2) to a few wavelengths in the first place so that nominal zero OPD is well within reach of the fast delay line piezo stages.

Another part of the Warm Optics is a set of alignment plates, working at visible light, which are mounted on the Warm Optical Table. They serve as the positional reference for the entire instrument. Together with two alignment telescopes, they are used to adjust the Warm Optics components.

A major group of devices within the Warm Optics is dedicated to the calibration of MIDI. Directly placed on the Warm Optical Table, there is a black screen which can be heated by about

---

[6] At 10 µm, the reflectivity of a gold-coated mirror is usually higher than 99 %.

[7] In a roof mirror, two plane mirrors enclose an angle of 90 degrees (see Figure 4.1). If it is mounted with the angle opening parallel to the optical table, a beam travelling parallel to the table is exactly reversed (see Figure 2.1), independently of the lateral incident direction of the beam.

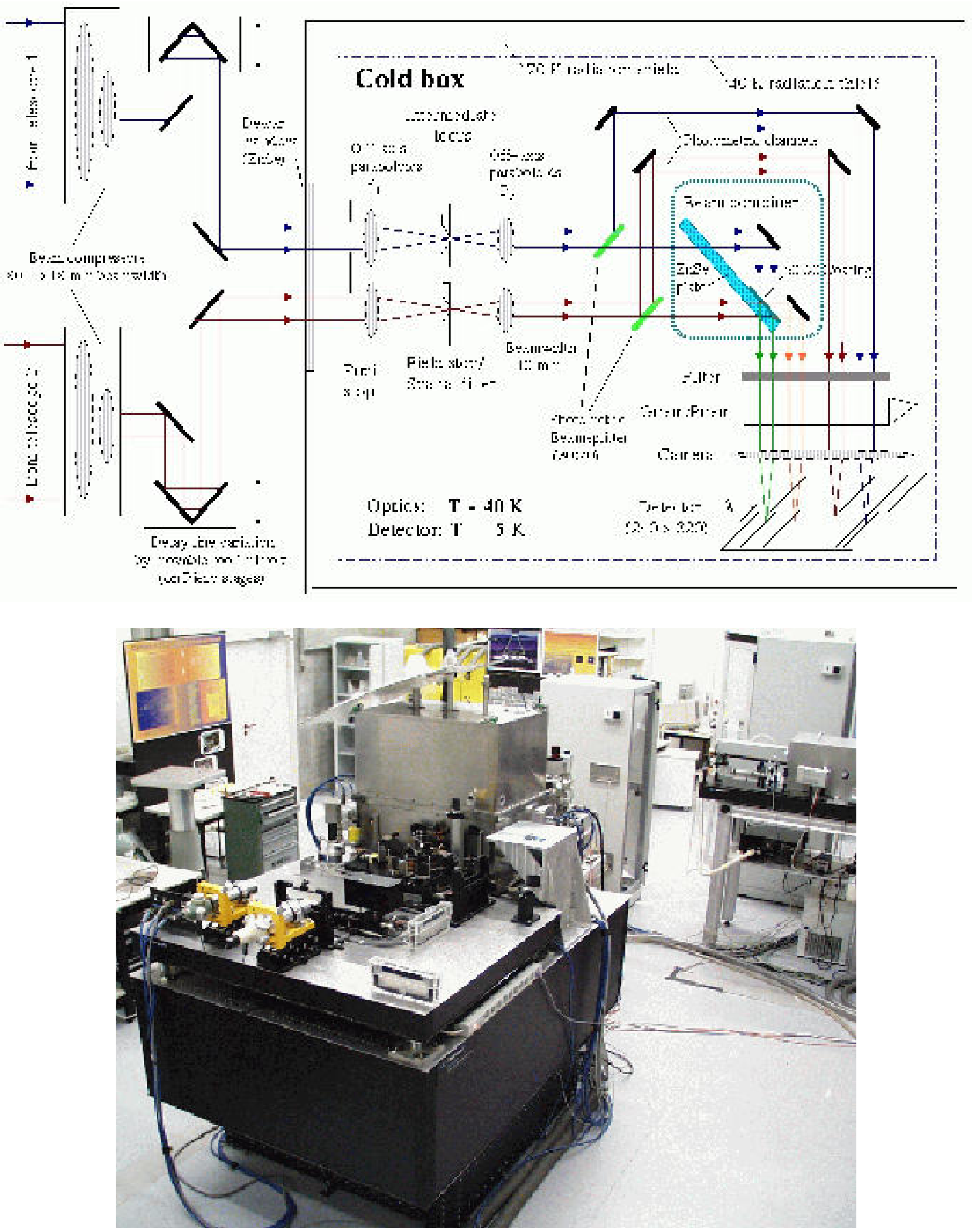

Figure 3.6: Scheme and overview of MIDI. *In front of the dewar lies the Warm Optics bench. In the overview on the far right one can see the extra optical table carrying two of the three calibration light sources.*

15 K above room temperature. It can be moved into and out of the FOV of MIDI, providing a field filling stimulus for the instrument during alignment and calibration procedures.

Another set of calibration light sources, mainly a CO_2 laser, is placed on an extra optical table which, on Paranal, will be in a room adjacent to the Interferometric Lab (see section 4.3). Their collimated light is directed towards the Warm Optical Table. Here, the incoming beam travels through a beamsplitter and is fed into the two optical inputs of MIDI, i.e., before passing the IDL, with an OPD set close to the one expected for the VLTI beams. This feed-in unit is likewise mounted on a drive stage and moved into the beam train when needed.

3.3.2 Dewar

After passing the Warm Optics, the beams enter the MIDI housing with a separation of 30 mm. In Figure 3.7, the main subunits placed in the MIDI dewar are shown. The dewar is evacuated to $\approx 10^{-7}$ mbar. In a first step, the dewar is cooled by liquid nitrogen. A radiation shield, which is in thermal contact with the tank, encloses the cold optical bench. The second cooling step is a helium liquefying Closed Cycle Cooler (CCC), which has two stages of which the first is connected to another radiation shield, and the second stage cools directly the detector mount. In Figure 3.6, one can see the nominal temperatures reached at each of these steps. The CCC is placed on a separate pedestal and is connected to the dewar by a vacuum bellows, in order to minimise vibration transfer from the CCC to the dewar. Vibration isolation, thermal insulation, and optical baffling of the optical train are crucial points in the design of MIDI.

To have the possibility of aligning MIDI to the VLTI, and to compensate for thermally induced displacements by cooling down, the MIDI dewar is placed on a five-axes mount which allows translations of up to ±2 mm in two dimensions (perpendicular to beam axis) and ±0.1 degrees of rotation about the three spatial axes.

3.3.3 Cold Optics

Figure 3.8 shows the layout of the MIDI cold optics inside the dewar.

Beam Cleaning Right after the entrance window of the dewar there is a cold shutter unit that may be used to block each beam independently. The beams then pass a cold stop, which is placed at an image[8] of the telescope entrance pupils. The cold stop suppresses unwanted thermal radiation from outside the acceptance angle of the telescopes.

The beams are then compressed from 18 mm to 10 mm diameter by two off-axis parabolic mirrors with a common adjustable focus. Thereby, in the intermediate focus, the beams can be spatially filtered by a variety of pinholes and slits. Investigations for an additional single mode fibre are still ongoing.

Beam Combination Following beam cleaning and compression, the beams enter the beam combining assembly, which is the heart of the interferometer (see Figure 3.8). Before interfering at the actual beam-combiner, two so-called photometric beams are optionally coupled out from the incoming beams. This photometric information can be used at data reduction (see Appendix B).

---

[8] The middle point between the re-imaged pupils defines the origin of the local MIDI coordinate system.

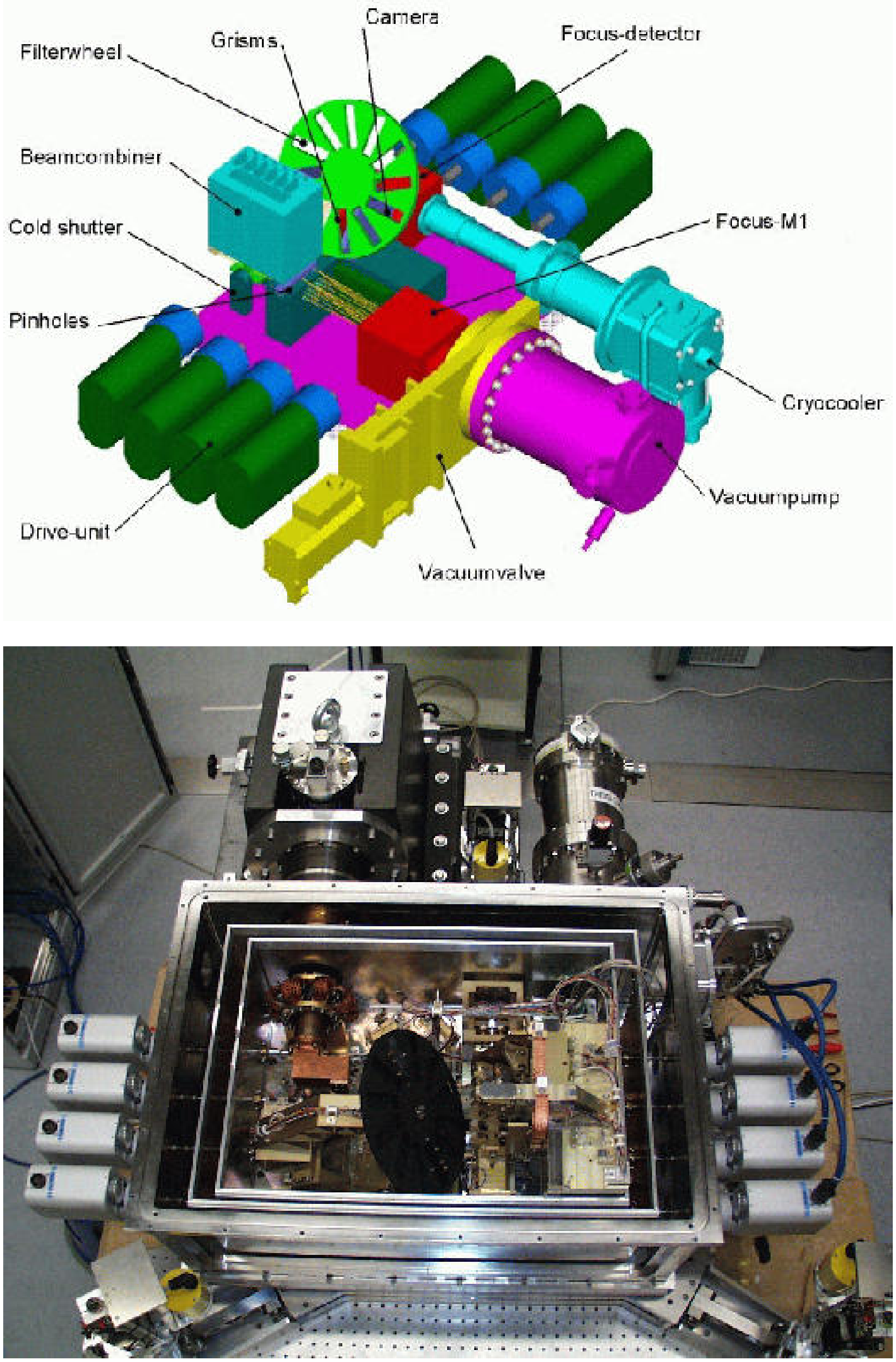

Figure 3.7: MIDI Dewar. *Top: Mechanical drawing with the major functional units. Bottom: View inside the dewar.*

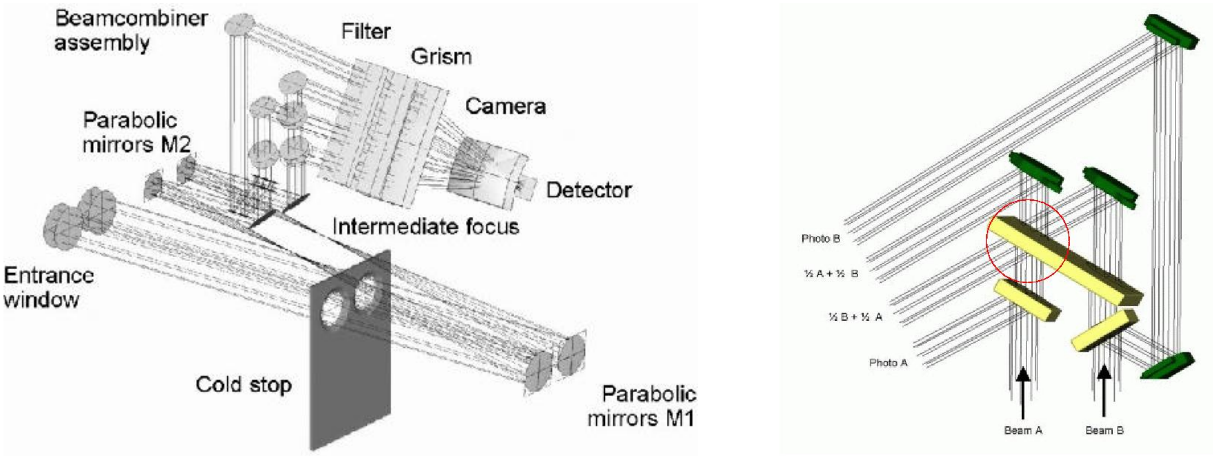

Figure 3.8: MIDI Cold Optics. *Left: Complete optical path inside the dewar from the entrance window to the detector; Right: Side view of the Beam Combining Unit in MIDI. From the incoming beams, the photometric beams are extracted before combination. The principle of a beam combiner is depicted in Figure 2.2. Beam combination occurs in the encircled area.*

Analysing Optics The two interferometric and the two photometric beams then pass analysing optics. A filter wheel with 12 positions for various narrow and broadband filters, neutral density filters, and mounting frames for spectral references. Figure 3.9 shows the transmission of some of MIDI's filters. The spectral reference is discussed in section 4.4. After the filter wheel, two optional dispersive optical elements may be used, a grism with a spectral resolution $R_g = (\lambda/\Delta\lambda) = 260$ and a prism with $R_p = 30$. Further dispersive elements might be added in a later phase of MIDI's lifetime.

Cameras As the last optical unit, MIDI offers three different cameras, all fabricated from Germanium with anti-reflection coatings. The spectroscopic camera is used with the dispersive optics. It focuses the beams on the detector such that the sampling of the Airy diameter λ/D is done by 1 pixel in spectral and 2 pixels in spatial direction. In other words, the pixel scales are $0.26''$/pixel and $0.13''$/pixel respectively[9]. For imaging the sky on the detector and performing field interferometry, one may choose the so-called field camera with a pixel scale of $0.086''$/pixel and therefore 3 pixels per λ/D. An important tool for alignment purpose and functional verification is the pupil camera which allows viewing of the MIDI internal pupil with a diameter of about 40 pixels.

Detector The final component is a Raytheon array. This detector has 320×240 pixels with a size of $(50\,\mu\text{m})^2$. Its main performance specifications at an operating temperature of about 10 K are a dark current of ≈ 100 electrons per second, a readout noise of ≈ 1000 electrons, and a well capacity of $\approx 10^7$ electrons with an overall quantum efficiency of about 40 %. The predicted minimum readout time is 1.4 ms, which corresponds to a maximum full frame rate of 700 Hz. In practice, to get rid of extra noise components, readout occurs at 5.6 ms per full frame.

---

[9] Compare to telescope parameters, page 17.

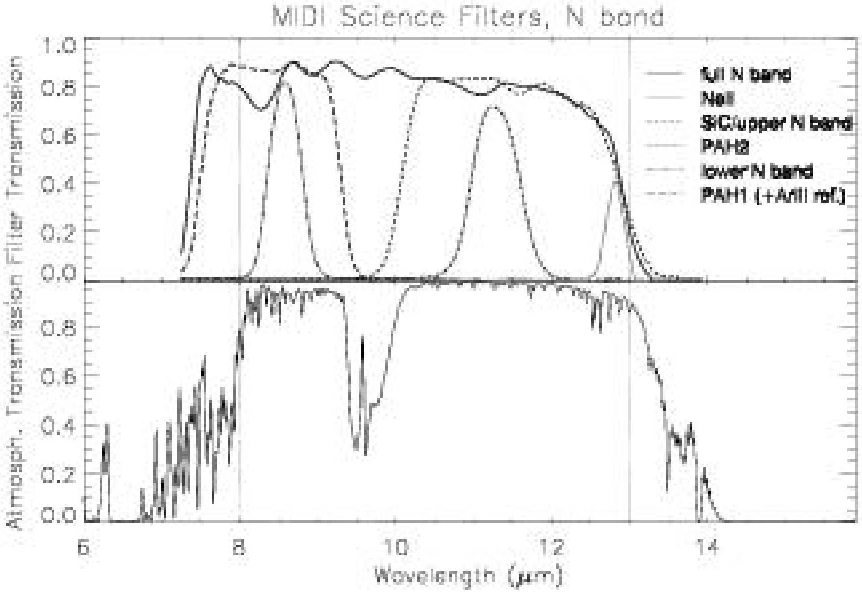

Figure 3.9: Science filters in MIDI. *The diagram shows a selection of the filters available in MIDI (Przygodda, 2001) and for comparison the atmospheric transmission window (see Figure 3.5).*

Chapter 4

Calibrations

4.1 Overview

The following overview points out some of the critical aspects which have to be considered for MIDI as an optical pupil-plane interferometer with additional spectral capabilities:

- *optical alignment* of each individual beam and with respect to each other – no vignetting should occur, proper (position and direction) alignment on the beam combiner is necessary to achieve high interferometric contrast, correct placement on the detector for read-out

- *photometric calibration* – transmission respectively reflection of all optics involved, consider polarisation effects if necessary; efficiency of the detector, linearity, various noise sources

- *spectral calibration* – define position of spectrum and dispersion on detector, determine spectral resolution

- *mechanical behaviour* of Internal Delay Line – static and dynamic properties; vibrations caused, e.g., by the Closed Cycle Cooler (CCC)

- *interferometric performance* – surface quality of all optical parts; special focus on beam combiner as “heart” of the interferometer: thickness, absorption and ghost reflections, wedge angle, splitting ratio, differential phase shifts between different polarisation angles

All these aspects refer mainly to instrument properties that can be tested, optimised, and calibrated in the laboratory. One main emphasis of this work was put into this context. This chapter presents in section 4.2 the results of tests performed on the Internal Delay Line. In order to provide tools for the broad field of tests requiring light, adequate sources had to be designed and realised. This task is addressed in section 4.3. In the following section 4.4 some simple tools for a spectral calibration are presented.

Once the instrument is to be commissioned at the VLTI, other additional, important aspects have to be considered. For example, the interface with the VLTI optical train has to be taken care of. The relatively high number of mirrors in the train contributes to a high mid-IR background. The major change, though, when starting observations is the Earth’s atmosphere which is between the instrument and the object observed. Also the atmosphere contributes by a high background (see section A.1), yet in addition this contribution varies considerably with time (see section 3.2.3).

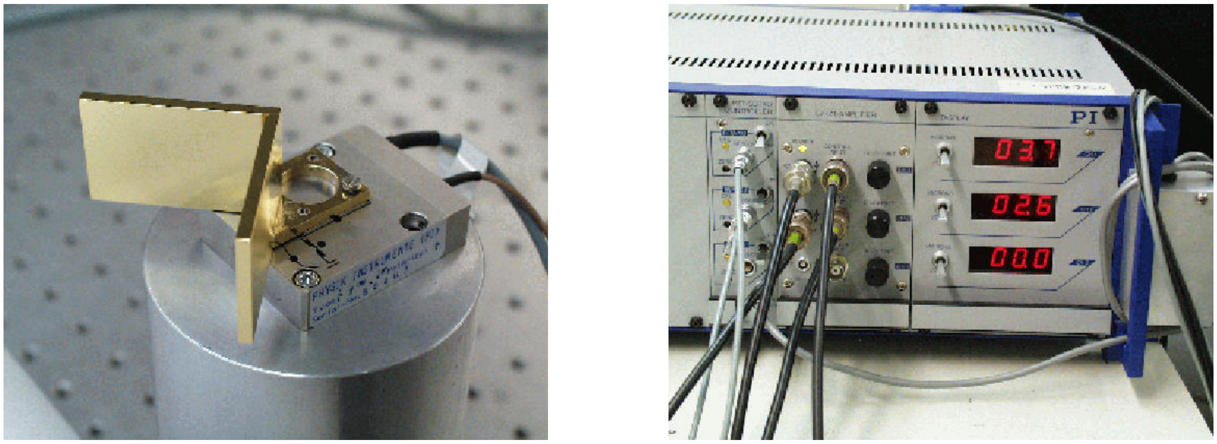

Figure 4.1: Piezo stage and electronics. *Left: One of the two piezo stages carrying a roof mirror mounted in a test setup. Right: Driver electronics for the two stages. One can see the servo module, amplifier, and display module (from left to right).*

In order to calibrate during observations for these effects caused by the mentioned reasons, calibration stars are used (see section 5.1). These calibrators are required to be objects with well-know properties both in spatial and spectral respect. Their observations can reveal atmospheric effects which, in turn, helps extract the useful information on the scientific target.

4.2 Performance of Optical Path Length Modulators in MIDI

4.2.1 Overview

For adjusting and modulating the OPD in MIDI, in each of the incoming beams there is a piezo translation stage carrying a gold-coated monolithic roof mirror made of Beryllium. The piezo stages were chosen from Physik Instrumente, model P-780.20, with the serial numbers 80466 and 80467. In the following, these are called P66 and P67.

The stages are driven and controlled by modules of the Physik Instrumente E-500 product line (see Figure 4.1). Each one of the stages is driven by a specially assigned output of an E-503.00 amplifier with an average output power $\bar{P_T} = 6\,\mathrm{W}$ per channel. P66 is operated by Channel 1 and P67 by Channel 2. Input voltages of the drivers are permitted in the range -2. . . 12 V and are applied to the piezo stages, amplified roughly 10 times. Considering input voltages, the response ϵ of the piezo stages is specified as $\epsilon \approx 8\,\mu\mathrm{m/V}$. Therefore, the maximum stroke of the piezos is roughly 110 µm.

The actual movement of the stages are measured by an inductive sensor. This sensor allows to compensate for drifts and hysteresis by means of a control loop. For each driving channel, the Position Servo Control Module E-509.L3 provides a control loop, which can be switched on or off by a switch. Furthermore, it is possible to adjust the properties of a control loop, e.g., the step response, to different behaviour of piezos or to current requirements. A third driving and control channel, usually not used, offers the option to test changes of the control loop properties first, prior to applying them to the channels in use.

Finally, the display module E-515.03 shows the actual position of each piezo stage. One can toggle the display between absolute displacement in µm and applied output voltage of the driver.

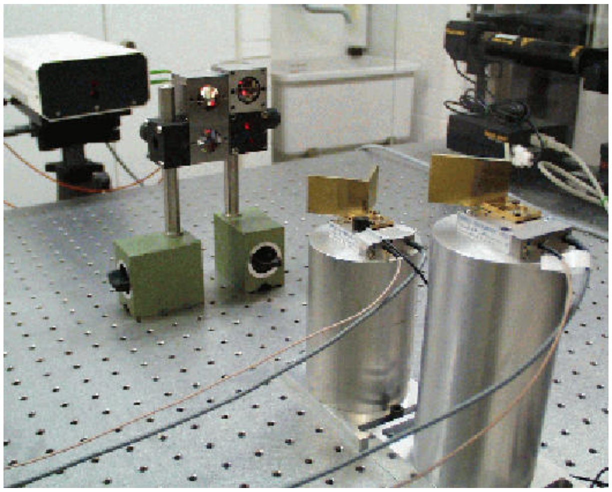

Figure 4.2: Piezo test setup with HeNe interferometer. *The laser head is visible in the top left corner of the image. The beam splitter unit and the retro-reflectors are placed in front of it and close to each other. The beams run in different heights so that the piezos are both included in the interferometer.*

To study the quality of the position control, the two roof mirrors RM1 and RM2 with masses $m_{RM1} = 17.5\,\mathrm{g}$ and $m_{RM2} = 18.2\,\mathrm{g}$ were mounted on their respective piezo stages. Including screws etc., the total masses mounted on the stages were $m_1 = 18.3\,\mathrm{g}$ and $m_2 = 19.0\,\mathrm{g}$. The stages were set up on a vibrationally damped optical table under a plexi-glass cover to prevent significant air turbulences which could falsify the results. As measuring system we used the dual-frequency HeNe laser interferometer ZLM 500 (JENAer Messtechnik, Jena) with a resolution of up to $\pm 2.5\,\mathrm{nm}$, depending on operational mode (see Figure 4.2), and operated by a PC program. With an ADC installed in a second, independent PC the input and output voltages of the electronics were also monitored. The ADC had 12 bits at an input range of $\pm 10\,\mathrm{V}$ and thus a voltage resolution $U_{LSB}^{ADC} = 4.9\,\mathrm{mV}$ corresponding to the least significant bit (LSB).

It was intended to perform tests under conditions that were as similar as possible to the expected actual MIDI setup. Therefore, a test setup was chosen which included one roof mirror in each interferometric arm of the ZLM interferometer. The input voltage for the amplifier was generated by a VME board like the one used for MIDI with a 12-bit DAC. It has an output voltage range of $0 \ldots 10\,\mathrm{V}$ and thus a voltage $U_{LSB}^{VME} = 2.4\,\mathrm{mV}$, which means $S_{LSB} \approx 0.020\,\mu\mathrm{m}$ for the mechanical stroke. In order to command the VME system, a software control module was developed which also entered into the MIDI operating software (Mathar et al., 2001, section 3.3).

In the test results presented hereafter, most length values are given as mechanical values unless stated otherwise. To obtain the values for the OPD between the two beams, one has to multiply the *mechanical* values by a factor of 2 for the *optical* path.

4.2.2 Results

Response to applied voltage In order to characterise the response of the electronics/piezo stage system and find its response curve, we applied an input signal shown in Figure 4.3. The duration of each step was slow enough, i.e., quasi-static, so that dynamic effects were avoided. The respective mechanical movement of the two piezo stages and the resulting response curves are shown in Figure 4.4.

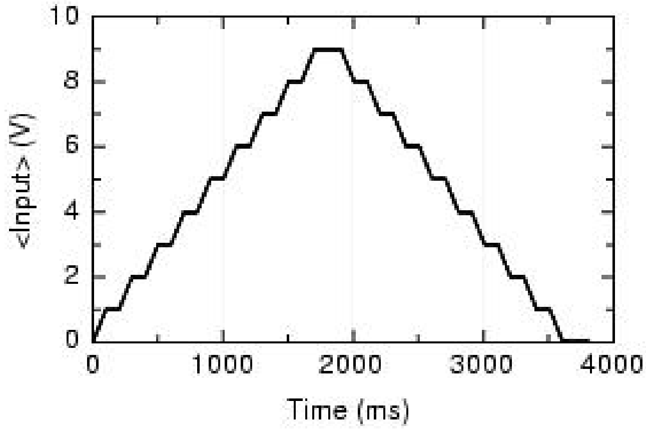

Figure 4.3: Input signal for piezo tests. *Ramps and plateaus are 100 ms long each. Voltage step size is 1 V.*

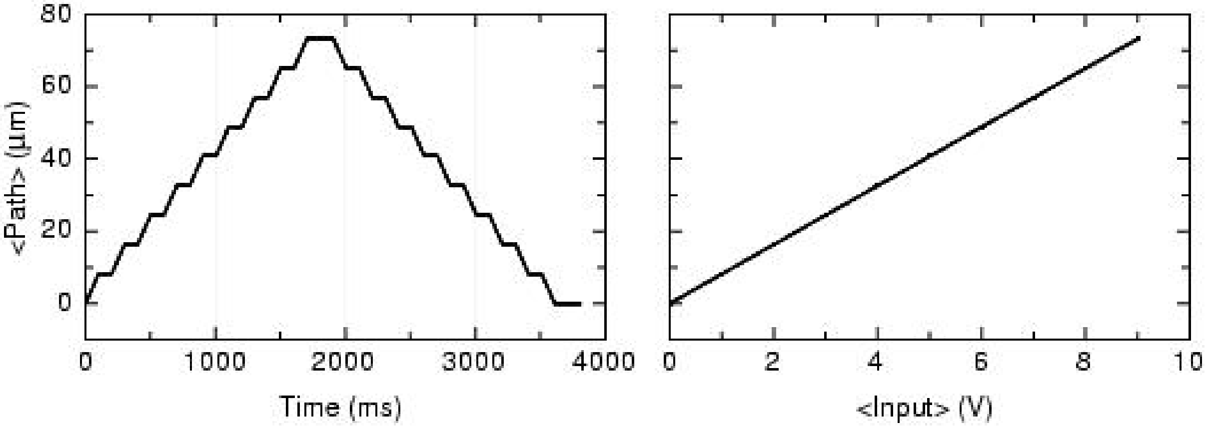

Figure 4.4: Piezo response. *Left: Time dependent response; Right: Response curve.*

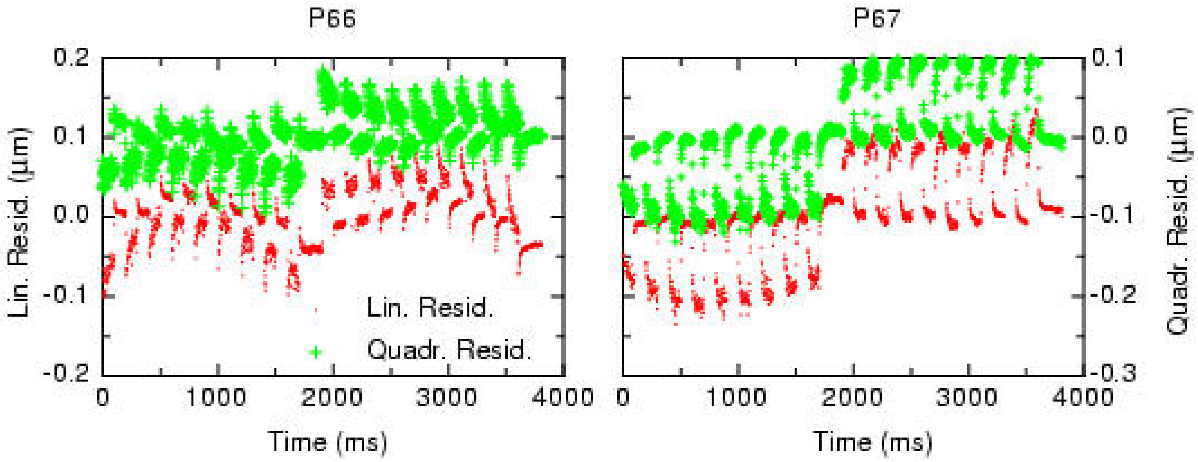

Figure 4.5: Residuals after fit of response. *Note the shifted scales for linear and quadratic fits. The difference between actual and expected position is shown for both piezo stages. When commanding the piezo to move during ramp periods, it always lacks behind, which is the reason for the "outliers" above and below the zero value. In the case of linear fitting (dots), the residual shows obviously a quadratic progression which is not present after quadratic fitting (crosses).*

In a first attempt to characterise the response, and expecting a linear behaviour as claimed by the manufacturer, the curves were fitted by Linear Regression. This yielded the two numbers $\bar{\epsilon_1} = 8.135\,\mu\text{m/V}$ and $\bar{\epsilon_1} = 7.918\,\mu\text{m/V}$. With these numbers and the input signal the two expected mechanical movements were calculated and the measured signal was subtracted. Figure 4.5 shows the residuals.

Apparently, the response curve contains also terms of higher than only linear order. In general, the piezo response is described by $\epsilon(U) = dS(U)/dU$. To consider second order terms, one can assume a quadratic form of the response curve, namely

$$S(U) = a_2 \cdot U^2 + a_1 \cdot U + a_0 \quad , \tag{4.1}$$

which means for the piezo response:

$$\epsilon(U) = \frac{dS(U)}{dU} = 2 \cdot a_2 \cdot U + a_1 \quad . \tag{4.2}$$

A quadratic form has also the advantage to be invertible analytically, which is convenient for the MIDI case where certain *positions* are defined and the corresponding command *voltage* should be chosen by the software. In Table 4.1 the fit parameters are given for the quadratic fit. The residuals of a quadratic fit can be seen in Figure 4.5. The parameter a_0 is not really meaningful, since a constant offset of the piezo system can easily be introduced e.g. by thermal drifts (see below), but can also easily be compensated for during data acquisition.

Table 4.1: Parameters for quadratic fit of piezo response curves.

	a_2 (µm/V^2)	a_1 (µm/V)	a_0 (µm)
P66	-0.00292 ± 0.00003	8.16144 ± 0.00032	-0.04118 ± 0.00062
P67	-0.00104 ± 0.00007	7.92704 ± 0.00064	0.02509 ± 0.00125

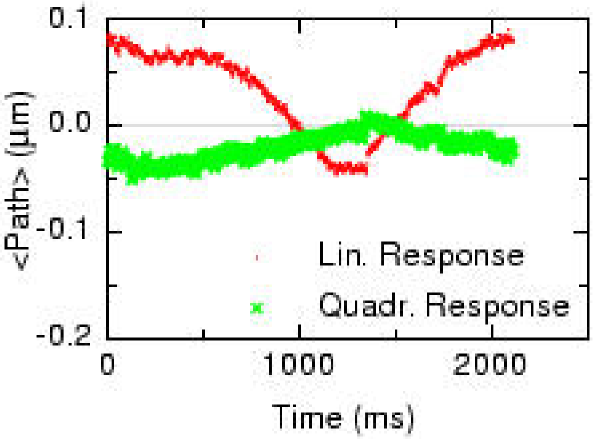

Figure 4.6: Verification of piezo tests. *The fit parameters were inserted in the driving software. Both piezo stages were commanded simultaneously to the same positions. The input signal was similar to the one shown in Figure 4.3, yet the ramp duration was set to zero.*

The respective fitted numbers were inserted in the driving software. As a verification of this method, both piezo stages were commanded simultaneously to the same positions, covering almost the full accessible stroke (≈ 72 µm), with a command signal similar to the one shown in Figure 4.3. One should expect that with a well-enough described system the resulting interferometric signal should remain zero all the time, since both stages perform the same changes to the optical path. Figure 4.6 shows the result of this verification performed several days later. This also allows to estimate how adequately the numbers found in one particular test describe the system in general. One can see that assuming a quadratic response curve yields a maximum piston error roughly three times smaller than assuming a linear curve. Varying the curve parameters slightly during the verification test around the values found by the fitting procedure described above, no substantial improvements of the OPD signal could be obtained. This lets one assume that the remaining OPD signal is mainly caused by higher order terms in the response curve. The maximum piston error $\bar{R}_{max} = 0.05\,\mu\text{m}$ in the "quadratic" case corresponds to an OPD of 0.1 µm which is 1 % of the central MIDI wavelength $\lambda_{MIDI} = 10\,\mu\text{m}$.

Stability With the position controllers switched on for both piezo stages, the piezos showed a noise amplitude of $\pm 8 \ldots 9\,\text{nm}$ (RMS) and a peak-to-peak amplitude of up to 70 nm. This was independent of the offset of the command signal. As one can see in Figure 4.7, the frequency spectrum of the noise showed a peak at $\nu_0 \approx 940\,\text{Hz}$. According to manufacturer information, this corresponds roughly to the resonance frequency of the piezo control loop.

Considering long term stability, we observed a drift $D_{tot} = 6 \ldots 60\,\text{nm}$ per 10 min[1] depending on the operating time of the experimental setup. The "shorted" ZLM itself, i.e. the optical arms of the interferometer covered with retro-reflectors, showed a drift $D_{ZLM} = 2 \ldots 60\,\text{nm}$ per 10 min over a test period of 16 hours. This allows to consider the piezo stage system as stable on long time scales.

---

[1] It has been estimated that typically the acquisition of one data point with MIDI in observing mode will take roughly 10 minutes.

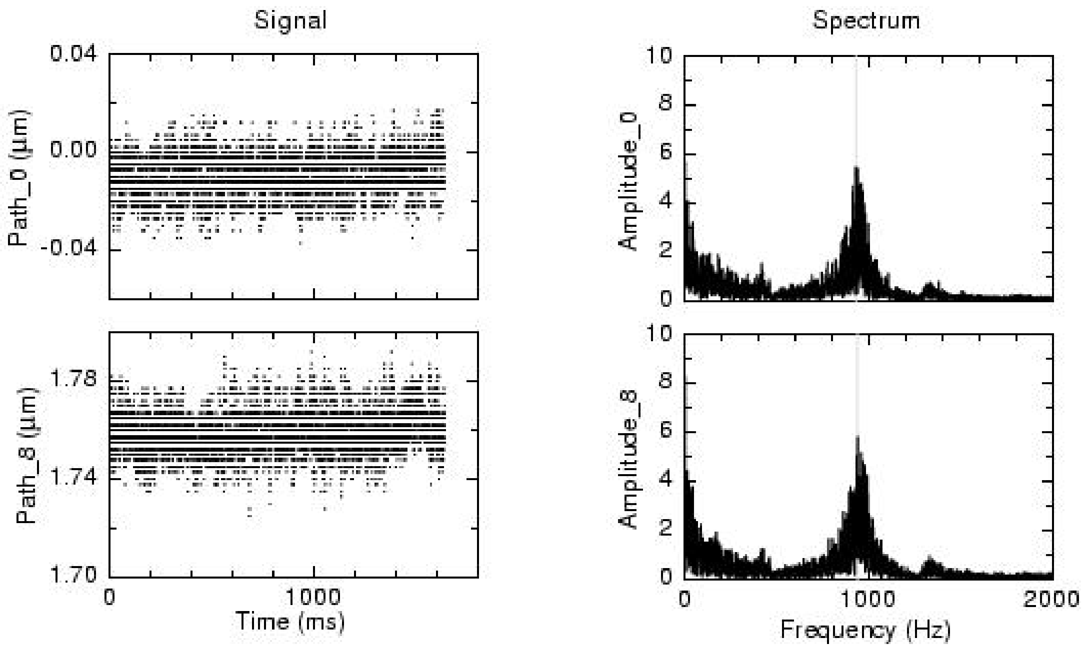

Figure 4.7: Noise and its spectrum of a piezo stage. *The signal is shown at 0 V and 8 V input voltage, therefore the offset of the path axis is different in each case. Units of the amplitude are arbitrary.*

Simulating internal OPD scanning For testing one of the possible internal OPD scanning modes, we applied a 5-step function[2] as command signal setting the piezo in *optical* steps of $\lambda_{MIDI}/4 = 2.5\,\mu\mathrm{m}$ and a step duration of 20 ms. Both the command and the response signal are shown in Figure 4.8. As one can see in Figure 4.9, the time it takes the piezo to move from 10% to 90% of the average step height is $T_{10/90} \approx 2\,\mathrm{ms}$. Resonance oscillations are also visible with an initial peak-to-peak amplitude of $O_{pp} \approx 0.2\,\mu\mathrm{m}$ and a period $T_{osci} = 1\,\mathrm{ms}$, the latter corresponding to the reciprocal value of the resonance frequency found in Figure 4.7. The oscillations are damped to ≈ 50 % after 5 ms.

Other possible observation modes require the internal OPD to be changed in a long ramp at a uniform speed corresponding to a few interferometric fringes within co-phasing time (for MIDI assumed as 100 ms). Figure 4.10 shows the piezo overall movement for an *optical* speed of 10 fringes/100 ms. The overshoot at the plateaus is roughly three times the magnitude of the peak-to-peak noise of the piezo (e.g. see Figure 4.7), i.e., 0.1 µm mechanically yielding an OPD of 0.2 µm. The settling time of the overshoot is $T_{set} \approx 10\,\mathrm{ms}$.

The difference between actual movement and expected position is shown in Figure 4.11. A constant value means that the piezo stage follows the command signal with the appropriate speed, even though with some constant offset. As can be seen in Figure 4.11, the difference creeps for about 50 ms over ≈ 0.15 µm into an almost constant level. These values went down by a factor of ≈ 2 when the piezo speed was reduced to 5 fringes/100 ms, i.e., half the speed.

Tip-tilt deviation In a different experimental setup, the tip-tilt angle of the piezo was measured by the deviation of a reflected HeNe laser beam off a plain mirror mounted in place of the roof mirror. The detection of the expected small angles should allow an accuracy better than 1/10 of the FWHM of the Airy disk of the MIDI Cold Optics, which is

---

[2] In contrast, the mode shown in Figure 2.6 applies four steps of size $\lambda_{MIDI}/4$ and duration 25 ms.

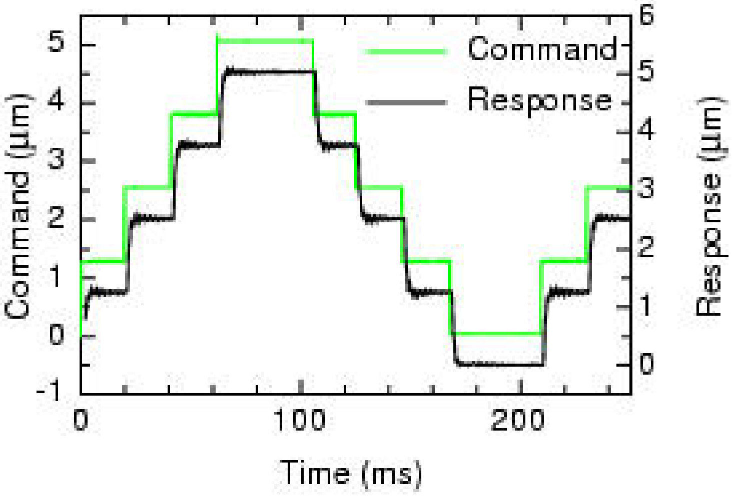

Figure 4.8: Stepping scanning mode. *Note the different scales of command and response. The internal OPD stays constant over a plateau duration of* $\approx 20\,ms$. *The total* mechanical *stroke is* $\lambda_{MIDI}/2 = 5\,\mu m$.

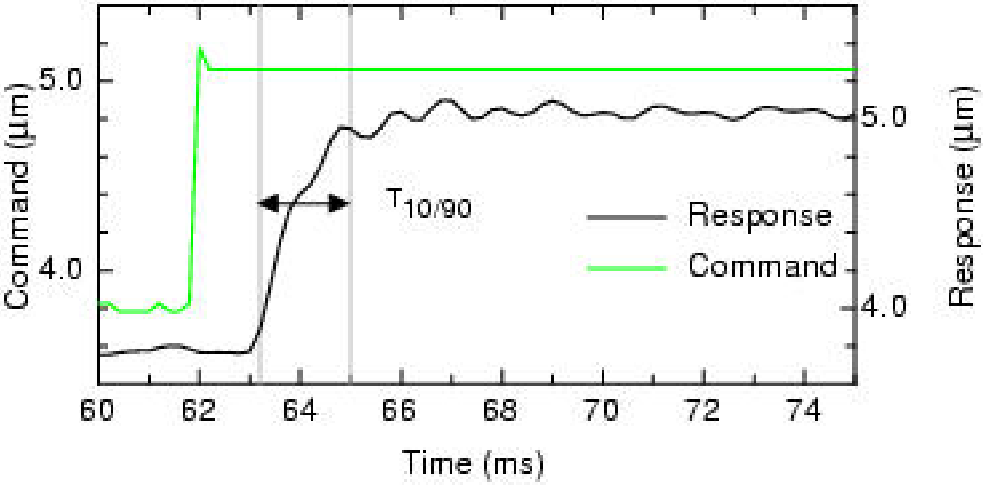

Figure 4.9: Step response of the piezo. *Note the different scales of command and response. The rising time is* $T_{10/90} \approx 2\,ms$.

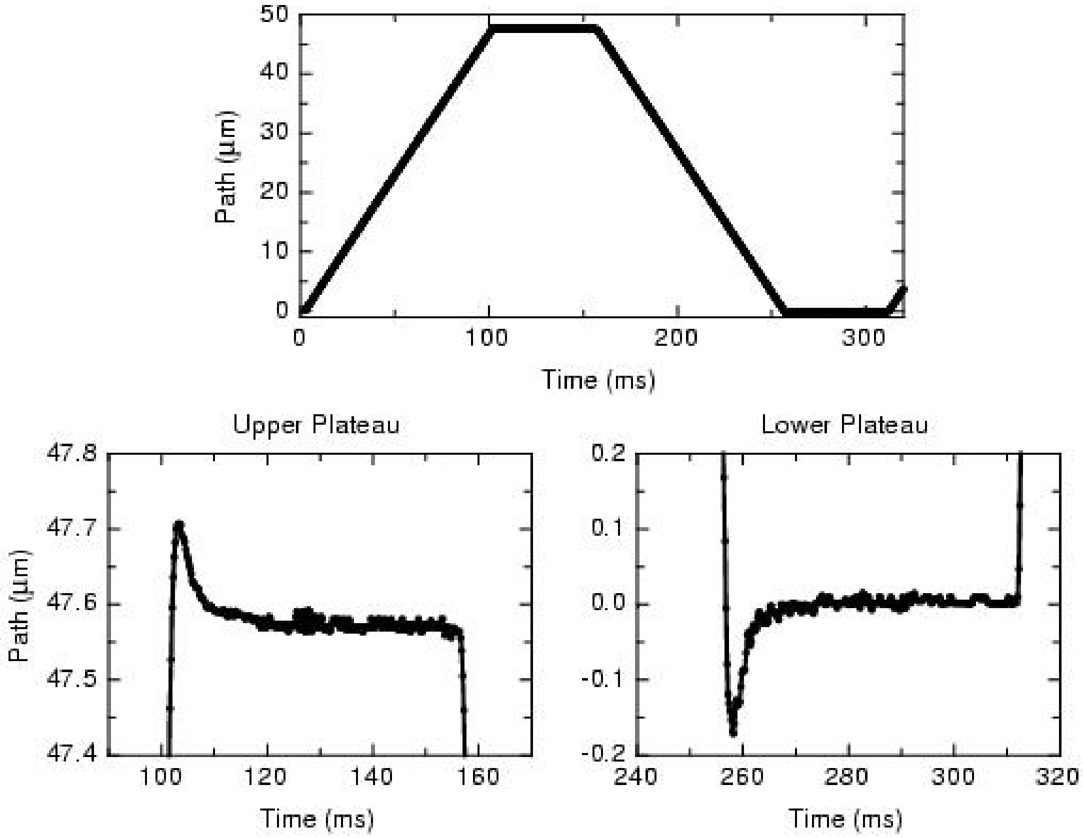

Figure 4.10: Fourier scanning mode. *Long ramp movement and overshoot.*

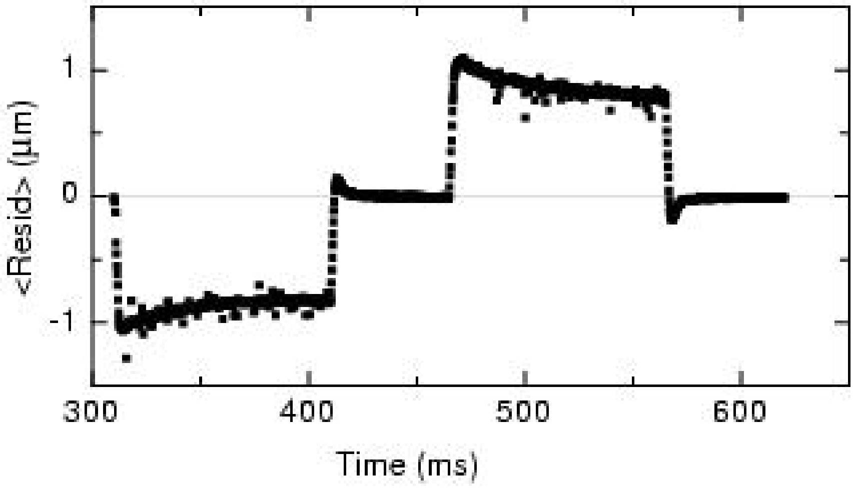

Figure 4.11: Fourier mode residual. *Difference between actual movement and expected position of long ramp movement. The data noise is reduced by averaging several cycles prior to fitting.*

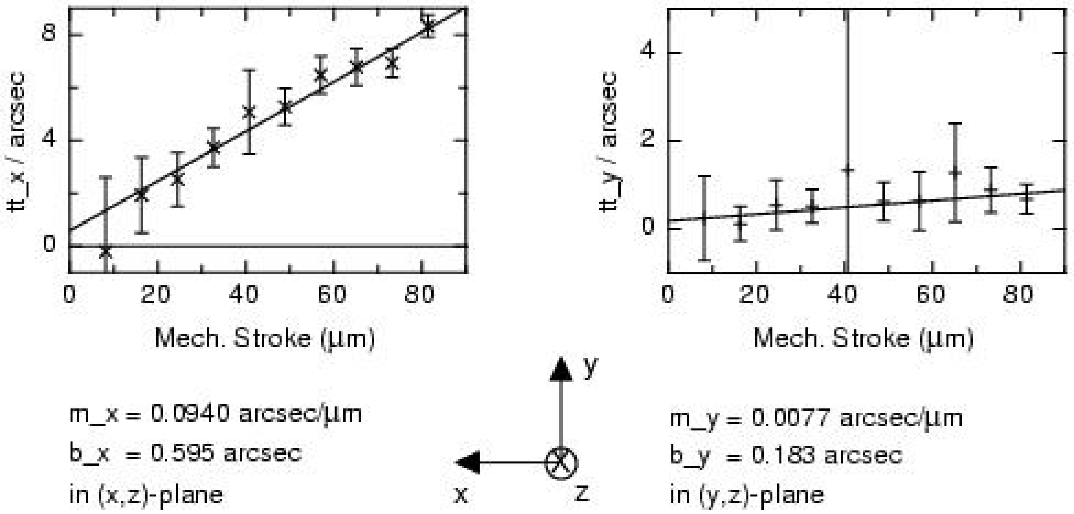

Figure 4.12: Tip-tilt angle of piezos. *It was measured parallel and perpendicular to the beam plane (x,z). The beam plane was parallel to the optical table.*

$\phi_{tt} = \lambda_{MIDI}/(10\,D) \approx 10''$, where $D = 18\,\mathrm{mm}$ is the beam diameter delivered to MIDI. The beam was recorded on a CCD with a pixel size of $p = 15\,\mu\mathrm{m}$, placed at a great distance d away ($d \approx 14\,\mathrm{m}$) from the piezo stage. The angular resolution was therefore $\alpha_{detect} = p/d = 0.22''$. The piezo was commanded by a DC voltage U_{tt} in a quasi-static way alternating several times from 0 V to U_{tt} to allow compensation for drifts.

The results of tip-tilt measurements are shown in Figure 4.12. The piezo stage was moving in the (x,z)-plane parallel to the table surface. The tip-tilt angle in the (x,z)-plane is compensated by the roof mirror[3] mounted on the piezo stages. The angle in the (y,z)-plane is ≈ 12 times smaller, i.e., about $1''$ maximum.

4.2.3 Discussion

The values presented in the previous sections are found to be all well within acceptable limits for 10-µm interferometry. Both the piston mismatch $\bar{R}_{max}$ and the noise values induced an OPD of the order of 1 % of $\lambda_{MIDI} = 10\,\mu\mathrm{m}$ which are maximum numbers. Likewise, the tip-tilt angle in the critical direction, i.e., in the (y,z)-plane was a factor 10 below the minimum requirement ϕ_{tt}.

The effects observed in the OPD scanning modes were slightly higher. In the stepping mode, the resonance peak-to-peak amplitude O_{pp} caused an OPD corresponding to 4 % of λ_{MIDI}. Yet, the applied command steps were very abrupt. They can be chosen smoother since there is, in any case, the requirement to read out the detector between two steps which allows at least this read-out time to move the piezos. Applying a long ramp as command signal, the overshoot does no harm since measurements are taken during the ramp period. The creep occuring during this time induced a 3 % effect which is sufficiently small for this scanning mode.

---

[3] See footnote 7 on page 27 for properties of such a mirror.

Table 4.2: Calibration light sources.

light source	purpose
broad-band, extended and uniform	– provision of minimum signal and known stimulus – stability – internal vignetting
narrow-band/laser, unresolved	– wavelength calibration – rough interferometric alignment – $\Delta\, OPD$ calibration of Internal Delay Line – maximum visibility calibration
broad-band, continuous	– calibration of constant flux; variety of available pinholes, resolved to unresolved – $OPD = 0$ ("white light fringe") – wavelength calibration with foils – broad-band visibility calibration
broad-band, electronically chopped	– like the continuous source, but calibration of modulated flux

4.3 Calibration Light Sources

For various laboratory test and verification purposes, the MIDI instrument needs artificial light. The various purposes can be divided in three groups which are served by light sources differing in kind and spectral width. In Table 4.2 an overview is given of the different sources and the purposes they serve. The following paragraphs focus on the narrow-band and on the unresolved broad-band source as their design was a major task of this work. For the extended broad-band source, refer to section 3.3.1.

Parts of this present section where already presented in Schuller et al. (2000).

4.3.1 The Monochromatic Source

For calibration of the wavelength, ΔOPD, and visibility MIDI will use the monochromatic light of a CO_2 laser. To meet MIDI requirements, its output power had to be attenuated by an optical setup as shown in Figure 4.13. Both the laser and the optical setup are mounted on an optical table.

The laser (model 3622 by Ultra Lasertech Inc., Brampton ON, Canada) is polarised horizontally with respect to the optical table (degree of polarisation $\approx 50:1$ between the two polarisation directions). It has an output power range of $0.6 \ldots 6$ W at 10.6 µm and is manually controlled by a current setting at the control electronics. Its beam diameter at $1/e^2$ intensity level is 3.8 mm. This results in an average[4] flux density of $5 \ldots 50\,\mathrm{W/cm^2}$. At the output aperture there is a laser diode emitting visible light at 670 nm (red) which allows alignment of subsequent optics. In order to keep thermal expansions of the laser head low, which could effect wavelength stability, the laser has an Invar housing and is cooled by a water cooler.

The MIDI detector chip has a saturation level for one pixel of 10^7 electrons, which translates

---

[4] Further remarks on this number can be found in section A.3.1.

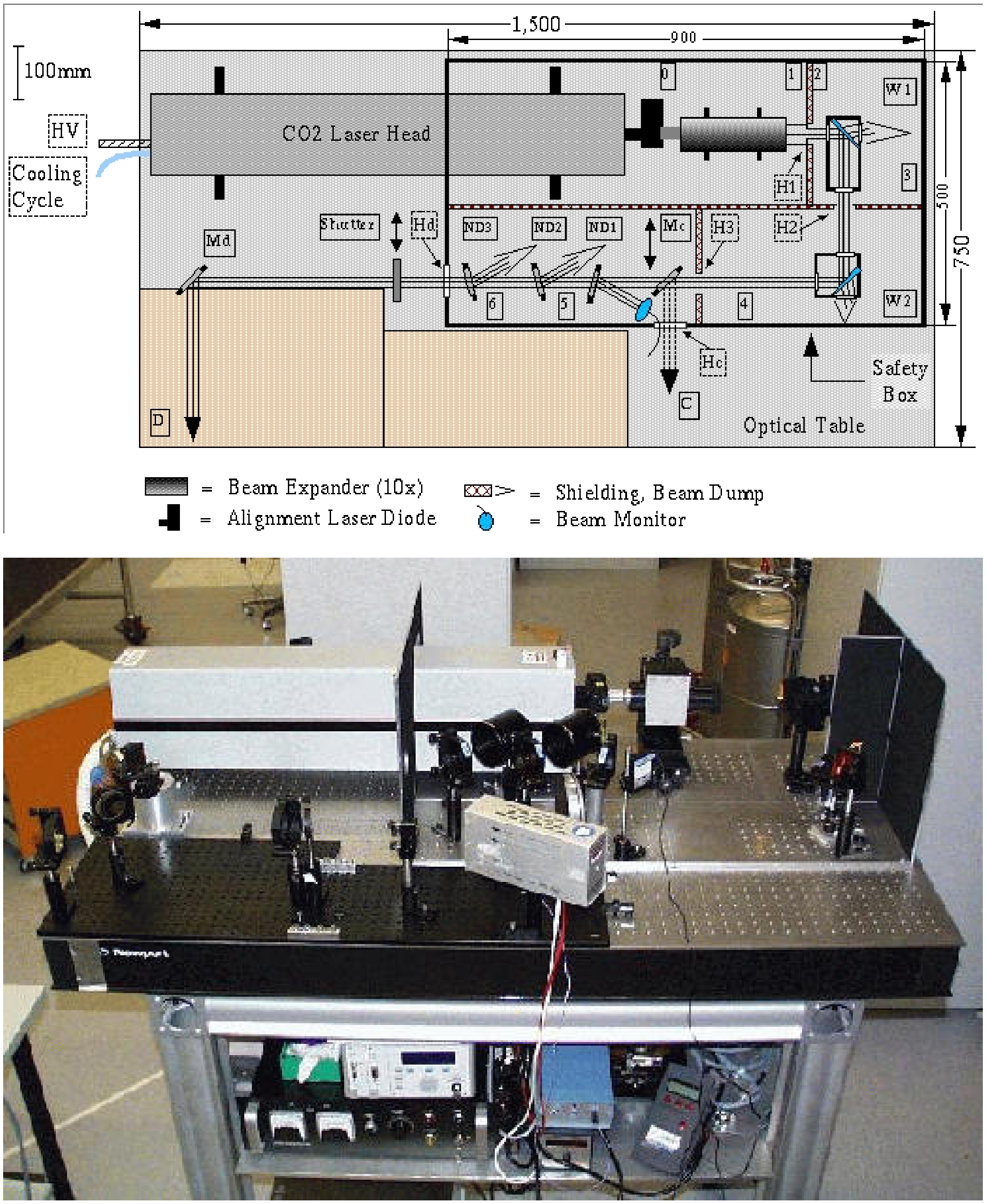

Figure 4.13: CO$_2$ laser with attenuation. *The optical elements are collected in Figure 4.3, numbered beam parameters are found in Table 4.4. Beams C and D go to the optional IR camera and to the detector respectively. The shaded area at the bottom left of the drawing indicates the breadboard contours of the broad band source described in section 4.3.2. In the photograph, parts of the safety box were removed for a clear view.*

Table 4.3: Optical elements used in laser beam attenuation. *All optical elements are made of ZnSe with appropriate coating.*

Element	Function
Beam Expander	expands beam by factor 10; telescopic system of two lenses
W1, W2	wedge, $R_{W1} = 0.5\,\%$ and $R_{W2} = 5.0\,\%$
ND1, ND2, ND3	neutral density, $T = 1\,\%$

by[5]

$$I_{sat} = \frac{E_\gamma n_{sat}}{\eta T_{CO} t_{int}} = n_{sat} \cdot 2.3 \cdot 10^{-18}\,\mathrm{W} \tag{4.3}$$

to $I^D_{sat} \approx 0.9\,\mu\mathrm{W/cm}^2$. To bring down the output power to a level matching with I^D_{sat}, an adequate optical layout had to be designed and established. This is described in the next paragraph. At the same time, operational safety had to be considered. Respective remarks are found in the following paragraph.

Optical Setup

To bring down the output power to a level matching with I^D_{sat}, several stages of attenuation have to be applied. The elements used for this purpose are listed in Table 4.3. The fractions of the beams not used are trapped and dissipated. To avoid potential central hole burning as soon as possible in the optical train, we apply a beam expander in the first place, which is a telescopic system of two lenses enlarging the beam diameter by a factor of 10 and hence reducing the flux density by a factor of 100.

After reducing the beam diameter from 38 mm (nominally) to 20 mm by an aperture, there are two wedges W1 and W2 with reflectivities $R_{W1} = 0.5\,\%$ and $R_{W2} = 5\,\%$ for both s- and p-polarised light. They are designed to strongly divert reflections from the back surface so that these can be trapped and do not interfere with the main beam. The mount of W1 provides space for up to four additional CaF_2 plates, each with a transmission of 60 % at 10.6 µm which corresponds to 0.55 mag in brightness. By this means it is possible to simulate a range of 2.2 mag.

At this position the beam parameters are at a level convenient for laboratory testing of optical components in Heidelberg. Therefore we introduce an optional mirror Mc and an extra output, which are normally not used on Paranal. As a detector we use an IR camera (Pyroviewer, model 5450 by Electrophysics, Fairfield NJ, USA) which has a saturation level $I^C_{sat} \approx 200\,\mu\mathrm{W/cm}^2$ and a destruction level of $I^C_{destr} \approx 1\,\mathrm{mW/cm}^2$.

For the MIDI detector chip its saturation level $I^D_{sat} \approx 0.9\,\mu\mathrm{W/cm}^2$ is to be considered, the MIDI warm optics (von der Lühe et al., 1999) coupling in and splitting the laser beam, and the cold, imaging optics (Glazenborg et al., 1999). As a result, the flux density of the laser beam must be attenuated by an additional factor of $10^{-4}...10^{-7}$, depending on the MIDI camera in use. Thus the beam reflected by W2 (Beam 4) is further attenuated by reflective metal-coated filters serving as neutral density filters ND1, ND2, and ND3 with optical densities OD1=OD2=OD3=2.0, i.e., transmission factors $T_{ND1} = T_{ND2} = T_{ND3} = 10^{-2}$. Here ND3 is removable.

---

[5] For values of parameters see section A.2.

Table 4.4: Beam parameters at different positions using the CO$_2$ laser. *See Figure 4.13 to identify intermediate positions.*

beam	diameter	F (W)	I (W/cm^2)
0	3.8 mm	5.67	50.0
1	38 mm	5.67	0.500
2	20 mm	1.57	0.500
3		$7.85 \cdot 10^{-3}$	$2.50 \cdot 10^{-3}$
4		$3.93 \cdot 10^{-4}$	$1.25 \cdot 10^{-4}$
5		$3.93 \cdot 10^{-6}$	$1.25 \cdot 10^{-6}$
6		$3.93 \cdot 10^{-8}$	$1.25 \cdot 10^{-8}$
C	20 mm	$3.93 \cdot 10^{-4}$	$1.25 \cdot 10^{-4}$
D		$3.93 \cdot 10^{-10}$	$1.25 \cdot 10^{-10}$

Hence with this setup we obtain numbers for the flux F and the flux density I as given in Table 4.4.

Safety Considerations

The optical table carrying the laser source is placed towards MIDI closely to the wall between the Combined Coude Lab and the Interferometric Lab. Thus it is not possible for persons to pass through the laser beam.

The laser and the optical setup are covered by a safety box which is fixed to the optical plate and connected to an interlock system. It is not possible to remove the box accidentally or to access the attenuating optics without triggering the interlock system first which will shut down the high voltage supply for the laser head and therefore IR light output. A flow switch is installed to check the water flow of the cooling cycle for the laser head. It is triggered, if there are considerable discrepancies between the water amount flowing to and from the laser head or if the water flow is too low.

For more information on safety aspects of MIDI, and references of the respective guidelines, see Schuller et al. (2000).

Operation Procedure

It is planned to switch on the laser once or twice per observing campaign in the afternoon before the beginning of an observation night. After performing the required tests for calibration of the wavelength, ΔOPD, and visibility and carrying out possible required adjustments, the laser should be switched off again. It is expected that this takes less than two hours.

PbS Laser Diode as Backup System

In the course of setting up the CO$_2$ laser it turned out that the company producing these lasers does not exist anymore. Because this means that support is not guaranteed anymore in case of failure during laboratory tests of MIDI, it was decided to purchase another backup system. The main objective was to have a monochromatic single mode source. Searching the market for an alternative, a very compact system was found (OLS 150 Tunable MIR-Laser Source

Figure 4.14: Laser diode system. *(Image: Mütek Infrared Laser Systems)*

by Mütek Infrared Laser Systems, Diessen, Germany) which is usually used for infra-red gas analysis (VDI, 1998). Light is produced by a semi-conducting PbS diode contained in a LN2 cooled dewar (see Figure 4.14) which can hold two such diodes in total. Operating temperature of the diode and driving current are set by an electronic system and can be remote-controlled which is a welcome advantage. The light emmitting active zone of the diode is placed in the focus ($f = 40\,\mathrm{mm}$) of an off-axis paraboloid mirror which produces a collimated beam of 14 mm diameter. Nominal output power is roughly 0.25 mW maximum. This results in a flux density of $I_{LD} = 1.62 \cdot 10^{-4}\,\mathrm{W/cm^2}$ which is almost identical to the flux density in beam 4 of the CO_2 laser attenuator. Therefore, in case of failure of the CO_2 laser one can place the diode system in front of the neutral density filters which again weakens the beam to limits suitable for MIDI. The respective beam parameters are listed in Table 4.5.

It is known that this sort of diodes changes the output wavelength with temperature and current. The compact size made it possible to setup the system in front of a spectrograph and take spectra while changing operation parameters. Results are shown in Figure 4.15.

Table 4.5: Beam parameters at different positions using the laser diode. *See Figure 4.13 to identify positions. Compare to the case with the CO_2 laser given in Table 4.4.*

beam	diameter	F (W)	I (W/cm^2)
4	14 mm	$2.50 \cdot 10^{-4}$	$1.62 \cdot 10^{-4}$
5		$2.50 \cdot 10^{-6}$	$1.62 \cdot 10^{-6}$
6		$2.50 \cdot 10^{-8}$	$1.62 \cdot 10^{-8}$
C	14 mm	$2.50 \cdot 10^{-4}$	$1.62 \cdot 10^{-4}$
D		$2.50 \cdot 10^{-10}$	$1.62 \cdot 10^{-10}$

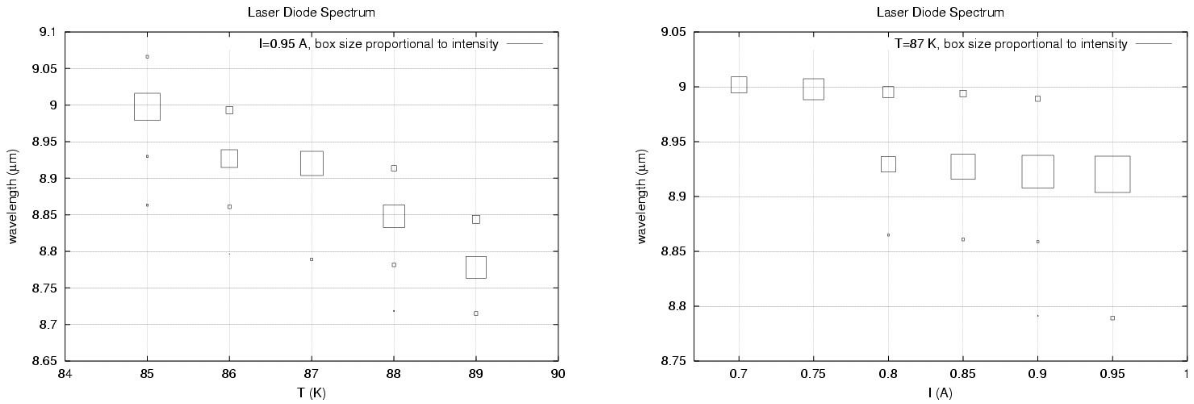

Figure 4.15: Laser diode wavelength. *Left: Dependency on temperature at driving current $I = 0.95\,A$; Right: Dependency on driving current at temperature $T = 87\,K$ (Przygodda, 2001).*

4.3.2 The Polychromatic Unresolved Source

For broadband flux and spectral calibrations as well as finding $OPD = 0$, MIDI needs a broadband source which is well repeatable and which provides parallel light to simulate the two incoming VLTI beams. Such a source is already required and necessary during laboratory tests of MIDI in Heidelberg. For commissioning and operation of MIDI on Paranal, it has been specified that the LEONARDO unit[6] will serve this purpose (Kervella et al., 2000b,a).

The task was to design a low-budget setup which serves the requirements for MIDI. The desired property of being suitable for broad-band yields two consequences. First, only reflecting optics should be used to avoid chromatic effects caused by dispersion. It is obvious, therefore, to ideally choose as the central element a parabolic mirror and place a pinhole, which is smaller than an Airy disk, in its focus. So the second consequence of the broad-band requirement is that the pinhole chosen has to have a diameter smaller than the Airy disk for *all* wavelengths in the band.

Let p be the diameter of the pinhole and ρ the radius of the Airy disk of the parabolic mirror. The condition to fulfil then is

$$p \ll 2 \cdot 1.22 \frac{\lambda}{D} \cdot f_M \quad , \tag{4.4}$$

with f_M the focal length of the paraboloid, D its diameter, and λ the respective wavelength. Considering a 100 µm pinhole, a nominal beam diameter $D = 20\,\mathrm{mm}$ at the entrance window of MIDI, and a band pass from 7 to 14 µm yields for the required focal length $f_M \gg 60 \ldots 120\,\mathrm{mm}$. As one wants to be able to vary the energy throughput by changing the pinhole size by some factor 1.5, one ends up with a minimum focal length of 180 mm. It follows for the f-ratio $(f_M/D) \approx 10$. In addition, one may note that the difference Δx between a parabolic and a spherical mirror, measured at the edge, is (Hecht, 1998, Chapter 5)

$$\Delta x = \frac{1}{2^{10}} \cdot f_M \cdot (f_M/D)^{-4} \tag{4.5}$$

in the leading order. For practical reasons, the dimensions for the mirror were chosen as $f_M = 400\,\mathrm{mm}$ and $D = 50\,\mathrm{mm}$. In fact, MIDI accepts beams of 18 mm diameter. So, directing a slightly oversized 20-mm beam from the broadband source to MIDI means $(f_M/D) = 20$. It follows a $\Delta x = 2\,\mathrm{nm}$ which is $1/500$ of λ_{MIDI}. This is an acceptable number for the present

---

[6] In the future, this unit will be incorporated in the ARAL unit (see section 3.1.3).

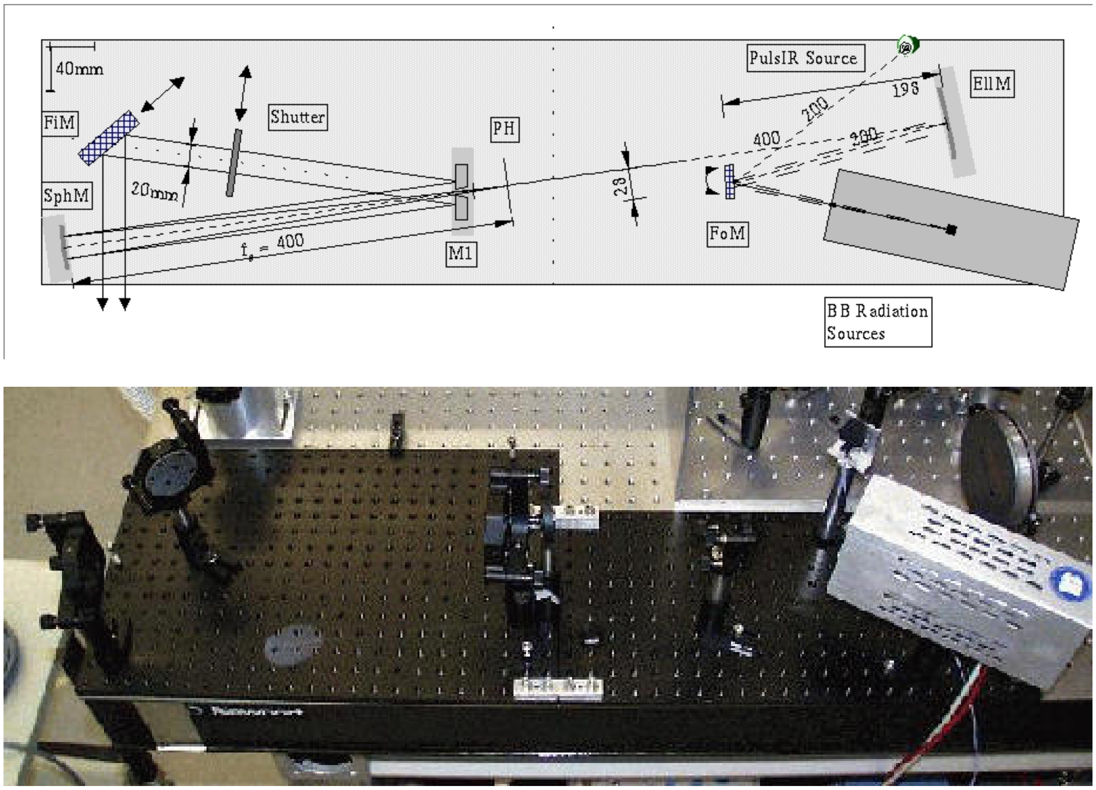

Figure 4.16: Broad-band source with collimating optics. *The flip-in mirror FiM is to be removed in order to let the laser beam pass (see Figure 4.13). Names of optical parts are found in Appendix C.*

purpose, and therefore instead of a more costly paraboloid a spherical mirror was taken for simplicity.

The overall setup of the broad-band source is shown in Figure 4.16. To illuminate the pinhole, a radiation source should be imaged on it. For this purpose an elliptical mirror was chosen with a diameter of 78 mm, a focal length of 400 mm, and an opening angle of 8 degrees. As there was the demand to have both a continuous source and one with a chopping feature, an additional folding mirror (diameter 25 mm) was placed in a way that one can choose between two different sources, yet the optical elements involved in the imaging remain the same.

Continuous Source One of the radiation sources is a commercial black body (model BB 1001, with temperature control 204, Galai Ltd., Migdal Haemek, Israel) which can be heated up to 1 300 K. It was placed in the setup so that its inner, heated part is imaged on the pinhole.

Pulsed Source The second source is an electrically-pulsed filament (pulsIR source by Ion Optics Inc., Waltham, MA, USA) placed in a transistor housing without window. It is driven by a small electronic device and commanded through a serial interface by a PC program. The pulsIR can be operated in a range of temperatures (nominally 200 . . . 900 °C), pulse frequencies, and duty cycles. In this way a mechanical chopper can be saved which makes the setup simpler and more compact.

Photometric tests of the pulsIR source showed qualitatively its main characteristics. In Figure 4.17, the signal for 10 µm wavelength is sketched. All results are summarised in Table 4.6.

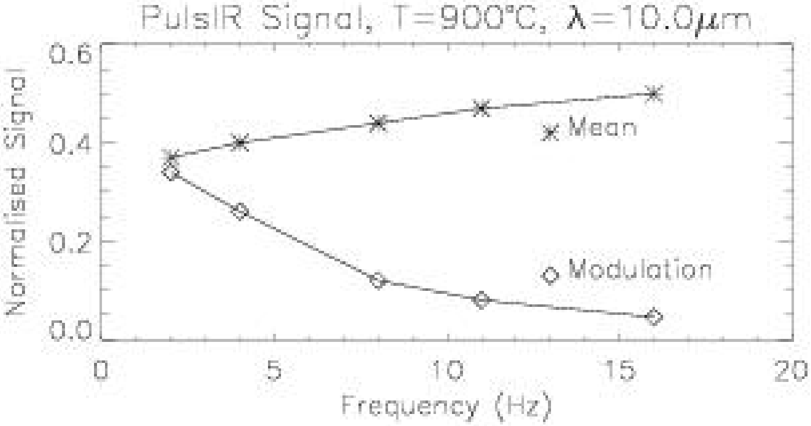

Figure 4.17: PulsIR measurements at constant wavelength. *The diagram shows the pulsIR mean and modulation signal versus the pulse frequency. It is normalised to the signal of a blackbody at* $T = 900\,^\circ C$ *mechanically chopped with* 11 Hz. *Values are given for* 10 µm *and* 50 % *duty cycle (Pitz, 2000).*

The mean signal was only a fraction 0.1 . . . 0.5 of the signal of a mechanically chopped blackbody, the fraction increasing with pulse frequency and its value dependent on wavelength. The modulated signal decreased, also dependent on wavelength, with pulse frequency. Furthermore, it was noticed that the signal amplitude increased by a factor of almost 3 when air was blown over the housing.

This behaviour can be understood by considering the thermal inertia of the filament which at higher pulse frequencies does not have the time to cool completely down to ambient temperature. An air flow accelerates the cool-down process and so a larger amplitude can be measured. In order to keep the signal stable, though, and prevent drafts of ambient air, the filament housing is protected by a foam collar.

Tests were also made on housings with a Germanium window. Germanium is normally used because of its flat transmission curve between 2 µm and 12 µm at roughly 50 % level. It turned out, though, that in this case the window itself was heated and appeared as emitter of infra-red radiation. Its thermal inertia was so high that hardly any modulation signal could be measured. Therefore, this model was rejected.

Table 4.6: PulsIR measurements. *The table gives the pulsIR mean and modulation signal dependent on pulse frequency* f *and wavelength* λ. *The signal is normalised to the signal of a blackbody at* $T = 900\,^\circ C$ *mechanically chopped with* 11 Hz. *Values are given for* 50 % *duty cycle (Pitz, 2000).*

f (Hz)	Mean Signal					Modulated Signal				
	λ (µm)					λ (µm)				
	2.2	4.8	8.5	10.0	12.0	2.2	4.8	8.5	10.0	12.0
2	0.14	0.30	0.39	0.37	0.30	0.33	0.44	0.38	0.34	0.28
4	0.14	0.32	0.39	0.40	0.33	0.30	0.35	0.37	0.26	0.20
8	0.18	0.37	0.47	0.44	0.37	0.19	0.17	0.14	0.12	0.10
11	0.22	0.42	0.49	0.47	0.37	0.16	0.12	0.09	0.08	0.06
16	0.33	0.46	0.51	0.50	0.41	0.11	0.07	0.05	0.045	0.04

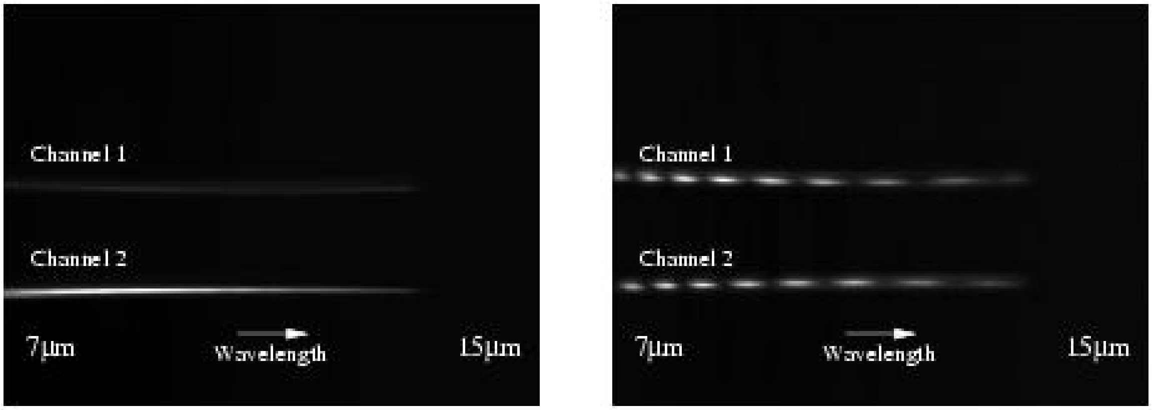

Figure 4.18: Detector images of broad-band interference. *The wavelengths are coarse estimations. Left: OPD is set to nearly zero. Right: OPD set to roughly 140 µm (Przygodda, 2001).*

Verification of Functionality

During first test with the assembled MIDI instrument, the previously described light sources demonstrated their functionality. Mainly with the broad band source, zero OPD was successfully found. In Figure 4.18 two broad band interferograms are shown, one near zero OPD and the second with $\approx 140\,\mu\text{m}$ OPD. Currently, the sources are actively used in laboratory tests of MIDI.

4.4 Spectral Calibration

Because MIDI includes means for spectral resolution (see section 3.3.3), it is necessary to assign proper wavelengths to positions on the detector.

One option for performing this calibration is introducing a foil of a material with a well-know spectrum into the incoming beams which are taken from a source with a continuous spectrum, e.g., a blackbody. The reference spectrum should contain, distributed mainly in the band $8 \ldots 13\,\mu\text{m}$, a number of clear spectral features which allow to pinpoint the according wavelengths on the detector. The task, therefore, was to find an appropriate material, produced as foil with a thickness suitable for MIDI calibration purpose, and to provide a reference spectrum.

As there is no adequate equipment at MPIA to perform spectrally resolved measurements at cryogenic temperatures that occur in the MIDI environment, an institution had to be found that has the equipment for and experience in collecting spectra in the wavelength band in question. A partner was found in the Chemical and Spectroscopical Laboratory at the Astrophysical Institute of the University of Jena, Germany, that carried out all spectral reference measurements described in this section.

As first step, one had to choose possible materials with interesting spectral features. A number of easily accessible and widely used materials were chosen from a collection of spectra (Schrader, 1995) and acquired from manufacturers as foils in a suitable thickness at which it was expected that the absorption lines in the spectral band would not be saturated. In a second step, the spectrum of the chosen materials had to be checked in a coarse overview at room temperature. A basic material from different producers may vary in the exact chemical composition and therefore additional absorption bands may occur in the spectrum. After this quick check, the following materials were selected for cold measurements:

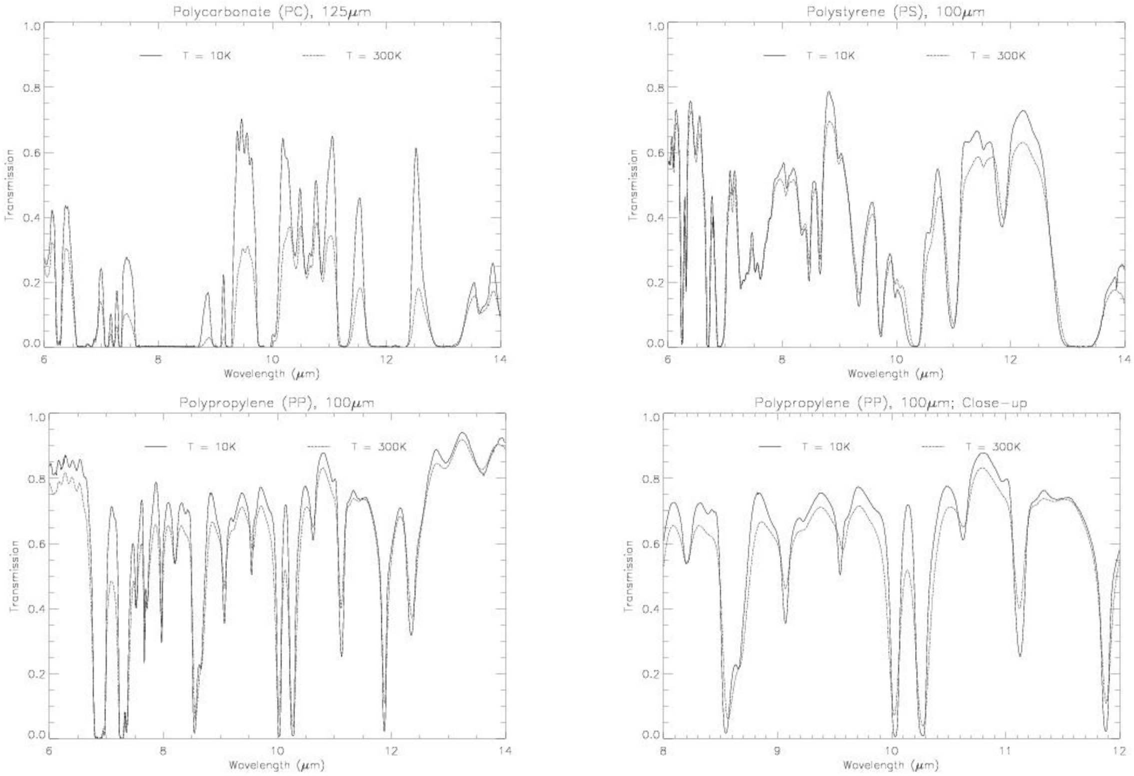
Polycarbonate (PC), 125μm

Polystyrene (PS), 100μm

Polypropylene (PP), 100μm

Polypropylene (PP), 100μm; Close-up

Figure 4.19: Foil reference spectra. *Out of the three tested materials, PP had the most suitable spectral features in the relevant wavelength band, i.e. distinct lines which are not saturated. (Spectra taken at the Chemical and Spectroscopical Laboratory, University of Jena)*

Material	Product Name	Thickness	Producer
Polycarbonate (PC)	Makrofol DE 1-1 CC	125 μm	Bayer AG, Leverkusen
Polypropylene (PP)		100 μm	profol GmbH, Halfing
Polystyrene (PS)[7]	Styrolux 693 D	100 μm	BASF AG, Ludwigshafen

The last step was to take the spectra of these materials roughly at temperatures occuring in MIDI.

In Figure 4.19, one can see spectra of the materials at room temperature and at 10 K. Test measurements taken as comparison during warm-up after the first cool-down cycle of the spectrograph did not indicate any permanent changes of the optical properties of the material. Apparently, the positions of spectral peaks and dips hardly change with temperature. At 10 K, shifts of single peaks by 0.02 μm can be observed, mostly towards shorter wavelengths. A typical FWHM of a sharp absorption line is roughly 0.1 μm. Again, it is slightly smaller at 10 K than at room temperature.

These findings have to be compared with the spectral resolution of the dispersive elements in MIDI. As mentioned in section 3.3, the nominal spectral resolution for the grism is $R_g = (\lambda/\Delta\lambda) = 260$ and for the prism $R_p = 30$. With $\lambda_{MIDI} = 10\,\mu\text{m}$, this means for the wavelength resolution $\Delta\lambda_g = 0.04\,\mu\text{m}$ and $\Delta\lambda_p = 0.3\,\mu\text{m}$, or $\Delta\lambda_{g,px} = 0.02\,\mu\text{m}$ and $\Delta\lambda_{p,px} = 0.2\,\mu\text{m}$ per pixel respectively. Hence, the prism does not resolve the sharp spectral lines which should exactly serve as markers. With the grism, peak positions can be determined well enough. At the same

---

[7] Among other applications, PS is a widely used reference material for IR spectrometers.

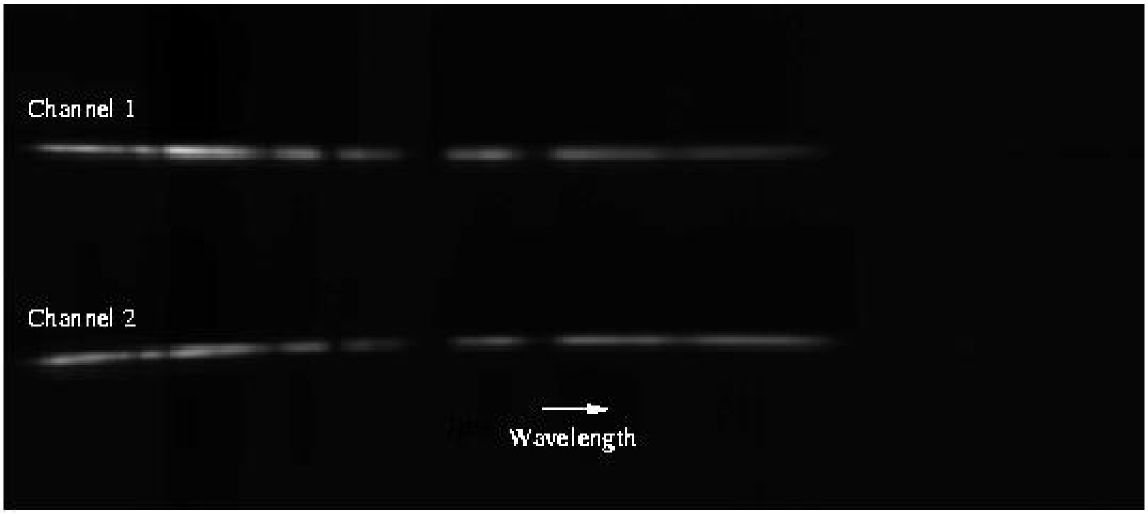

Figure 4.20: Foil spectrum taken with MIDI. *Using the light of the broad band source, the polypropylene spectrum was taken without the beam combiner. Therefore, it is visible in both channels. Compare to Figure 4.19 (Chesneau, 2001).*

time, the minor temperature shifts are not resolved and therefore not relevant.

For inserting the foils into MIDI, a small frame was designed with dimensions fitting into the filter wheel of MIDI. This frame can hold a piece of foil so that both photometric and both interferometric beams pass through it. Care had to be taken not to clamp the foil too tightly, as it stiffens and shrinks considerably at cryogenic temperatures and therefore might be damaged if internal tension is present.

The way to proceed for a calibration is, first, to identify the exact positions of specific spectral features in the reference spectra. Then, the spectra are taken with MIDI in dispersive mode, i.e., with its grism in the optical path. The same spectral features as shown in Figure 4.19 should appear. Their position on the detector can be registered. Last, one can perform a linear or even quadratic fit of the position on the detector versus the wavelength. The resulting relation should be characteristic for the grism in a given position and distance to the detector. This calibration should be done at least once per observing run.

Furthermore, it has to be made sure that the reference spectra do not show long term changes. This could potentially happen as the material deteriorates with the thermal cycles of MIDI. With laboratory tests proceeding, this point will be observed carefully. Also, homogeneity of the material might be a point to be taken into account, yet this is assumed not to be relevant with the samples used in MIDI.

Verification of Functionality First verification tests with the MIDI instruments showed that the material best suitable for the method described above is Polypropylene. It has a sufficiently high number of clear lines in the interesting wavelength region. Figure 4.20 shows its spectrum detected with MIDI.

4.5 Mutual Calibration of Laser and Piezo

In the previous sections of this chapter, several tools were presented with their properties and attributes. The now following section exposes a method how to proceed as far as the spectral calibration and the characterisation of the Internal Delay Line are concerned and demonstrates a first test of the method's capability.

4.5.1 From Spectral Wavelength to Piezo Movement

Spectral Calibration on Detector The starting point for the calibration routine is one or several of the foils presented in section 4.4. Shining broadband light into MIDI will project their spectra on the detector which will calibrate the wavelength axis on it. The spectra have to be known with sufficiently high precision. As it was shown, the precision is determined by the dispersive elements in MIDI, which might change as MIDI will be further developed.

Calibration of Laser Wavelength Taking the foil spectra as reference, the next step is to determine the CO_2 laser wavelength by shining laser light into MIDI while operated in dispersive mode. A comparison of the laser line appearing on the detector with the known spectral positions determined by the foils will immediately reveal the laser wavelength λ_{CO2}. Again, care must be taken for the stability of the laser wavelength. The measures for stabilisation described in section 4.3.1 will be verified by long term test.

Calibration of Piezo Behaviour With the laser wavelength known it is possible to test the expansion behaviour of the piezos in the Internal Delay Line in the following way. As it follows from equation (4.2), changing the applied voltage U to the piezo by ΔU induces a mechanical stroke Δs_m of

$$\Delta s_m = \epsilon_U \cdot \Delta U \quad . \tag{4.6}$$

Furthermore, a change ΔOPD of the OPD between the two interferometic arms induces the flux density in one interferometic channel to be changed in a way that can generally be described by a sinusoidal when using laser light with a very long coherence length:

$$I(\Delta OPD) = \hat{I} \cdot \sin\left(\frac{2\pi}{\lambda_{CO2}} \cdot \Delta OPD + \phi_0\right) + I_0 \quad , \tag{4.7}$$

where $\hat{I}$ is the amplitude, ϕ_0 a phase, and I_0 the offset. Identifying ΔOPD with two times the mechanical stroke from equation (4.6) yields

$$I(U) = \hat{I} \cdot \sin\left(f_U \cdot U + \phi_u\right) + I_0 \quad , \tag{4.8}$$

where f_U is a factor in units of 1/V describing the piezo behaviour at a given stroke:

$$f_U = \frac{2 \cdot 2\pi}{\lambda_{CO2}} \epsilon_U \quad . \tag{4.9}$$

Taking a measurement sequence of the flux density in a given voltage range and fitting a sinusoidal to these data outputs $\hat{I}, f_U, \phi_u$ and I_0 as fit parameters. For the average piezo response in this range it follows

$$\epsilon_U = f_U \frac{\lambda_{CO2}}{4\pi} \quad . \tag{4.10}$$

The way of retrieving one data point was as follows. Light from the CO_2 laser was injected into a Michelson setup with the two piezos and their roof mirrors. Figure 4.21 shows the experimental setup. The Pyroviewer camera (see section 4.3.1) was used as detection device. At each value of the applied voltage, three images were taken. For each image of a sequence, two

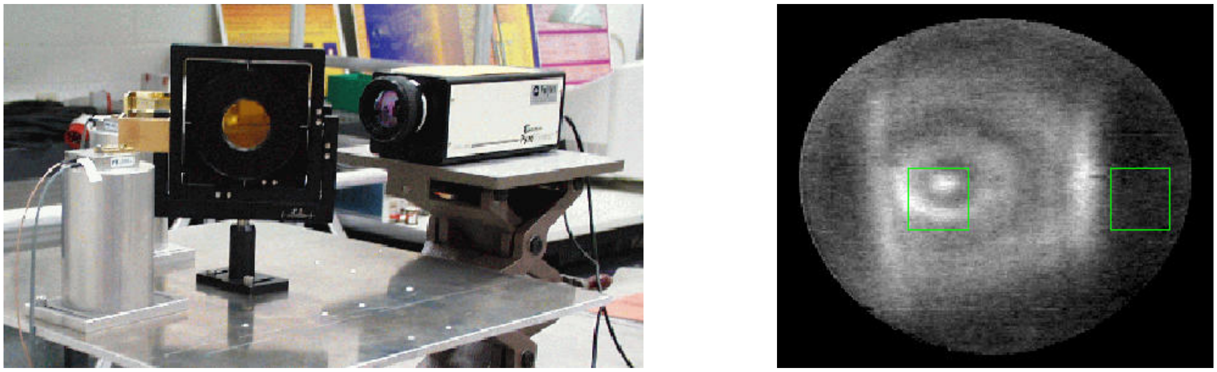

Figure 4.21: Piezo test setup with infrared interferometer and interference pattern. *Left: Experimental setup. The Pyroviewer camera, sensitive in the mid-infrared, was used as detecting device. Right: Image of the beam profile taken with the camera. The circular structure is caused by diffraction at a round aperture in the attenuator optics of the laser.*

different fields were chosen as it is shown in Figure 4.21. One field was located where no laser signal was detectable. It served as a reference to account for changes in the camera's properties. The camera was sensitive to thermal drifts, and it was unknown to what extent a varying overall light level could cause shifts of electronic offsets induced by internal controls. In the other field the laser signal was included. The data point was created as the difference of the mean pixel value in each field.

In Figure 4.22, a selection of sequences is shown taken for the piezo P66. The sinusoidal fit for the first sequence is also plotted. It is noticeable that for higher voltages this fit is out of phase in respect to the data points.

The resulting ϵ_U for both piezos can be seen in Figure 4.23. The application of a linear regression $\epsilon = m \cdot U + b$ to the piezo response yielded the fit parameters given in the table. Within the errors, these results are in good agreement with the ones found in section 4.2.

For the measurements presented here so far, it was assumed that the CO_2 laser wavelength was indeed $\lambda_{CO2} = 10.6\,\mu\text{m}$ as it was stated by the laser documentation (but see section 4.5.2). It must be noted, though, that at the time these data were taken there was no measured spectral information available. Lasers by different manufacturers may vary in the output wavelength according to fabrication details. Therefore, the resulting numbers given in the above table

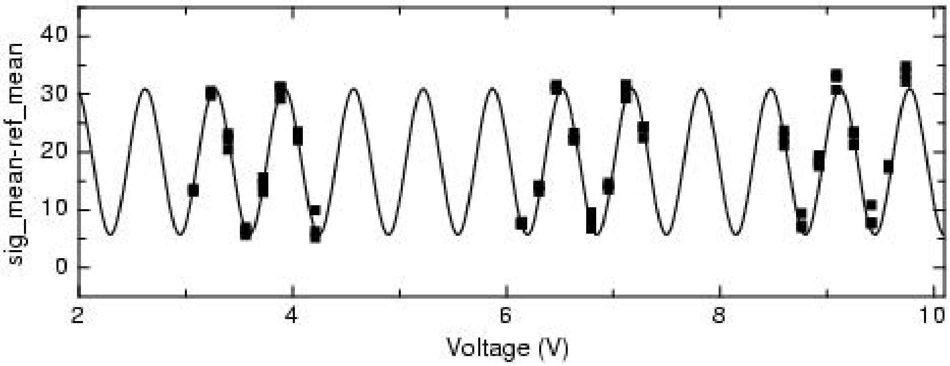

Figure 4.22: Checking the piezo response with the CO_2 laser. *Note that the sinusoidal fit for the first sequence is out of phase at higher voltages.*

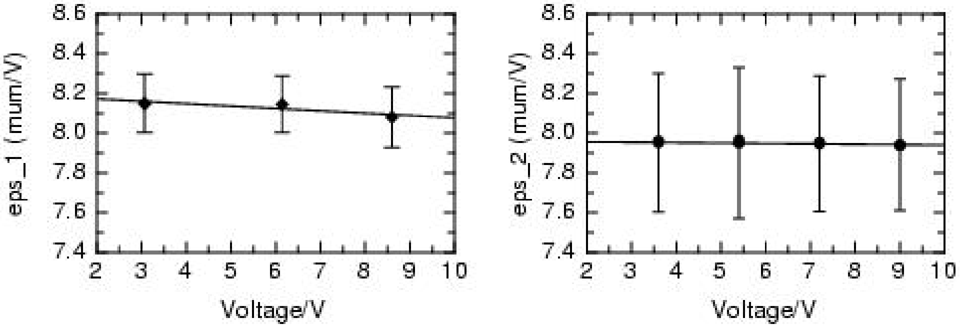

P66: ϵ_1		P67: ϵ_2	
m (µm/V^2)	b (µm/V)	m (µm/V^2)	b (µm/V)
-0.012 ± 0.038	8.20 ± 0.24	-0.002 ± 0.085	7.96 ± 0.57

Figure 4.23: Piezo response derived from given CO_2 laser wavelength. *Compare to values given in Table 4.1, section 4.2.2.*

might change as MIDI becomes fully operational and spectral information can be gained.

4.5.2 An alternative approach

Taking as a starting point the data presented in Figure 4.22, and making use of the results detailed in section 4.2, it is possible to reverse the order of calibrations. By means of equation (4.1) and the parameters of Table 4.1 one can transform the applied voltage into the mechanical deflection of the piezo stage. So here the basis is a well-known behaviour of the piezos. In Figure 4.24 this transformation is realised.

With this transformation it is now possible to gain the laser wavelength by fitting *one* sinusoidal to the data of the *whole* range, assuming they are represented by equation (4.7) where ΔOPD is two times the mechanical stroke. The fitting process yields f_s as one of the parameters, similar to f_U in equation (4.8). Thereby, one can retrieve the laser wavelength by

$$\lambda_{CO2} = \frac{4\pi}{f_s} \quad . \tag{4.11}$$

For the present data set the result of this process was $\lambda_{CO2} = (10.53 \pm 0.02)\,\mu\mathrm{m}$ which is 0.7 % shorter than the documented wavelength.

The same procedure with the laser diode operated at $T = 87\,\mathrm{K}$ and $I = 0.95\,\mathrm{A}$ yielded $\lambda_{LD} = (9.03 \pm 0.01)\,\mu\mathrm{m}$. According to the data shown in Figure 4.15 its nominal wavelength is 8.92 µm, so the wavelength obtained here is 1.2 % larger. It should be noted, though, that the Pyroviewer camera had a strong tendency to drifts and the images were very noisy, which could cause the discrepancies beyond the error given by the fit.

With the laser wavelength known by this approach, and shining laser light into MIDI, this fixes one point of the spectral axis on the detector. In order to calibrate the full spectral range of MIDI, one can use the light of a broadband source and disperse it on the detector. In this way, the light is made monochromatic in every single spectral channel, i.e., a specific pixel column. Moving one of the piezos over a certain range ΔOPD will cause interference cycles in each of these channels. Thus, the same fitting process applies correspondingly as for λ_{CO2} which pins down the wavelength detected in a given spectral channel.

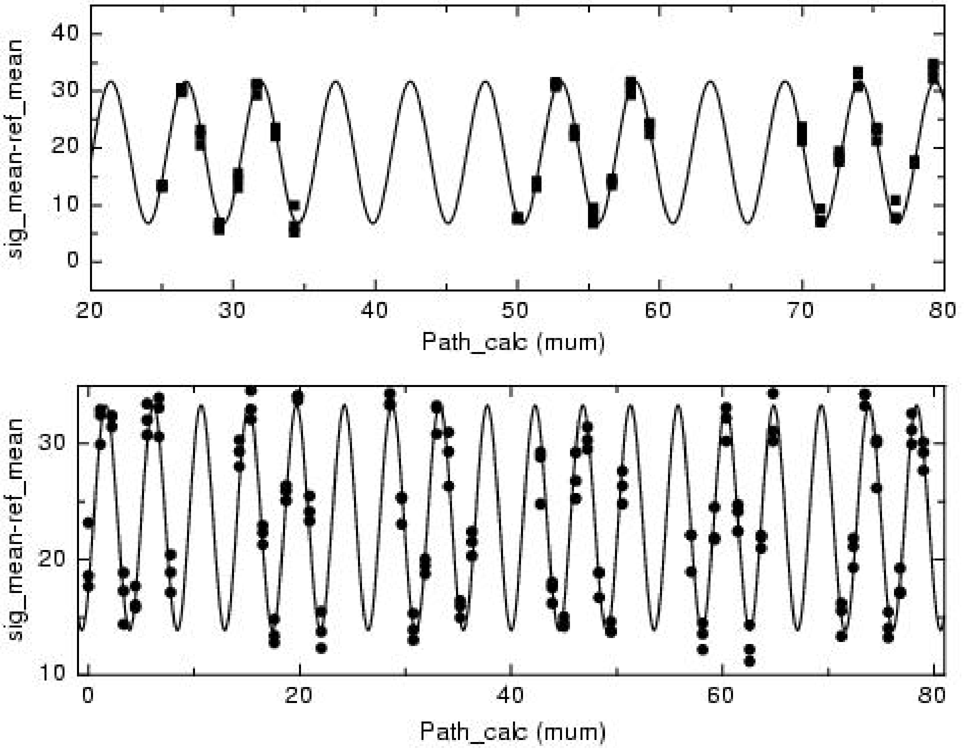

Figure 4.24: Finding the laser wavelength by defined OPD change. *The path was calculated from the applied voltage (Figure 4.22) by means of equation (4.1) and the values in Table 4.1. The sinusoidal fit was extended over all data points. Top: CO_2 laser; Bottom: Laser Diode.*

Chapter 5

Applying Stellar Interferometry

5.1 Calibrator Stars

5.1.1 Overview

As indicated earlier in section 2.3, an important issue in stellar interferometry is to have calibrator stars with well-known and stable properties. They allow for the calibration of instrumental effects and for the retrieval of useful information from measurements of science targets. The according set of calibrators has to be selected for characteristics that may vary over different wavelength regions.

In any case, care must be taken for the photometry and spectral classification, as will become clear in a moment. Let F_{SpT} be the spectral (wavelength dependent) flux density of a star as it is emitted from its surface. When considering a star as a blackbody, then not only does F_{SpT} depend on the effective temperature T_{eff} of the object as $F_{SpT} = \sigma T_{eff}^4$, where $\sigma = 5.67 \cdot 10^{-8}\,\mathrm{W\,m^{-2}\,K^{-4}}$ is the Stefan-Boltzmann constant. F_{SpT} also changes with the spectral type of the star and therefore its spectral features. If the object of radius R is at a distance r, the spectral flux density f_{SpT} measured by a terrestrial observer is

$$f_{SpT} = \frac{4\pi R^2 \cdot F_{SpT}}{4\pi r^2} = \left(\frac{\Theta}{2}\right)^2 \cdot F_{SpT} \quad , \quad [f_{SpT}] = \mathrm{W\,m^{-2}\,\mu m^{-1}}, \tag{5.1}$$

where Θ is the apparent diameter of the object. Transforming the flux into an apparent magnitude yields

$$m - m_0 = -2.5 \lg f_{SpT} = -5 \lg \Theta - 2.5 \lg F_{SpT} + const. \tag{5.2}$$

m_0 sets the zero point for the respective bandpass.

These expressions can be interpreted in a twofold way, dependent on which information about the object is assumed as given. Suppose one measures f_{SpT}, and F_{SpT} can be derived from models of stellar atmospheres. Then, following sections 2.2 and 2.3, the apparent diameter, Θ, can be estimated and therefore one can determine the visibility, V. This strategy is typically applied to calibrator stars. Furthermore, in a few cases, visibilities can be derived by direct measurements, for example, by the lunar occultation technique (Richichi and Calamai, 2001). The calibrators' visibility, known in either way, then enters directly into data reduction of the science object by giving an estimate of present instrumental effects.

On the other hand, one can start with measurements of f_{SpT} and V. Recently, more and more high angular resolution measurements have become available (see, e.g., Richichi and Percheron

(2002)) or can be made at dedicated observations (see following section). Thus, it is possible to compare stellar model predictions of an expected V with the measured value. Combined with spectral calibration (see, e.g., Cohen et al. (1999)), models can be tested and refined while parameters can be constrained leading to a better understanding of the underlying processes (Carbon, 1979; Engelke, 1992; Morossi et al., 1993). This second strategy will be chosen for science objects which are investigated.

The dependence of the flux on the wavelength also implies an additional aspect. Spectral lines might be induced by different astrophysical processes taking place in different layers of the stellar atmosphere. Therefore, if observed in different narrow bands around such lines, i.e., looking at different layers, the visibility of the star (and thus its diameter) might vary (see section 5.1.3) and should be denoted V_λ and Θ_λ to indicate dependence on the actual observation wavelength (Quirrenbach et al., 1993). Likewise, the absorption strength might vary over the wavelength region which results in different sizes of the effective stellar disc. Detailed modeling of stellar atmospheres also has to take these effects into account.

5.1.2 Establishing a Database

The database for the calibrator stars should be reasonably established prior to the actual science observations. In general, a calibrator should be a bright single star with well-understood properties and should show neither variability nor an extended atmosphere. It does not necessarily need to be unresolved by the interferometer, but its visibility should be reliably determinable. For example, Bordé et al. (2002) provide a catalogue of interferometric calibrators in the near infrared regime which was derived from photometrically calibrated objects presented by Cohen et al. (1999).

Initial Selection Criteria The general aspects mentioned above also apply for calibrators in the N band. In particular, this means that stars with dust shells are not suitable, because shells may change their structure with time and they are an indicator for stellar variability. A working group within the MIDI collaboration established the following selection criteria for searching calibrator candidates:

- declination $\leq +35°$ to be within reach of VLTI (located at geographic latitude $-19°$, accesses 60° at maximum from zenith)
- colour corrected 12 µm flux ≥ 5 Jy (N≈2.3) to be bright enough (see estimations in Chapter 3)
- colour temperature $T_{12/25}$ from 12 µm/25 µm flux ratio ≥ 4000 K (If possible, evolved stars which might have dusty circumstellar envelopes should be avoided.)

Searches in the IRAS and MSX catalogues yielded a total of 511 objects that might be called MIDI Calibrator Candidates (MCC). For all these objects, astrometric HIPPARCOS data are also available. Combining the HIPPARCOS data with stellar models yields a linear stellar diameter, which can be used for a consistency check of the angular diameter.

Photometric/Spectroscopic Information A large fraction ($\sim 75\,\%$) of MCCs were found to have photometric data between 0.35 µm and 0.58 µm from the Geneva Observatory photometric system. Of the remaining sample, about half were observed at the Belgian Mercator telescope on La Palma. Furthermore, in order to have largely consistent photometric information available, several observing runs were performed in the near-infrared (J, H, K, and L bands, 1. . . 4 µm) at the 0.75-m telescope of the South African Astronomical Observatory (SAAO) from where 456 objects were accessible. From this set, a group of 56 stars was selected to be bright in the N band and to be of possibly early stellar type. These objects should serve as primary MCCs in the early phase of MIDI on Paranal. Their spectra were specifically checked in the N band by observations with the TIMMI-2 instrument at the 3.6 m telescope of ESO on La Silla, Chile. To date, reduction of the TIMMI-2 data is ongoing. Special attention is payed to spectral lines of amorphous silicate around 9.7 µm (mainly in emission) as well as (absorption) signatures around 11.3 µm originating from crystalline silicates (Boekel, 2002). They could indicate the presence of dust shells, which should be avoided for MIDI calibrators.

Modeling (Verhoelst, 2002) This photometric information is used to model the stellar Spectral Energy Distribution (SED) for each MCC, using Kurucz models[1] (Kurucz, 1979; Morossi et al., 1993) with T_{eff} and the angular diameter as free parameters. The Geneva photometry offers a good coverage of that part of the SED which is very sensitive to temperature, allowing for a rather accurate estimate of T_{eff}. The JHKL measurements probe a the wavelength region which is only mildly temperature-sensitive and thus provides an accurate estimate of the angular diameter, given the already good estimation of T_{eff}. The resulting angular diameter seems to agree with interferometric measurements to within 5% for stars hotter than roughly 4000 K.

5.1.3 Interferometric Verification

Models constrained by photometric information alone can be checked against interferometric observations. Not only do models predict visibilities for MIDI in the N band, but also in other photometric bands, e.g., the K band (2.2 µm) in which most current stellar interferometers operate. Visibility measurements taken in the K band therefore help verify model predictions and thus check the model reliability.

Broad K Band Measurements

In the course of this work, a first set of MCCs could be measured interferometrically in the K band during observing runs undertaken at the IOTA observatory on Mount Hopkins near Tucson, Arizona, USA (Traub et al., 2000). Both the classical optical beam combining setup and the FLUOR instrument were used, each with a broadband K′ filter (2.0. . . 2.3 µm). The main steps of the FLUOR data reduction process are described in Appendix B. Figure 5.1 shows two exemplary results taken with FLUOR at a 38-m baseline. Table 5.1 lists the full set of visibilities achieved through end of 2001.

Due to adverse technical circumstances (system failure, alignment problems) the overall quantity of useful data was unexpectedly small. To date, with the VLTI going online and with VINCI being an effective tool, a snapshot survey to observe as many MCCs interferometrically as possible in a broad K band is planned, in order to verify their suitability as calibrators.

---

[1] In the future, also models more appropriate for cooler stars may be applied.

Table 5.1: Visibilities measured in K′ on MIDI Calibrator Candidates. *A broadband K′ filter (2.0…2.3 µm) was used. Except for HD 116658, which was measured with a 30-m baseline, all other objects were observed with a baseline of 38 m.*

Star	Date (dd/mm/yyyy)	Azimuth (degrees)	Spatial frq. (cycles/arcsec)[a]	Visibility	Error
HD 62509	08/04/2000	89.75	86.04	0.55982	0.01670
(β Gem)		90.68	86.04	0.55281	0.01646
		91.53	86.05	0.55624	0.01654
HD 80493	07/04/2000	84.59	86.86	0.58310	0.00575
(α Lyn)		85.43	86.85	0.58898	0.00552
		87.19	86.85	0.59565	0.00579
HD 120933	07/04/2000	66.86	86.47	0.74505	0.00839
(AW CVn)		78.04	86.88	0.73287	0.01037
		79.52	86.88	0.72877	0.01015
		85.02	86.86	0.74148	0.00870
		85.76	86.85	0.74377	0.00787
	08/04/2000	73.14	86.82	0.74404	0.00524
		74.63	86.85	0.74142	0.00499
HD 116658	10/04/2000	60.68	70.79	0.98944	0.00849
(α Vir)		62.10	69.42	1.00030	0.00935
		63.93	67.87	0.99459	0.00915
		67.52	65.32	0.97581	0.00979
		69.43	64.21	0.97663	0.00927

[a] 1 cycle/arcsec=206 265 cycles/rad

Object information taken from the SIMBAD database (see bibliography) and the HIPPARCOS catalogue:

Object	HD number	Spectral Type	Brightness V (mag)	K (mag)	$F_{12\mu m}$ (Jy)	Parallax (mas)	Remarks
β Gem	HD 62509	K0IIIb	1.15	-1.11	124.6	96.7	Variable
α Lyn	HD 80493	K7III	3.16	-0.65	86.9	14.7	Variable
AW CVn	HD 120933	K5III	4.76	0.14	49.0	5.4	Variable
α Vir	HD 116658	B1III-IV	1.04	1.65	–	12.4	Ellipsoidal variable

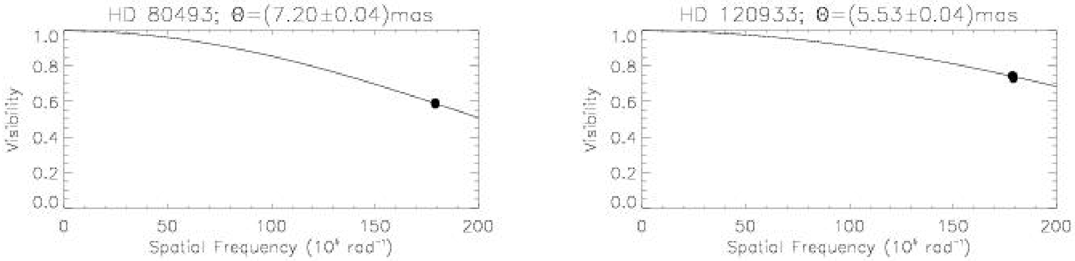

Figure 5.1: K′ filter measurements on MIDI Calibrator Candidates. *The data were taken with the FLUOR instrument at IOTA in a broadband K′ (2.0…2.3 µm) filter and with the 38-m baseline. For the fit (solid lines), a uniform disk was assumed. The resulting diameters Θ are indicated.*

Narrow K Band Measurements

Nevertheless, as it was described in section 5.1.1, the visibility V may vary if measured in different narrow band filters. In order to investigate in detail this wavelength dependency of V and the accuracy of the applied stellar models, a small group of objects was selected from the MCCs for observations at IOTA in spring 2002. Observations took advantage of the set of narrow band filters available with the FLUOR instrument (see Table 5.2). In order to compare the findings at MCCs with other late-type stars, some common M-giants were also observed as well as Mira type stars.

Table 5.3 summarises the basic properties of the observed objects. Preliminary results of the data reduction are listed in Table 5.4 and plotted in Figure 5.2. For ϵ Peg, the results are not conclusive yet as this object was resolved only marginally with the baselines used. A tendency can be seen that for an object the differences between measured diameters in different narrow filters increase as the object becomes of later type. This may be due to a decrease in the stellar temperature which leads to molecule formation in the stellar atmosphere.

A more thorough evaluation of the 2002 narrow band data and the comparison with stellar atmosphere models are still ongoing. If the narrow K band visibilities can be well reproduced by detailed modeling, then confidence would be increased that the applied models also allow good predictions of the object properties in the N band.

Table 5.2: K band filters available with the FLUOR instrument.

Filter	Wavelength Pass (µm)	Remarks
K′	2.15 ± 0.15	broad band
K203	2.03 ± 0.05	H_2O absorption bands
K215	2.15 ± 0.05	continuum
K222	2.22 ± 0.05	continuum
K239	2.39 ± 0.05	CO and H_2O absorption bands

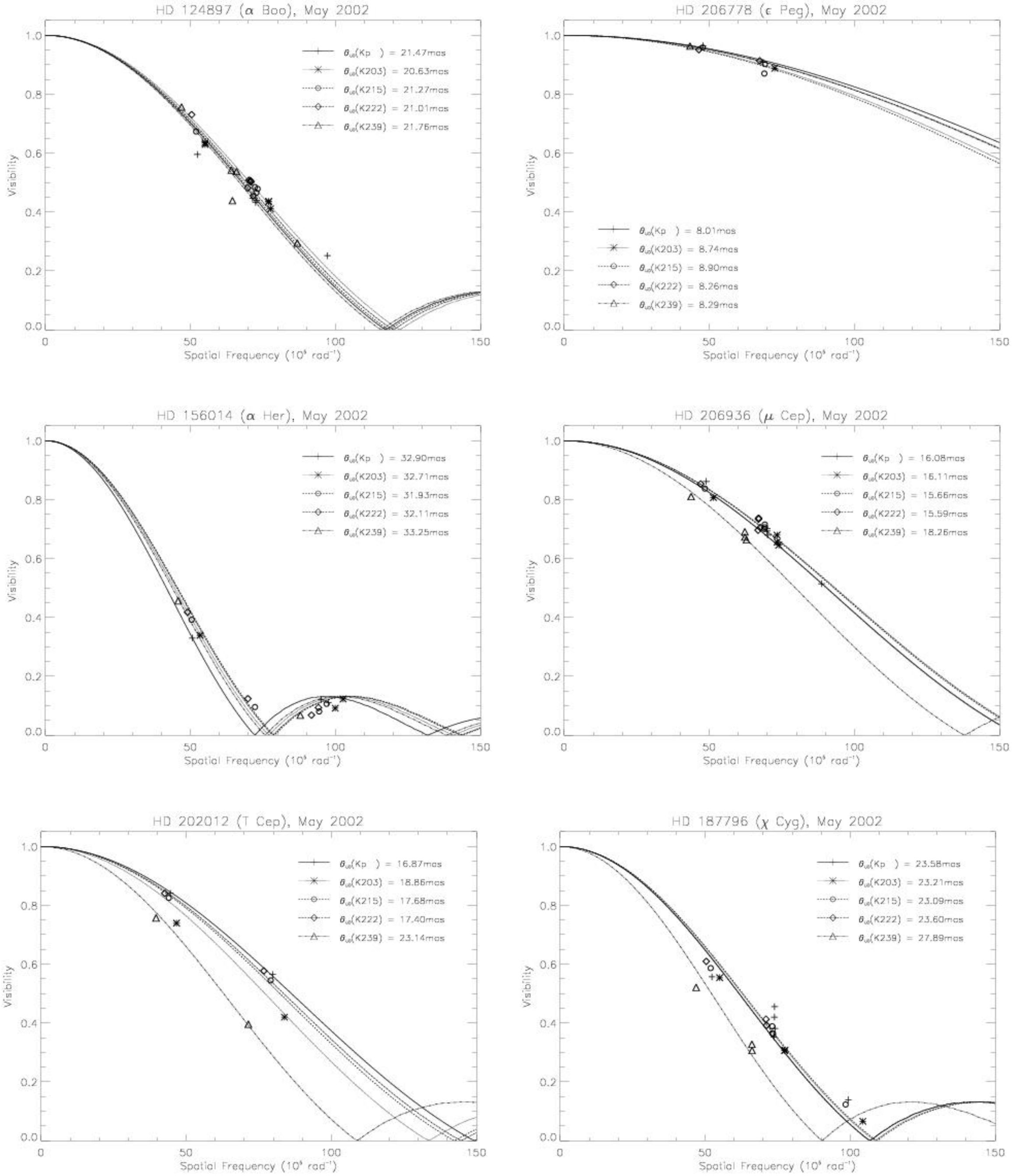

Figure 5.2: Measurements in narrow K filters on MIDI Calibrator Candidates. *The data were taken with the FLUOR instrument at IOTA in the filters given in Table 5.2 at several baselines (see Table 5.4). For the fits, uniform disks were assumed. The resulting diameters θ are indicated.*

Table 5.3: Objects observed in spring 2002 with narrow K band filters. *Object information is taken from the SIMBAD database (see bibliography) and the HIPPARCOS catalogue.*

Object	HD number	Spectral Type	Brightness V (mag)	K (mag)	$F_{12\mu m}$ (Jy)	Remarks
α Boo	HD 124897	K1.5III	-0.04	-2.95	793.1	Variable; MCC
ϵ Peg	HD 206778	K2Ib	2.40	-0.85	103.9	Variable; MCC
α Her	HD 156014	M5Ib-II	3.48	–	1515.0	Semi-regular pulsating
μ Cep	HD 206936	M2Iae	4.04	-1.65	1296.0	Semi-regular pulsating
T Cep	HD 202012	M7IIIe	7.37	-1.56	752.9	Mira Cet type
χ Cyg	HD 187796	S	6.80	-1.84	1688.0	Mira Cet type

Object	HD number	Parallax (mas)
α Boo	HD 124897	88.9
ϵ Peg	HD 206778	4.9
α Her	HD 156014	8.5
μ Cep	HD 206936	0.6
T Cep	HD 202012	4.8
χ Cyg	HD 187796	9.4

Table 5.4: Visibilities in narrow K filters measured on MIDI Calibrator Candidates. *Note: 1 cycle/arcsec=206 265 cycles/rad*

Star	Filter	Date (dd/mm/yyyy)	Azimuth (degrees)	Spatial frq. (cycles/arcsec)	Visibility	Error
HD 124897	K′	31/05/2002	82.79	47.14	0.25140	0.00557
(α Boo)		02/06/2002	120.05	35.15	0.43232	0.00451
		02/06/2002	121.12	35.28	0.43977	0.00455
		03/06/2002	115.62	34.61	0.44654	0.00370
		05/06/2002	121.95	25.39	0.59532	0.00454
	K203	04/06/2002	122.93	37.27	0.43417	0.00587
		04/06/2002	123.35	37.32	0.43612	0.00573
		05/06/2002	122.37	26.68	0.63482	0.00922
		05/06/2002	122.63	26.69	0.62936	0.00794
		06/06/2002	131.03	37.62	0.41085	0.00584
	K215	02/06/2002	121.57	35.01	0.48446	0.00537
		03/06/2002	119.31	34.74	0.45398	0.00308
		04/06/2002	123.75	35.25	0.46551	0.00591
		05/06/2002	122.97	25.18	0.67328	0.00527
		06/06/2002	131.41	35.46	0.47833	0.00564
	K222	02/06/2002	122.02	34.02	0.50804	0.00541
		03/06/2002	119.93	33.78	0.48177	0.00426
		04/06/2002	124.28	34.25	0.50675	0.00562
		04/06/2002	124.74	34.30	0.50349	0.00556
		05/06/2002	123.38	24.44	0.73048	0.00739
		06/06/2002	131.70	34.36	0.50220	0.00577

Table 5.4: (continued)

Star	Filter	Date (dd/mm/yyyy)	Azimuth (degrees)	Spatial frq. (cycles/arcsec)	Visibility	Error
	K239	31/05/2002	93.42	42.09	0.29445	0.00917
		02/06/2002	116.61	31.08	0.54194	0.00766
		03/06/2002	118.21	31.26	0.43841	0.01334
		05/06/2002	124.06	22.74	0.75617	0.00655
		06/06/2002	132.04	31.94	0.53722	0.00773
HD 206778 (ϵ Peg)	K′	05/06/2002	107.48	23.18	0.96468	0.00643
		06/06/2002	118.83	33.22	0.90835	0.00903
	K203	06/06/2002	120.04	35.17	0.88781	0.01211
	K215	05/06/2002	109.14	23.13	0.95844	0.00616
		06/06/2002	121.15	33.43	0.87006	0.01115
		06/06/2002	121.63	33.54	0.90227	0.01042
	K222	05/06/2002	109.67	22.49	0.95084	0.00584
		06/06/2002	122.12	32.65	0.91378	0.01067
	K239	05/06/2002	110.43	21.01	0.96296	0.01080
HD 156014 (α Her)	K′	31/05/2002	95.74	46.07	0.12166	0.00575
		05/06/2002	114.51	24.54	0.32985	0.00288
		07/06/2002	109.64	47.31	0.11091	0.00451
	K203	31/05/2002	96.78	48.44	0.09165	0.00546
		05/06/2002	115.17	25.85	0.33897	0.00266
		07/06/2002	110.13	49.76	0.12288	0.00366
	K215	31/05/2002	97.54	45.75	0.08062	0.00248
		05/06/2002	115.60	24.43	0.39192	0.00153
		06/06/2002	125.40	35.02	0.09539	0.00157
		07/06/2002	110.55	47.00	0.10630	0.00282
	K222	31/05/2002	98.95	44.47	0.06782	0.00663
		05/06/2002	116.08	23.75	0.41749	0.00156
		06/06/2002	124.57	33.85	0.12410	0.00201
		07/06/2002	110.92	45.64	0.09381	0.00267
	K239	05/06/2002	116.89	22.17	0.45651	0.00296
		07/06/2002	111.95	42.60	0.06782	0.00516
HD 206936 (μ Cep)	K′	31/05/2002	88.71	42.98	0.51430	0.00632
		02/06/2002	111.00	33.99	0.67963	0.00780
		03/06/2002	112.67	33.89	0.69311	0.01111
		05/06/2002	96.40	23.73	0.86157	0.00598
		06/06/2002	112.28	33.92	0.70193	0.00712
	K203	03/06/2002	113.41	35.55	0.67949	0.01155
		04/06/2002	108.11	35.85	0.64529	0.00690
		05/06/2002	97.70	24.91	0.80678	0.00837
		06/06/2002	113.35	35.56	0.65521	0.00824
	K215	02/06/2002	115.19	33.43	0.70043	0.00371
		03/06/2002	113.94	33.51	0.70576	0.00871
		05/06/2002	98.30	23.49	0.83726	0.00520
		06/06/2002	114.19	33.50	0.71526	0.00776
	K222	02/06/2002	116.05	32.38	0.69584	0.00446
		03/06/2002	114.85	32.46	0.73396	0.00484
		04/06/2002	109.84	32.74	0.70520	0.00461
		05/06/2002	98.91	22.78	0.85323	0.00551

Table 5.4: (continued)

Star	Filter	Date (dd/mm/yyyy)	Azimuth (degrees)	Spatial frq. (cycles/arcsec)	Visibility	Error
		06/06/2002	114.78	32.46	0.73689	0.00767
	K239	03/06/2002	115.58	30.17	0.69065	0.01600
		04/06/2002	110.80	30.43	0.66325	0.00641
		05/06/2002	99.67	21.19	0.81025	0.01413
		06/06/2002	115.54	30.17	0.67268	0.01048
HD 202012	K′	05/06/2002	108.67	21.57	0.84095	0.00577
(T Cep)		07/06/2002	89.79	38.69	0.56471	0.01080
	K203	05/06/2002	109.67	22.61	0.73932	0.00805
		07/06/2002	90.94	40.64	0.41964	0.00977
	K215	05/06/2002	110.29	21.31	0.82547	0.00497
		07/06/2002	91.66	38.34	0.54470	0.00955
	K222	05/06/2002	110.90	20.65	0.84083	0.00488
		07/06/2002	92.12	37.20	0.57732	0.00961
	K239	05/06/2002	111.87	19.18	0.75710	0.01123
		07/06/2002	92.91	34.61	0.39573	0.01023
HD 187796	K′	30/05/2002	86.61	48.17	0.13928	0.00395
(χ Cyg)		01/06/2002	123.05	35.84	0.45530	0.00736
		01/06/2002	123.98	35.81	0.42012	0.00809
		02/06/2002	117.90	35.90	0.38092	0.00499
		04/06/2002	109.63	35.73	0.35256	0.00326
		05/06/2002	101.38	25.36	0.55687	0.00395
	K203	30/05/2002	95.72	50.59	0.06557	0.00229
		04/06/2002	110.45	37.55	0.30773	0.00374
		05/06/2002	102.13	26.65	0.55381	0.00415
		06/06/2002	109.38	37.52	0.30610	0.00392
	K215	30/05/2002	99.71	47.71	0.12288	0.00163
		02/06/2002	120.95	35.57	0.36346	0.00220
		04/06/2002	111.43	35.46	0.36524	0.00164
		05/06/2002	102.70	25.15	0.58652	0.00256
		06/06/2002	110.67	35.44	0.38872	0.00399
	K222	02/06/2002	121.79	34.50	0.39179	0.00306
		05/06/2002	103.25	24.40	0.60943	0.00279
		06/06/2002	111.26	34.40	0.41304	0.00424
	K239	04/06/2002	113.22	32.06	0.30659	0.00587
		05/06/2002	104.24	22.72	0.52096	0.00480
		06/06/2002	112.04	32.04	0.32787	0.00442

5.2 Interferometric Data and Astrophysical Modeling

This section is dedicated to a demonstration of how interferometric data can be used to improve the understanding of astrophysical objects.

The supergiant α Ori, the Mira star R Leo, and the semi-regular variable SW Vir are considered. Their basic information are listed in Table 5.5. For all three objects, interferometric data are available in the K band (2.2 µm) from the FLUOR interferometer and in the L band (3.6 µm) from the TISIS instrument (Mennesson et al., 1999). Furthermore, Danchi et al. (1994, hereafter D94) proposed some silicate dust shell models for α Ori and R Leo based on interferometric data taken at 11 µm with the Infrared Spatial Interferometer (ISI) on Mount Wilson, California, USA (Hale et al., 2000). In the following, these models are altered slightly and evaluated in the K and L bands in order to learn if these pure dust models can reproduce the data available in these bands. Since SW Vir is of an intermediate type in between α Ori and R Leo, it is also included in this study. This will also allow the derivation of some expected observational N band results for this object which is presently among the first targets to be observed by MIDI (MIDI Science Group, 2001).

5.2.1 The Modeling Code

The radiative transfer code utilised was developed and is described by Lopez et al. (1995) and Lopez et al. (1997) (see Niccolini et al. (2002) for an update report). The star is assumed to be a blackbody. It emits photons which can either pass the envelope directly, or they are scattered in the envelope, or the photons are absorbed and then re-emitted by the dust grains. Spherical symmetry is assumed for the envelope. A grid over the dust shell has to be defined with radial zones and angular sections, with the resolution accounting for expected temperature gradients. The code calculates an equilibrium temperature profile for the studied object, with the stellar radius left as scaling factor. From this profile, the spatial flux distribution at a given wavelength can be derived, i.e., a model image of the object at this wavelength can be created. For the purpose of producing the image, the code allows to choose a zooming factor while the image dimensions are always fixed at 300×300 pixels.

In order to obtain model visibilities, a Fourier transform can be applied to the image (see section 2.2.1). The resulting two-dimensional Fourier map is then plotted along a cut through the origin parallel to one of the spatial frequency axes[2].

In this study, the dust particle material was constrained to astronomical silicates as characterised by Draine and Lee (1984) and also used by D94. Optical properties were considered at 32 wavelengths between 0.1 µm and 300 µm. The number density distribution $s(a)$ of spherical particles having the radius a is given by $s(a) \sim a^{-3.5}$ where a is contained in the limits $0.005\,\mu\mathrm{m} \ldots 0.25\,\mu\mathrm{m}$ (Lopez et al., 1997).

The parameters of the model are the stellar radius R_* and its effective temperature T_* which together define the total flux radiated by the star (see equation (5.1)). Furthermore, the dust envelope is described by its inner and outer radius, r_i and r_o, in units of R_* and its optical depth, τ_λ, which can be defined at a given wavelength, λ, expressed in µm. In the present case, it was always set $\lambda = 11$ µm in accordance with D94.

The grain density distribution $n(r)$ was chosen to take into account acceleration phenomena

---

[2] Since the objects under study are spherically symmetric, any cut through the origin will show the same shape.

Table 5.5: Basic data of modeled objects. *Values are taken from the SIMBAD database.*

Object	Spectral Type	Brightness V (mag)	K (mag)	L (mag)	$F_{12\mu m}$ (Jy)	Variability	Period (days)
α Ori	M1	0.58	-4.01	-4.43	4682.00	Semi-regular	2070
R Leo	M8IIIe	6.02	-2.63	-3.19	2161.00	Mira	313
SW Vir	M7III	7.05	-1.74	–	681.00	Semi-regular	150

induced by gas outflowing from the star, similar to the models of D94. Therefore, the distribution $n(r)$ was described by

$$n(r) = n_i \cdot \frac{r_i^2}{r^2} \cdot \frac{1}{(1 - A \cdot r_i/r)^{1/2}} \quad , \tag{5.3}$$

where n_i is the density at the inner edge of the dust shell. The parameter A is defined as

$$A \equiv 1 - (v_i/v_{\inf})^2 \quad , \tag{5.4}$$

where v_i is the velocity of the outflowing gas at the inner edge of the envelope and $v_{\inf}$ the terminal velocity. A typical value is $A \approx 0.99$ (see D94), which was used for this study. This means that the density $n(r)$ is peaked at the inner edge when compared to a usual r^{-2} law.

5.2.2 Observational Data

The model output Spectral Energy Distribution (SED) was compared to existing low spectral resolution data from different catalogues available at the SIMBAD database. For α Ori and R Leo, D94 determined additional flux measurements between 9 µm and 22 µm.

The interferometric data for α Ori, R Leo, and SW Vir in the K band are taken from Perrin et al. (2002a, in preparation), Perrin et al. (1999), and Perrin et al. (2002b). Chagnon et al. (2002) provide visibility measurements for these objects in the L band. For α Ori and R Leo, the visibilities at 11 µm were extracted from D94.

5.2.3 Comparison between Model and Observations

The supergiant α Ori

D94 proposed that a spherical silicate dust shell existed around α Ori. This shell was thought to be very thin and quite far away from the star (see Table 5.6). The effective stellar temperature of

Table 5.6: Parameters used for modeling. T_*: *stellar temperature;* R_*: *stellar radius;* r_i, r_o: *inner resp. outer radius of dust shell;* τ_{11}: *optical depth of shell at 11 µm. In all cases, an accelerated dust density profile was used (see section 5.2.1).*

Object	T_* (K)	R_* (mas)	r_i/R_*	r_o/R_*	τ_{11}
α Ori	3640	21.8	45.9	48.2	0.0065
R Leo	2500	14.9	3.5	140.0	0.1
SW Vir	3100	8.4	30.0	50.0	0.01

3640 K is consistent with the temperature 3520 K by Perrin et al. (2002a, in preparation). Using these parameters, the model output is shown in Figure 5.3. The model is in good agreement with the SED and the interferometric data in K, L, and N. The visibility curves in K and L are almost identical which indicates that the same physical structures are seen. They do not show the dust feature seen in the N band at spatial frequencies below $3 \cdot 10^5\,\mathrm{rad}^{-1}$ which indicates that the dust shell is transparent and cannot be seen in the K and L band.

The Mira star R Leo

As a Mira star, R Leo shows large photometric variations due to pulsation, as is indicated by the scatter in the photometric data at wavelengths below 1.0 µm shown in Figure 5.4. For the present study, it was regarded as sufficient if the model output came near to some of the photometric data. Furthermore, it is assumed that the structure of the envelope is not changed by the pulsation.

Applying the parameters of D94 for a pure silicate shell yielded the model output shown in Figure 5.4. They chose a temperature based on photometric data above 8 µm where emission from cool dust has an important contribution to the total flux. Here, photometric data at smaller wavelengths also have been considered to determine the stellar temperature, which was adopted as $T_* = 2500\,\mathrm{K}$. Therefore, with a higher temperature and the total flux given, the stellar radius should be accordingly smaller (see equation (5.1)). This is consistent with the fact that the uniform disc radius in the K band is roughly 15 mas (Perrin et al., 1999). Since it is assumed, in general, that measurements in the K band are mostly sensitive to regions close to the stellar photosphere, this value was taken as R_*.

Differing from D94, who chose $r_i = 2R_*$, a larger $r_i = 3.5R_*$ was assumed for the dust shell to account for the higher T_* and to keep the temperature of the grains close to the estimated temperature of grain condensation. Choosing $r_i = 140R_*$, and almost maintaining the optical depth τ_{11}, yielded the model output shown in Figure 5.5. It is apparent that both the K band and the N band data can be satisfactorily explained. At the same time, the L band data are over-estimated, i.e., they suggest a larger structure. Choosing a larger stellar radius could make the model comply with the L and N band data, since the latter are less sensitive to parameter changes as they are at low spatial frequencies. Yet, then the K band data are under-estimated.

The semi-regular variable star SW Vir

For a M7III star like SW Vir, Perrin et al. (1998) suggested an effective temperature of roughly 3100 K, so this value was adopted for T_*. Likewise, the K band uniform disc radius of about 17 mas was assumed for R_*. Searching for a set of shell parameters r_i, r_o, and τ_λ which would fit the observational data in the K band yielded the values given in Table 5.6. The resulting plots are shown in Figure 5.6. Like in the case of R Leo, the L band data are over-estimated and suggest a larger stellar radius.

5.2.4 Discussion

The study presented here was limited in several respects, and a few aspects need further investigation. As was mentioned, only one material was used. The influence of other dust materials, e.g., graphites or even mixtures of different materials, should be regarded. For example, for R Leo, D94 achieved the best agreement between model and data with a mixture of silicates and

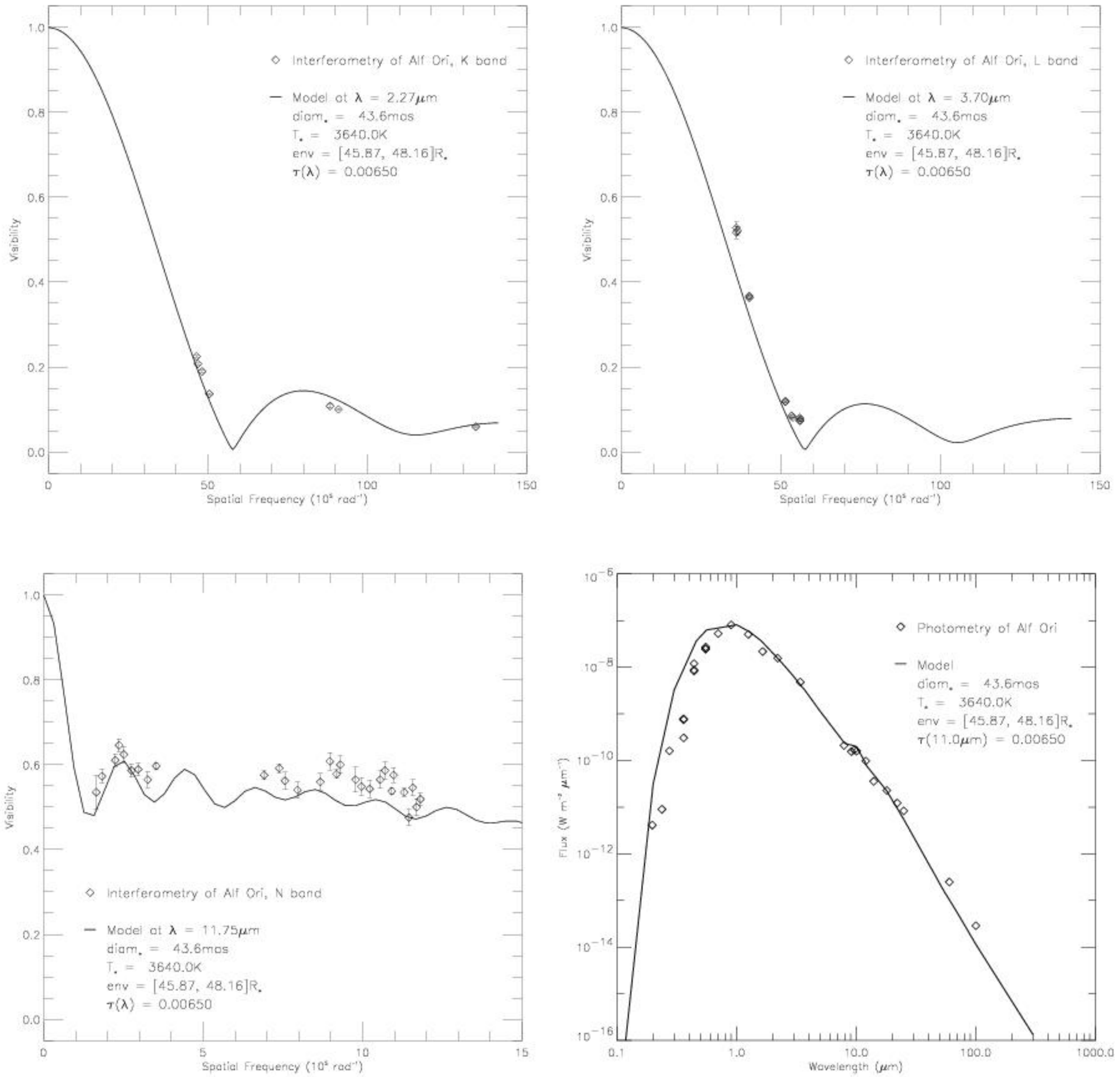

Figure 5.3: Model output for α Ori. *From top left to bottom left: modeled visibility curve with interferometric data for the bands K, L, and N; bottom right: modeled spectral energy distribution with photometric data.*

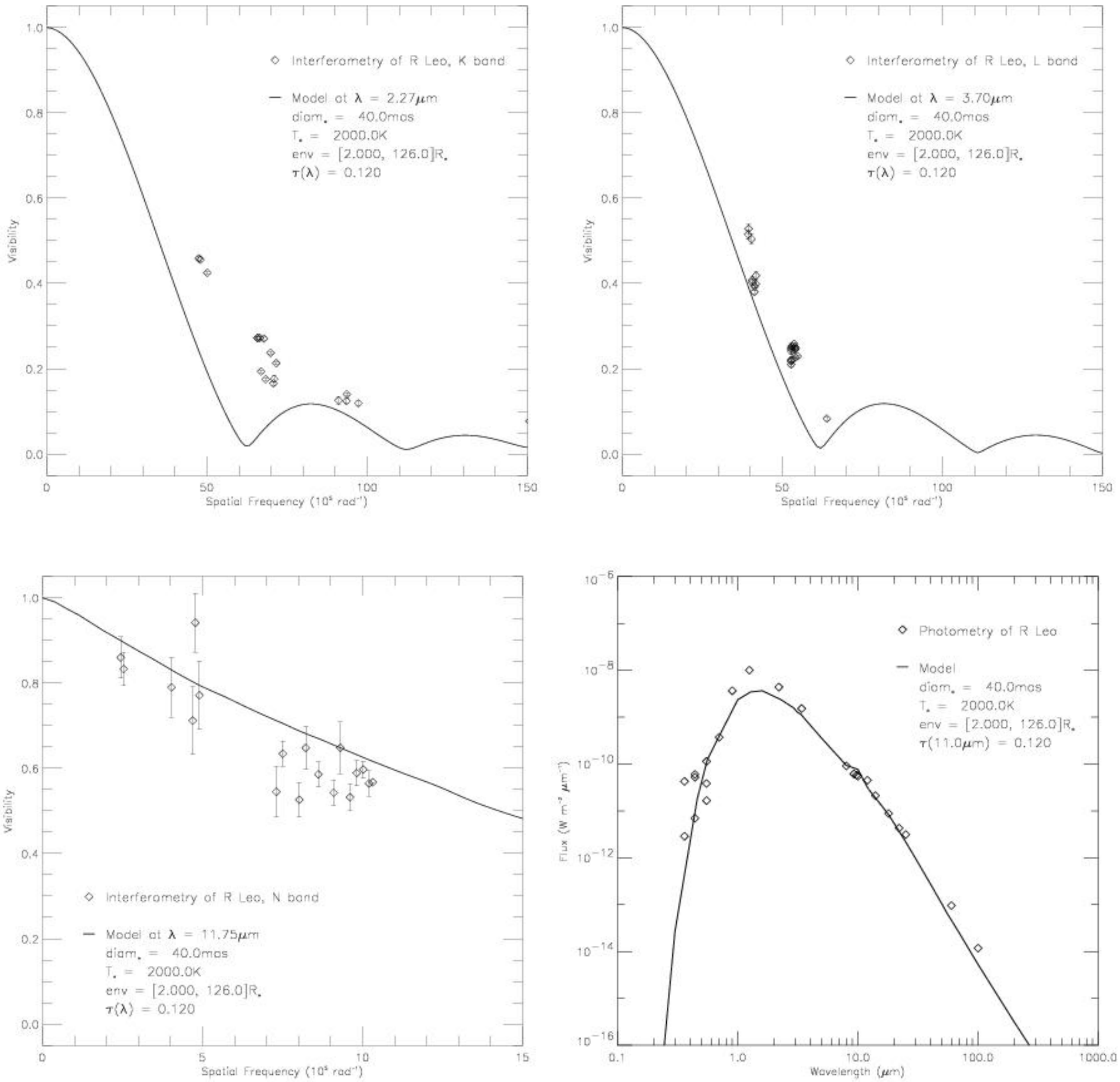

Figure 5.4: Model output for R Leo, initial parameters. *From top left to bottom left: modeled visibility curve with interferometric data for the bands K, L, and N; bottom right: modeled spectral energy distribution with photometric data.*

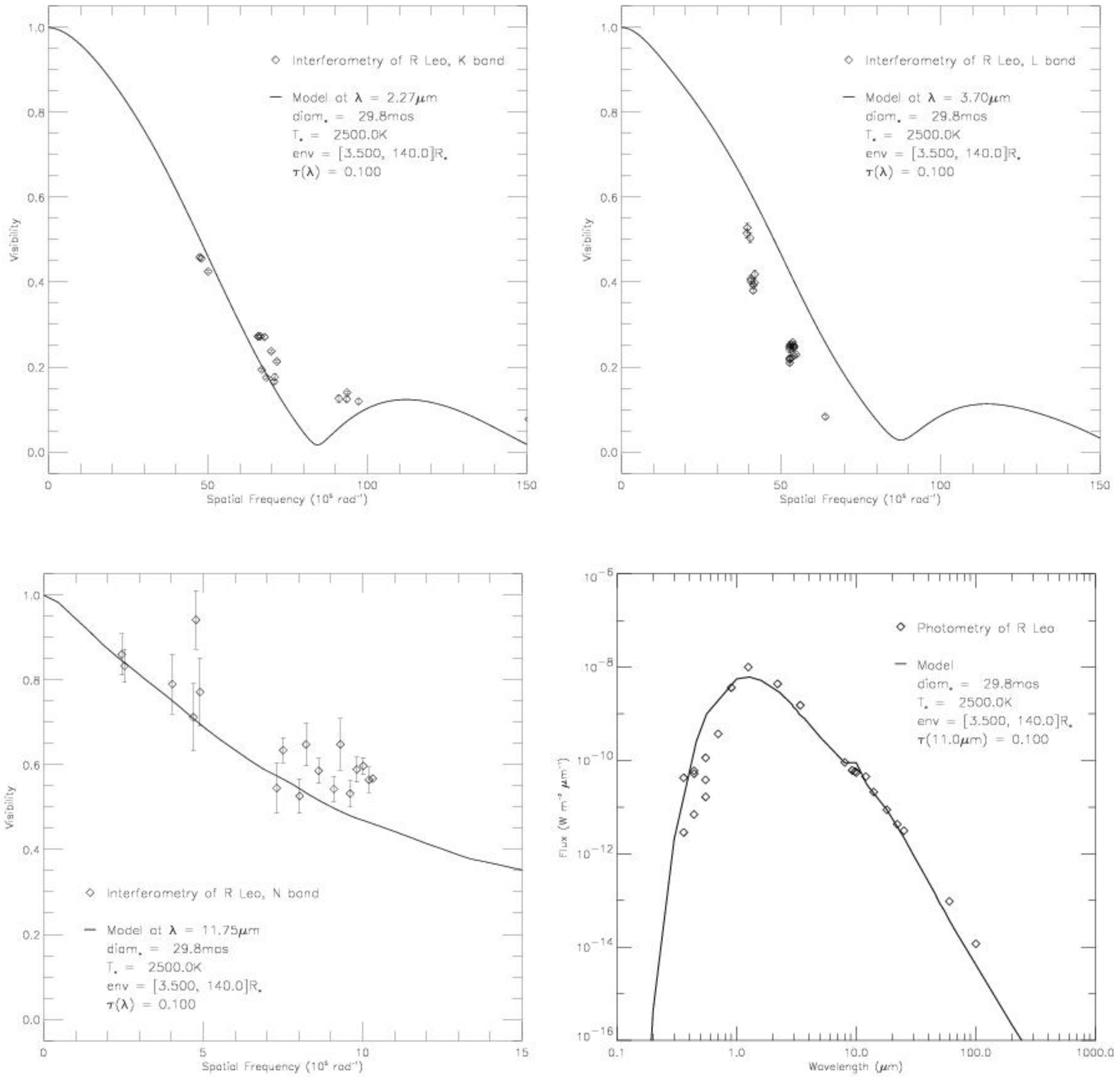

Figure 5.5: Model output for R Leo, modified parameters. *From top left to bottom left: modeled visibility curve with interferometric data for the bands K, L, and N; bottom right: modeled spectral energy distribution with photometric data.*

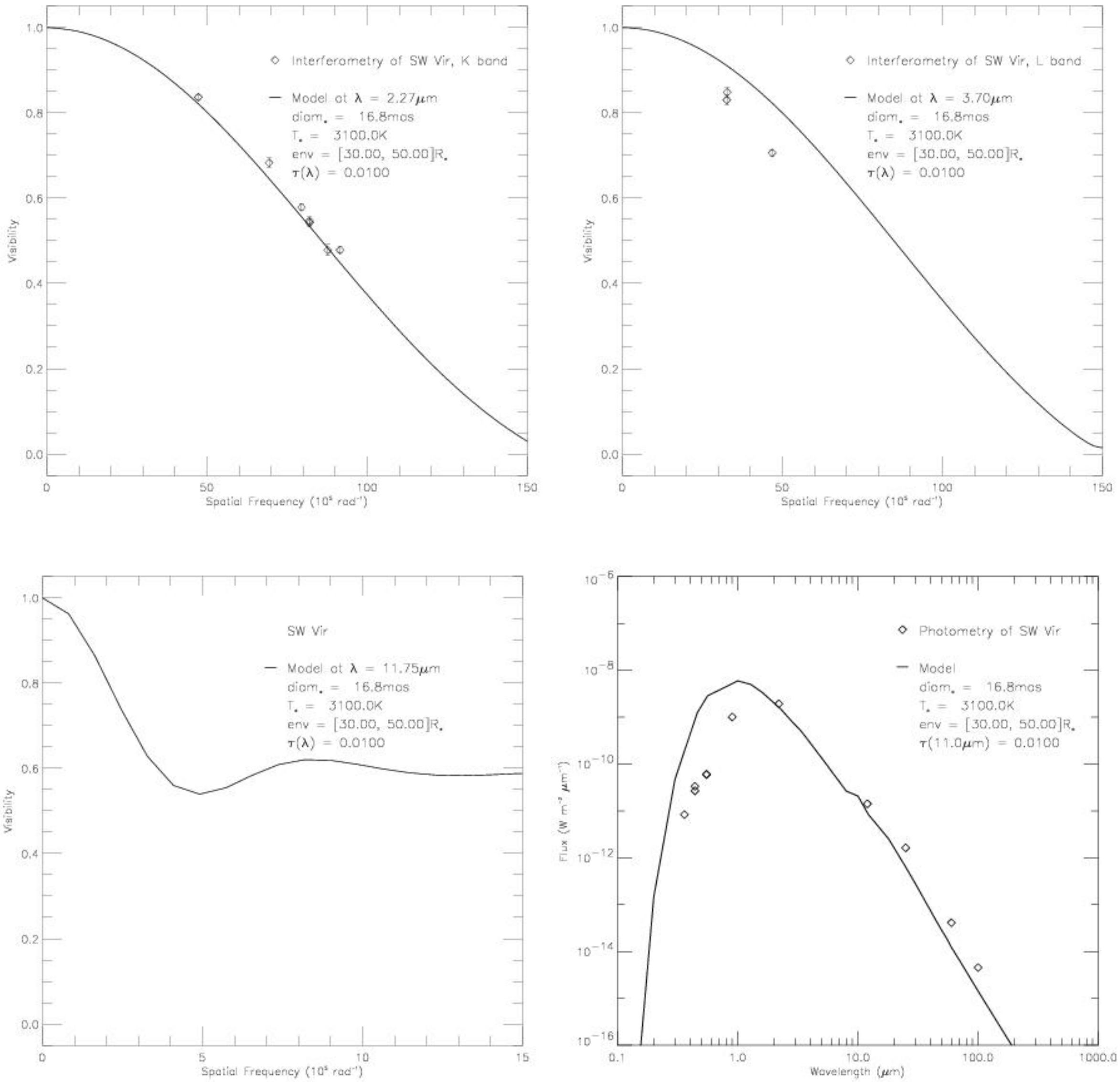

Figure 5.6: Model output for SW Vir. *Top left and right: modeled visibility curve with interferometric data for the K and L bands; bottom left: expected visibility curve for the N band; bottom right: modeled spectral energy distribution with photometric data.*

graphites. A further issue is the model parameter, A, described in equation (5.4) and chosen the same for all three objects. In D94, it was not stated explicitly which values were used. An individual analysis of outflowing matter for each object would be useful.

A more technical problem of using the model code arises by the fixed size of the image output. In order to achieve a spatial resolution of the code which is high enough to compare to existing data, an appropriate zooming factor had to be chosen. Yet, by zooming into the object and having the image size fixed, exterior parts of the surrounding structure may lie outside the image boundaries. This, in turn, means that flux is increasingly lost at low spatial frequencies. In the case of α Ori, where dust emission is localised in a very thin layer and is very important in the mid-infrared, this effect can have a strong and falsifying impact, even though in the present study this was not an issue. Yet, for R Leo a zoom factor had to be chosen in the K and L bands which led to parts of the envelope ending up outside the image. The resulting effect needs to be evaluated. It is expected that for these wavelengths this effect should be less relevant since the outer parts of the envelope contribute only a small fraction to the flux.

Keeping these limitations in mind, one can draw the following conclusions. Out of the three studied cases, the best consistency between observational photometric data, interferometric data in different bands, and a dust shell model is achieved in the case of α Ori. The oscillations of observed visibilities could qualitatively be well reproduced. The dust shell in this case is optically very thin and at a great distance from the star. It seems to have little impact on near-infrared observations and could indicate an episodic mass loss process.

In the case of R Leo, the photometric and K and N band interferometric data could be explained simultaneously. Yet, the L band observations were clearly over-estimated and suggest a stellar radius almost 1.5 times larger. The dust shell has an optical depth almost ten times greater than in the case of α Ori. In addition to having an inner radius close to the star, the shell extends to more than 100 stellar radii.

Like for R Leo, the L band data for SW Vir were over-estimated when the model was adjusted so that it agreed with the K band interferometric data and near- and mid-infrared photometry. A model radius roughly 1.5 larger would be required to bring the model into agreement with the L band data. The optical thickness is very similar to that found for α Ori. The dust shell thickness is in between that of α Ori and R Leo. Also, the inner radius has an intermediate value. The latter is consistent with the stellar effective temperature which lies between the temperatures of the other two objects. Therefore, it will be very interesting to obtain interferometric N band measurements on this object with MIDI in order to see if they agree with the proposed dust shell.

In summary, the discussed findings suggest that taking into account only a spherical dust shell envelope for late type stars like R Leo and SW Vir does not explain the observational data simultaneously in all bands. In contrast to α Ori, those objects should show a continuous mass loss process which is known for cool stars and Miras (see, e.g., Willson (2000)). At a distance corresponding to the appropriate temperature for a given material, the dust condensates out of molecules flowing out from the star. This means that between the stellar photosphere and the dust forming region there is a molecular gas layer. Since a dust shell model was not sufficient, the question then arises how this layer might affect interferometric observations. Mennesson et al. (2002) present a first attempt to explain the apparent inconsistencies between K and L band interferometric observations by assuming and modeling an extended gaseous layer around cool stars. But also for α Ori, where the dust shell model was in good agreement with observational data, Weiner et al. (2000) reported a stellar diameter in the N band much larger than the one by D94. With the ISI interferometer, they measured the visibility curve close to the first zero, i.e., at spatial frequencies around $47 \cdot 10^5\,\mathrm{rad}^{-1}$, where the dust shell should be completely resolved and its contribution to the correlated flux is negligible. The derived stellar radius was about 27 mas, i.e., again almost 1.5 times larger than the one used by D94. This means that there should be another component close to the star contributing to the N band flux. Therefore, it seems necessary to include the effects of gas layers into the model which would considerably change the radiation transfer behaviour.

Chapter 6

Conclusion

Within the framework of calibrating MIDI, several tasks had to be pursued and solved for this work. The piezo stages forming the Internal Delay Line were tested for their static and dynamic behaviour. Special attention was payed to the test setup. It was chosen such that both stages were included in the optical path, which corresponds to the actual setup in MIDI. The stages' properties were found to satisfy the requirements and to be suitable to perform the observing scan modes currently foreseen for MIDI.

A further task was the provision of calibration light sources for laboratory use. For the narrow-band source, a CO_2 laser had to be equipped with an attenuation dimming the radiation to a level suitable for MIDI. An appropriate design has to be found and the corresponding parts were specified. Effort was also put into finding a backup system for this laser source. A solution was found in a laser diode system which is very compact and easy to operate. It shows several narrow output wavelengths depending on operation mode. Yet, with the dispersive capabilities of MIDI, those should be clearly separable which makes each wavelength appear as a single laser. Thus, the diode system can be a useful tool for application in MIDI. Likewise, a broad-band source had to be designed and set up. Both the CO_2 laser and the broad-band source fulfil their purpose and are actively used for various tests in the laboratory. At the VLTI, the calibration light sources are currently upgraded by a mid-infrared source. For this, a setup was chosen which is very similar to the one used for the laboratory tests.

For the calibration of the wavelength location on the detector, a reference material was provided as a foil with its transmission spectrum. Shining light from a broad-band source into MIDI and measuring the transmission spectrum yielded the desired "spectral axis" on the detector with good precision. This procedure appears reliable and can be used to verify the spectral calibration whenever it is necessary, e.g., after dis- and re-assembling the instrument.

A procedure for the mutual calibration of the Internal Delay Line and the spectral axis on the detector was proposed. To the extent allowed by the integration status of the MIDI instrument at the time, this procedure was demonstrated and shown to be applicable in principle.

Calibrator stars are used during observation to calibrate for instrumental and atmospheric effects. Out of the list of candidates for MIDI calibrator stars, several objects were selected for interferometric observations in the near-infrared regime. The observations were performed in the course of this project and the results are presented in this work. Measurements in narrow-band filters showed differential effects of the visibility at different wavelengths. Comparison of these results with astrophysical models of the calibrator stars is still ongoing. A good agreement should increase confidence that the models are also applicable and give a good prediction of the stellar properties at mid-infrared wavelengths.

An astrophysical issue was addressed by the study of three evolved stars with different amounts of circumstellar material. Observational data, taken at different wavelength bands, were compared to spherical dust shell models of these objects. Preliminary conclusions showed that, in general, these models are not sufficient to explain the observational data in all wavelength bands simultaneously. Out of the three studied stars, the intermediate one did not have mid-infrared interferometric data. MIDI will be able to provide those and to extend this kind of observations to a vastly larger sample of objects. This will allow a much deeper study of the topic.

First scientific observations of this kind with MIDI at the VLTI are expected for early 2003. This will also be the time when the calibration work described in this thesis will come to fruition. To date, the MIDI instrument is prepared for ESO's Preliminary Acceptance Test at the MPIA in Heidelberg in September 2002. It is foreseen to install the instrument at the VLTI in November 2002. First test observations are expected before the end of the year 2002.

Appendix A

Signal Estimates

A.1 Limiting Magnitude for MIDI

In order to estimate a limiting magnitude for MIDI, one has to consider the Signal to Noise Ratio (SNR) for an object. As an interferometer, MIDI will measure visibilities from interference patterns. Therefore, the signal is taken as the *correlated flux*, i.e., the product $P_{cor} = V_{obj} \cdot P_0$ of the object visibility and the total power received from the object by one telescope (see section 2.2.1). The photon noise of the total thermal background will enter as noise term into the SNR.

We use the following relations in the derivations thereafter:

- area A of a telescope dish with diameter D:

$$A = \pi (D/2)^2 \tag{A.1}$$

- angular radius ϕ of diffraction limited focal point ("Airy disk"):

$$\phi = \lambda / D \tag{A.2}$$

The Airy disk contains the fraction $q = 75\,\%$ of the total energy.

- solid angle Ω of Airy disk seen from telescope aperture:

$$\Omega = \pi \phi^2 \tag{A.3}$$

- throughput (étendue) ET of optical system:

$$ET = A\Omega = (\pi/2)^2 \cdot \lambda^2 = c_E^2 \cdot \lambda^2 \tag{A.4}$$

ET is independent of the telescope diameter and conserved throughout the optical system.

- relation between wavelength λ, frequency ν, and speed c of light:

$$c = \nu\lambda \quad \Rightarrow \quad \Delta\nu/\nu = \Delta\lambda/\lambda \tag{A.5}$$

- energy E of photon (h is the Planck constant):

$$E = h\nu = hc/\lambda \tag{A.6}$$

The optical train of the VLTI is collectively regarded as one radiator at ambient temperature with the wavelength dependent Planck function B_λ. Multiplying B_λ by the emissivity ϵ when calculating the received energy indicates the fact that the optical train is not an ideal blackbody. Correspondingly, the transmissivity of the VLTI optical train is $(1-\epsilon)$. To translate the emission of the optical train into an apparent brightness S_ν^{wo} on the sky, one considers the *emitted* spectral flux density ϵB_λ as *transmitted* through the optical train. Therefore, the following relation applies:

$$S_\nu^{wo} = \frac{\Omega \cdot \epsilon B_\nu}{(1-\epsilon)} = \frac{\Omega \cdot \epsilon B_\lambda (\lambda^2/c)}{(1-\epsilon)}, \qquad [S_\nu^{wo}] = \mathrm{W\,m^{-2}\,Hz^{-1}}. \tag{A.7}$$

The number N_{el} of photo electrons collected by the detector in an Airy disk during integration time t_{int} is:

$$N_{el}^{wo} = q \cdot \eta_{det}\theta_{co} \cdot \frac{t_{int}\, A\, \Omega\, \Delta\lambda}{hc/\lambda} \cdot \epsilon B_\lambda, \tag{A.8}$$

where η_{det} is the quantum efficiency of the detector and θ_{co} the overall transmissivity of the MIDI Cold Optics. The photon noise (or shot noise) induces $\sqrt{N_{el}}$ photo electrons. For the corresponding photon noise, σ_{wo}, projected on the sky, it holds

$$\begin{aligned} \sigma_{wo}^2 &= \left(\frac{h\nu\sqrt{N_{el}}}{t_{int}\Delta\nu A \cdot \eta_{det}\theta_{co}(1-\epsilon)} \right)^2 \\ &= K_{co} \cdot \frac{S_\nu^{wo}}{A\,(1-\epsilon)} \cdot \frac{(\lambda/\Delta\lambda)}{t_{int}}, \qquad [\sigma_{wo}] = \mathrm{W\,m^{-2}\,Hz^{-1}}, \end{aligned} \tag{A.9}$$

with the constant K_{co} defined as

$$K_{co} = \frac{q\,h}{\theta_{co}\,\eta_{det}}. \tag{A.10}$$

K_{co} describes the Cold Optics of MIDI, so it is purely hardware dependent and usually not changeable by an observer. Likewise, the second term in equation (A.9) depends only on conditions of the Warm Optics outside MIDI. Under normal conditions, only the third term can be influenced by the observer. It changes with integration time and filter in use.

Also the atmosphere contributes to this background. Its contribution is highly dependent on the observing site, weather conditions etc. Similar to equation (A.8), but considering that this light has to *pass* through the VLTI optics, one can find for the number N_{el}^{wo} of induced photo electrons in an Airy disk

$$N_{el}^{sky} = q \cdot \eta_{det}\theta_{co} \cdot \frac{t_{int}\, A\,(\Delta\lambda/\lambda)}{h} \cdot (1-\epsilon) S_\nu^{sky} \tag{A.11}$$

and for the noise of the sky background

$$\sigma_{sky}^2 = K_{co} \cdot \frac{S_\nu^{sky}}{A\,(1-\epsilon)} \cdot \frac{(\lambda/\Delta\lambda)}{t_{int}}. \tag{A.12}$$

The total noise then is $\sigma = \sqrt{\sigma_{wo}^2 + \sigma_{sky}^2}$. If all hardware and environment dependent terms are collected in one constant K_{henv}, i.e.,

$$K_{henv}^2 = \frac{K_{co}(S_\nu^{wo} + S_\nu^{sky})}{A\,(1-\epsilon)}, \tag{A.13}$$

σ^2 can be written as

$$\sigma = K_{henv}^2 \cdot \frac{(\lambda/\Delta\lambda)}{t_{int}}, \tag{A.14}$$

In order to estimate a limiting magnitude m_{lim} with a given SNR, the signal is identified on one side with the number $SNR \cdot \sigma$ and on the other side with the measured correlated flux as mentioned before. Yet, one has to consider that this *measured* flux may be deteriorated compared to the *actual* correlated flux P_{cor} of the source by imperfections in tip-tilt correction, in VLTI and MIDI optics like misalignment or at the beam combiner, and by differential dispersion by air in the optical train. A detailed analysis of different effects with respect to the interferometric signal, including instrumental and atmospheric influences, is reported by Porro et al. (1999). It is estimated for MIDI that the measured visibility V will be reduced by an overall factor $S_{all} = 0.6$ relative to the object visibility V_{obj} (comp. section 2.2). One can write therefore:

$$SNR \cdot \sigma = V \cdot P_0 = S_{all} \cdot V_{obj} \cdot P_0, \tag{A.15}$$

yielding for the actual correlated flux

$$P_{cor} = V_{obj} \cdot P_0 = P_0 \cdot V / S_{all}. \tag{A.16}$$

The limiting magnitude is therefore estimated by:

$$\begin{aligned} m_{lim} &= -2.5 \cdot \lg\left(\frac{P_{cor}}{I_{ref}}\right) \\ &= -2.5 \cdot \lg\left(\frac{10\,\sigma}{S_{all} \cdot I_{ref}}\right) \\ &= -2.5 \cdot \lg\left(\frac{10 K_{henv}}{I_{ref}} \cdot \frac{\sqrt{(\lambda/\Delta\lambda)}}{\sqrt{t_{int}}}\right) + 2.5 \cdot \lg(S_{all}). \end{aligned} \tag{A.17}$$

This means, as S_{all} is contained in the interval $[0, 1]$, that m_{lim} will be shifted towards higher brightnesses.

For a numeric evaluation of the presented values at a 10σ level, i.e., $SNR = 10$, the following parameters might be used:

$D = 8.0\,\mathrm{m}/1.8\,\mathrm{m}/0.40\,\mathrm{m}$	diameter of one UT/AT/Siderostat
$\Delta\lambda = 5\,\mu\mathrm{m}$	width of full N band around $\lambda = 10\,\mu\mathrm{m}$
$B_\lambda = 8.4 \cdot 10^6\,\mathrm{W/m^2\,m\,sr}$	Planck function at $\lambda = 10\,\mu\mathrm{m}$ and 290 K
$t_{int} = 25\,\mathrm{ms}$	typical integration time; 1/4 of assumed atmospheric coherence time
$\epsilon = 0.65$	overall emissivity of warm optics (Koehler et al., 2002)
$\theta_{co} = 0.6$	overall transmissivity of cold optics in MIDI
$\eta_{det} = 0.4$	average quantum efficiency of detector

Furthermore, for good observing site conditions, the overall N band sky background is roughly $S_\nu^{sky}/\Omega = 500\,\mathrm{Jy}/('')^2$ (Smith and Harper, 1998, Table 1), i.e., $2.1 \cdot 10^{13}\,\mathrm{Jy/sr}$, where $1\,\mathrm{Jy} = 10^{-26}\,\mathrm{W/m^2\,Hz}$. The reference intensity for 0 mag in the N band is roughly $I_{ref} = 40\,\mathrm{Jy}$ (Léna et al., 1998). Table A.1 shows the numbers following from these parameters.

The calculations presented here show the order of magnitude of the different contributions to the total signal which is received by the detector. The signal of a 0 mag object is about 1 % of the thermal background originating from the UT warm optics[1]. Clearly, due to the well depth

---

[1] The according number of photo electrons can be deduced by introducing I_{ref} in place of S_ν^{sky} in equation (A.11).

Table A.1: Limiting magnitude calculation.

	UTs	ATs	Siderostats
$A\,(\mathrm{m}^2)$	50	2.5	0.13
$\phi\,('')$	0.26	1.1	5.2
$\Omega\,(\mathrm{sr})$	$4.9 \cdot 10^{-12}$	$9.7 \cdot 10^{-11}$	$2.0 \cdot 10^{-9}$
N_{el}^{wo}		$1.5 \cdot 10^{9}$	
$S_\nu^{wo}\,(\mathrm{Jy})$	2600	$5.0 \cdot 10^{4}$	$1.0 \cdot 10^{6}$
$\sigma_{wo}\,(\mathrm{Jy})$	0.049	0.97	20
N_{el}^{sky}		$6.2 \cdot 10^{7}$	
$S_\nu^{sky}\,(\mathrm{Jy})$	100	2100	$4.2 \cdot 10^{4}$
$\sigma_{sky}\,(\mathrm{Jy})$	0.0099	0.20	4.0
$K_{henf}\,(\mathrm{Jy}\,\sqrt{\mathrm{s}})$	0.0056	0.11	2.2
m_{lim}	4.2	0.96	-2.3

for one detector pixel of about 10^7 electrons (see section A.2), the signal has to be distributed over at least 100 pixels. Further, the dependencies on values chosen by observers become clear in equation (A.17).

A number of aspects were not considered in detail. A major point is the wavelength dependence of all numbers describing hardware components in (A.10) and (A.13), namely the emissivity $\epsilon(\lambda)$ of the Warm Optics, the transmissivity $\theta_{co}(\lambda)$ of the Cold Optics, and the quantum efficiency $\eta_{det}(\lambda)$ of the detector. The thermal emission of the telescope optics is evaluated for the N band close to its maximum and therefore strongly varies with wavelength. Also the sky brightness $S_\nu^{sky}(\lambda)$ is anything but constant in the N band and varies with time and weather conditions (Chamberlain et al., 2000; Smith and Harper, 1998). Likewise, the emission of the 0 mag reference star changes with the wavelength in the N band. As a result, the limiting magnitude $m_{lim}(\lambda)$ as computed by equation (A.17) will change with wavelength.

An extended sensitivity estimate, taking into account the various spectral dispersive capabilities of MIDI and detector read noise, is given by Leinert (1999).

A.2 Radiation Sources and Detector Response

In this section some relations are derived which connect the detector response to the flux coming from various radiation sources, entering the MIDI dewar, and focused on the detector by one of the available cameras. The MIDI detector and Cold Optics are characterised by the following parameters:

- Number of electrons in pixel: n_{det} ; $[n_{det}] =$ El./ pixel
  Saturation of a pixel at $n_{sat} = 10^7$ El. / pixel
  Quantum efficiency: $\eta_{det} = 40\,\%$
  1 pixel $= (50\,\mu\mathrm{m})^2 = 25 \cdot 10^{-6}\,\mathrm{cm}^2$
  Transmission Cold Optics: $\theta_{co} = 0.6$

These values are used in the following considerations.

A.2.1 Laser Sources

In the following calculations, it is assumed that a collimated beam arrives from the laser sources at the MIDI dewar (see section 4.3). The signal of the thermal background will not be considered for the numeric results.

- Parameters:
  - Pixel number p^c in Airy disk of angular extent $\pi \cdot (\lambda/\mathrm{D})^2$:

	Camera Type		
	Pupil	Imaging	Spectroscopic
Laser	$p_L^P = \pi \cdot 18^2 = 1020$	$p_L^I = \pi \cdot 3^2 = 28.3$	$p_L^S = \pi \cdot 2 \cdot 1 = 6.28$
Diode	$p_D^P = 616$	$p_D^I = 17.1$	$p_D^S = 3.80$

(A.18)

    The Airy disk holds $q = 75\,\%$ of the total energy.

    Since the Diode provides a collimated beam with 14 mm diameter, as opposed to the standard input beam diameter of 18 mm, the pixel numbers for the Diode were derived by scaling the ones for the Laser by $s = (14\,\mathrm{mm}/18\,\mathrm{mm})^2 = 0.605$ so that $p_D^c = s \cdot p_L^c$.

  - Integration time t_{int}:
    typically $t_{int} = 25\,\mathrm{ms}$ ($t_{int} \nearrow \;\; \Rightarrow$ allowed radiation $\searrow$!)
  - Photon energy E_γ: $E_\nu = h\nu = hc/\lambda = E_\lambda$
    CO$_2$ Laser: $E_{10.6\,\mu m} = 1.87 \cdot 10^{-20}\,\mathrm{Ws}$
    Laser Diode: $E_{9.0\,\mu m} = 2.21 \cdot 10^{-20}\,\mathrm{Ws}$
  - Beam diameter D_i, area $A_b = \pi(D_i/2)^2$
    CO$_2$ Laser: $D_L = 18\,\mathrm{mm}, A_L = 2.55\,\mathrm{cm}^2$
    Laser Diode: $D_D = 14\,\mathrm{mm}, A_D = 1.54\,\mathrm{cm}^2 = s \cdot A_L$ (A.19)

- Relation between flux density I_{in}, coming from a radiation source into *one* beam, and its detector response n_{det}:
  - Let r be the rate of *electrons* in one pixel per integration time:

$$r_{det} = \frac{n_{det}}{t_{int}} \quad , \quad [r_{det}] = \frac{\mathrm{El.}}{\mathrm{s\,pixel}} \tag{A.20}$$

Correspondingly, let r_γ be the rate of *photons* into one pixel per integration time, not considering MIDI cameras:

$$r_\gamma = \frac{r_{det}}{\eta_{det}\theta_{co}} = \frac{n_{det}}{\eta_{det}\theta_{co}t_{int}} \quad , \quad [r_\gamma] = \frac{\text{ph.}}{\text{s pixel}} \quad , \tag{A.21}$$

which translates into a power value by

$$J_{det} = E_\gamma \cdot r_\gamma = \frac{E_\gamma n_{det}}{\eta_{det}\theta_{co}t_{int}} \quad , \quad [J_{det}] = \frac{\text{W}}{\text{pixel}} \quad , \tag{A.22}$$

* Total power P_{in} of incoming beam, MIDI cameras considered:

$$q \cdot P_{in} = (\text{A.18}) * (\text{A.22}) = p^c \cdot J_{det} = \frac{p^c E_\gamma n_{det}}{\eta_{det}\theta_{co}t_{int}} \tag{A.23}$$

flux density of incoming (homogeneous) beam:

$$I_{in} = (\text{A.23})/(\text{A.19}) = P_{in}/A_b = \frac{p^c E_\gamma}{A_b q \eta_{det}\theta_{co}} \cdot \frac{n_{det}}{t_{int}} \overset{(\text{A.20})}{=} \frac{p^c E_\gamma}{A_b q \eta_{det}\theta_{co}} \cdot r_{det} \tag{A.24}$$

Overall expressions:

$$\boxed{n_{det} = t_{int} \cdot r_{det} \quad , \quad r_{det} = h_i^c \cdot I_{in} \quad , \quad h_i^c = \frac{A_b\, q\, \eta_{det}\, \theta_{co}}{p^c\, E_\gamma} = \frac{A_b\, q\, \eta_{det}\, \theta_{co}}{p^c\, h\, c} \cdot \lambda} \tag{A.25}$$

with h_i^c a constant, only hardware depending factor, linking r_{det} and I_{in}. Note that in the present case h_i^c changes from the CO_2 laser to the laser diode only due to the different wavelength λ and not due to geometry. The reason is that the scaling factor s contained both in A_b and in p^c cancels. The different camera types listed in (A.18) then yield:

	Camera Type		
	Pupil	Imaging	Spectroscopic
Laser	$h_L^P = 3.20 \cdot 10^{13}$	$h_L^I = 1.15 \cdot 10^{15}$	$h_L^S = 5.19 \cdot 10^{15}$
Diode	$h_D^P = 2.72 \cdot 10^{13}$	$h_D^I = 9.79 \cdot 10^{14}$	$h_D^S = 4.40 \cdot 10^{15}$

$$[h_i^c] = \frac{\text{El. cm}^2}{\text{W ms pixel}} \tag{A.26}$$

Thereby, it was chosen $q = 1$ to allow for a safety margin.

- Power balance (nominal) for radiation sources after passing attenuating optics (cf. section 4.3.1):

	Diameter	F (W)	I (W/cm^2)
CO_2 Laser	18 mm	$3.18 \cdot 10^{-10}$	$1.25 \cdot 10^{-10}$
Laser Diode	14 mm	$2.50 \cdot 10^{-10}$	$1.62 \cdot 10^{-10}$

The Laser Diode with its output power does not exceed the technical limits for devices of laser class 1.

Put into (A.25) and considering a reducing factor of 0.5, due to the MIDI Warm Optics splitting the incoming source beam into two channels, yields:

	Camera Type		
	Pupil	Imaging	Spectroscopic
CO_2 Laser	$r_L^P = 2.00 \cdot 10^3$	$r_L^I = 7.20 \cdot 10^4$	$r_L^S = 3.24 \cdot 10^5$
Laser Diode	$r_D^P = 2.20 \cdot 10^3$	$r_D^I = 7.93 \cdot 10^4$	$r_D^S = 3.57 \cdot 10^5$

$$[r_i^c] = \frac{\text{El.}}{\text{ms pixel}} \tag{A.27}$$

- Following equation (A.20), saturation is reached after $t_{int} = t_{sat}$:

	Camera Type		
	Pupil	Imaging	Spectroscopic
CO_2 Laser	$t_L^{P,sat} = 5\,000\,\mathrm{ms}$	$t_L^{I,sat} = 139\,\mathrm{ms}$	$t_L^{S,sat} = 30.9\,\mathrm{ms}$
Laser Diode	$t_D^{P,sat} = 4\,540\,\mathrm{ms}$	$t_D^{I,sat} = 126\,\mathrm{ms}$	$t_D^{S,sat} = 28.0\,\mathrm{ms}$

(A.28)

Yet, equation (A.28) gives only *upper limits* for t_{sat}, since in this present calculation the signal of the thermal background is not considered!

A.2.2 VLTI Background

From the numbers resulting in section A.1, an estimation can be retrieved for the time t_{sat} in which the detector is saturated by the background signal. Let the total number of background induced photo electrons in the Airy disk be $N_{el}^{tot} = 1.6 \cdot 10^9$. The rate by which they are produced is $r_{el}^{tot} = N_{el}^{tot}/t_{int} = 6.4 \cdot 10^{10}\,\mathrm{El./s}$. For the three different cameras available in MIDI, the Airy disk is distributed on a number p^c of pixels (see (A.18) for the laser). If the saturation level for one pixel is n_{sat}, then it follows for t_{sat}:

$$t_{sat} = p^c \cdot \frac{n_{sat}}{r_{el}^{tot}} \tag{A.29}$$

For the different camera cases this yields:

Camera Type		
Pupil	Imaging	Spectroscopic
$t_{sat}^P = 160\,\mathrm{ms}$	$t_{sat}^I = 4.4\,\mathrm{ms}$	$t_{sat}^S = 0.98\,\mathrm{ms}$

It is to be noted, though, that these numbers can only give a coarse estimation as they depend on the actual configuration, e.g., spatial filters and dispersive elements used.

A.3 Average Flux Density Versus Peak Intensity

When evaluating fluxes for different purposes, certain geometric beam diameters are assumed as precise. In this way average flux densities are calculated. Yet, on one side diffraction causes a smearing of the diameter so that small portions of the flux are also found outside the nominal boundary, on the other side there is usually a peak intensity somewhere in the beam cross section. Therefore, also peak intensities must be regarded when certain limits have to be considered so that e.g. damage to hardware components or persons is to be prevented.

In this section, two commonly occuring beam profiles are treated. They can be solved analytically for the peak intensity in case some mean intensity is given. First, a beam with a Gaussian profile is considered like it is output from laser resonators in the ground mode. The second example deals with an plane wave travelling through a circular aperture and focused by a lens on a detecting device. For some more cases there exist analytical solutions, other intermediate cases are often treated numerically.

Very similar considerations are undertaken for calculating the Strehl ratio S as a figure of merit for the quality of an optical system. The Strehl ratio is the ratio between the intensity on-axis of an aberrated beam in a real optical system and the intensity on-axis of an unaberrated beam in an ideally corrected system (Tyson, 1998).

A.3.1 Gaussian Profile

Let us assume a laser beam in the far field, i.e. well outside the resonator, so that the phase fronts of the light can be regarded as plane and perpendicular to the direction of propagation. Further, let r denote the distance from the beam axis. Then, the intensity $I(r)$ can be described by

$$I(r) = \hat{I} \cdot \exp\left(-\frac{2r^2}{w_0^2}\right), \tag{A.30}$$

where $\hat{I}$ is the axial value and w_0 defines the Gaussian beam radius where the intensity dropped to $1/e^2 = 0.135$ of central value. The FWHM is reached at $r_{1/2} = 0.589 \cdot w_0$. At $2w_0$ the relative intensity is already at 0.03 %. This means that laser beams that are masked by apertures wider than $2 \cdot 2w_0$ may be considered unobscured and so diffraction effects can usually be neglected. An important property of an unobscured Gaussian beam is that it retains its profile throughout an optical system, i.e. because a Gaussian function and its Fourier transform have the same form (Hecht, 1998, Chapter 11).

The total power P_0, that is usually given by laser manufacturers, can be expressed by the two-dimensional (x,y) integral in the plane normal to the beam direction:

$$P_0 = \hat{I} \cdot \int_{-\infty}^{\infty} dx \int_{-\infty}^{\infty} dy \; \exp\left(-\frac{2r^2}{w_0^2}\right), \quad \text{where} \quad r^2 = x^2 + y^2. \tag{A.31}$$

For evaluating the integral, one can utilise the axial symmetry of the problem and change to polar coordinates, or use the known solution of the definite integral:

$$\begin{aligned} P_0 &= \hat{I} \cdot \int_{-\infty}^{\infty} dx \; \exp\left(-\frac{2x^2}{w_0^2}\right) \cdot \int_{-\infty}^{\infty} dy \; \exp\left(-\frac{2y^2}{w_0^2}\right) \\ &= \hat{I} \cdot 2 \int_{0}^{\infty} dx \; \exp\left(-\frac{2x^2}{w_0^2}\right) \cdot 2 \int_{0}^{\infty} dy \; \exp\left(-\frac{2y^2}{w_0^2}\right) \\ &= \hat{I} \cdot \left(2 \cdot \frac{\sqrt{\pi}}{2} \cdot \frac{w_0}{\sqrt{2}}\right)^2 \\ &= \hat{I} \cdot \frac{\pi w_0^2}{2} \end{aligned} \tag{A.32}$$

The average intensity I_0 is calculated as the total power P_0 divided by the cross section of the beam with the radius w_o, i.e., $I_0 = P_0/\pi w_0^2$, and therefore with equation (A.32)

$$\boxed{\hat{I} = 2 \cdot I_0.} \tag{A.33}$$

In words, for an unobscured laser beam which has a Gaussian flux density profile the central peak value is twice as high as the average value.

A.3.2 Circular Aperture

Let a plane light wave of wavelength λ with a power density I_A illuminate a circular aperture of radius a and diameter $D = 2a$. The diffraction pattern in the far field (Fraunhofer approximation) is registered on a screen at distance R. If r is the distance on the screen from the central on-axis point, the irradiance I can be described by the well-known Airy diffraction pattern (Hecht, 1998, Chapter 10)

$$I(\rho) = \hat{I} \left[\frac{2J_1(kar/R)}{kar/R}\right]^2 \quad , \quad k = 2\pi/\lambda, \tag{A.34}$$

where $r^2 = x^2 + y^2$ with (x,y) the Cartesian coordinates.

Similar to equation (A.31), the total power $P_0 = I_A \cdot (\pi a^2)$ must also be found on the screen and therefore

$$I_A \cdot (\pi a^2) = P_0 = \hat{I} \cdot \int_{-\infty}^{\infty} dx \int_{-\infty}^{\infty} dy \, \left[\frac{2J_1(kar/R)}{kar/R}\right]^2 . \tag{A.35}$$

Changing to polar coordinates and inserting the substitution $\rho = kar/R$ yields

$$I_A \cdot (\pi a^2) = \hat{I} \cdot 2\pi \cdot \left(\frac{R}{ka}\right)^2 \cdot \int_0^{\infty} d\rho \, \rho \left[\frac{2J_1(\rho)}{\rho}\right]^2 . \tag{A.36}$$

The value for the integral is found to be exactly 2 (Gradshteyn and Ryzhik, 2000, Number 6.538), and so it follows

$$\hat{I} = \frac{\pi^2}{16} \cdot \frac{D^2 \cdot D^2}{R^2 \cdot \lambda^2} \cdot I_A . \tag{A.37}$$

If a lens with focal length f is placed in the aperture, the diffraction pattern can be observed in the focal plane, and in the above relation f enters for R which results in

$$\boxed{\hat{I} = \left(\frac{\pi}{4}\right)^2 \cdot \left(\frac{D}{f}\right)^2 \cdot \left(\frac{D}{\lambda}\right)^2 \cdot I_A .} \tag{A.38}$$

It is noted that f/D equals the f-ratio $F/\#$ of the lens, and λ/D is in good approximation the FWHM of the central peak enclosed by the first dark ring of the Airy pattern. The FWHM contains 75 % of the total power, whereas the full central peak contains 84 %.

Rewriting equation (A.38) in a different form yields

$$\hat{I} = \left[\frac{\pi(D/2)^2}{f \cdot \lambda}\right]^2 \cdot I_A = \left[\frac{\textit{Area of aperture}}{f \cdot \lambda}\right]^2 \cdot I_A . \tag{A.39}$$

It is interesting to note that the right, i.e., generalised expression in equation (A.39) also holds e.g. for a rectangular aperture. A more general treatment of this topic, taking into account the Huygens-Fresnel principle in an aberration free system, can be found, e.g., in Born and Wolf (1999, Section 9.1).

Appendix B

Retrieving Visibilities by Long Scan Fourier Analysis

This section describes the overall principle of the data reduction like it is performed for the FLUOR instrument. The data reported in section 5.1.3 were retrieved by this method.

When single mode fibres become available for the N band[1] they could be used as spatial filters. This would make possible to operate MIDI in an acquisition mode similar to the one used with FLUOR. The main difference would consist in additional contributions to the noise by the photometric background fluctuations of the atmosphere (see section 3.2.3) and of the warm optics in the optical train. Evaluation of these fluctuations will be one of the first tasks to be addressed when MIDI arrives on Mt. Parranal.

B.1 General Description

The basic idea of retrieving visibilities by long scan Fourier analysis is to perform a long OPD scan extending over several wavelengths within the coherence time. Depending on the scan speed, the interference fringes appear with a certain frequency. Fourier transforming the signal yields its power spectrum. The amount of energy found at the fringe frequency contains information on the object visibility.

In the special case of the FLUOR instrument, two incoming beams are each injected into a single-mode fluoride fibre. From these photometric input fibres, light is partially coupled out and recombined interferometrically by another pair of fibres. To acquire the fringe signal of an object, the OPD is scanned around zero by a piezo-driven fast delay line. During one such scan, the four output signals are recorded by a NICMOS3 detector. The speed of the sweep and therefore the change of the nominal OPD is kept constant during data acquisition and is chosen so that the fringe frequency is well above the turbulence frequency contributions.

Single mode fibres have the advantage to filter out wavefront corrugations caused by atmospheric turbulence. The corresponding phase fluctuations are translated into photometric fluctuations which can easily be monitored. The remaining atmospheric effect is the fundamental mode of differential piston between the two telescopes which mainly introduces signal noise in the reduced interferometric data. The likewise generated signal bias can usually be neglected as it is much smaller than the statistical error on acquired visibilities if the fringe packet is

---

[1] To date, market searches for available fibres are still ongoing.

scanned fast enough.

Besides the signal recording during the scan of the OPD, three more data sets are recorded which enter the data reduction and calibration of the instrument. While pointing to the astronomical object, each beam is blocked and the other one is open. These two photometric measurements are taken just before the interferometric sets. For the third data set, both beams are blocked in order to monitor dark current and zero photometric level. This set is taken before *and* after the interferometric measurements so that the instrument is optimally described during data acquisition.

These data allow to deduce the modulus μ of the complex coherence factor $\boldsymbol{\mu} = \mu e^{i\phi_\mu}$ for an object. The data reduction procedure is described in more detail in the following section. It leads to very accurate measurements with errors smaller than 1% of the object visibilities.

If atmospheric effects are neglected or considered as fully removed by the spatial filtering in the single-mode fibres, and the modulus T_i of the instrumental transfer function $\mathbf{T_i}$ is known, the modulus V of the object visibility $\mathbf{V}$ can be derived from

$$\mu = T_i \cdot V \quad . \tag{B.1}$$

In order to obtain the transfer function T_s for a science object, interferometric measurements are performed on two calibrator stars A and B prior to and after the science object. For the calibrators the same data reduction process applies as for the science object, and the relation (B.1) is also true. Yet, for the calibrators their visibilities V_A and V_B are assumed as known, which allows to derive the transfer functions T_A and T_B. T_s is then yielded by linear interpolation between those two.

B.2 Data Analysis

In Coudé Du Foresto et al. (1997), the derivation of μ^2 from FLUOR data is detailed, whereas Perrin et al. (1998) present the calibration process for the data. Perrin (2002) gives an update of the reduction process including signal correlations. Here, the main relations are compiled and the major steps which lead from raw data to the modulus of the coherence factor and eventually to the visibility of the observed object are described.

In a first step, one has to retrieve an estimator for the photometric signal which is coupled into the two beams. Let $M_{P_n}(x)$ be the measured signal in one of the photometric channels ($n = 1, 2$). The dependence on x is explicitly stated to indicate that a data sequence is taken in real space. M_{P_n} is the sum of the actual photometric signal P_n and an additive detector noise b_{P_n}:

$$M_{P_n}(x) = P_n(x) + b_{P_n}(x) \quad . \tag{B.2}$$

Let further $\tilde{\mathbf{M}}_{P_n}(\sigma) = \tilde{M}_{P_n}(\sigma)\, e^{i\phi(\sigma)}$ denote the Fourier transformed measured signal:

$$\tilde{\mathbf{M}}_{P_n}(\sigma) = \mathcal{F}\{M_{P_n}(x)\} \quad , \quad M_{P_n}(x) = \mathcal{F}^{-1}\{\tilde{\mathbf{M}}_{P_n}(\sigma)\} \quad , \tag{B.3}$$

with the wavenumber σ the conjugate variable to the position x. It can be shown that the estimator $\widehat{P_n}$ of P_n that minimises the mean quadratic error of the actual signal is obtained by applying optimal filtering (Press et al. (1999)):

$$\widehat{P_n}(x) = \mathcal{F}^{-1}\{W_n(\sigma)\, \tilde{\mathbf{M}}_{P_n}(\sigma)\} \quad , \tag{B.4}$$

with $W_n(\sigma)$ the Wiener filter, which is expressed by:

$$W_n(\sigma) = \frac{\tilde{M}^2_{P_n}(\sigma) - \tilde{b}^2_{P_n}(\sigma)}{\tilde{M}^2_{P_n}(\sigma)} \quad . \tag{B.5}$$

This relation holds, if the signal and the noise are assumed as uncorrelated. $\tilde{b}^2_{P_n}$ is estimated from the averaged power spectrum of the background measurements when both beams are blocked.

As next step the photometric properties of the instrument are determined. For this, the two beams have to be recombined fully incoherently. Given this case, the output I_m ($m = 1, 2$) is linked with the photometric signals by

$$I_m = \bar{\kappa}_{m1} P_1 + \bar{\kappa}_{m2} P_2 \quad . \tag{B.6}$$

$\bar{\kappa}_{mn}$ comprises the transmissions of the respectively involved couplers and the detector's global gain as well as its efficiency, all these properties integrated over the wavelength range of the filter in use. This is where the calibration measurements come in at which one of the beams is blocked. If, for example, signal P_2 in eq. B.6 is set to zero, the output is simply proportional to P_1 by the constant $\bar{\kappa}_{m1}$. In general, the Wiener filtering from eq. (B.4) is applied to the signal I_m in an analogous way, which yields $\bar{\kappa}_{mn}$ by

$$\bar{\kappa}_{mn} = \frac{\widehat{I_m}}{\widehat{P_n}} \quad . \tag{B.7}$$

Going to coherent beam recombination, and dropping the index m, let $M(x)$ be the measured interferometric output signal, in analogy with (B.2):

$$M(x) = I(x) + b_I(x) \quad . \tag{B.8}$$

As a further step, in order to retrieve the coherence factor μ from the pure interferometric term, one has to subtract the photometric contributions from the measured signal, normalise to the photometric signals which corrects for the photometric fluctuations induced by atmospheric effects, and change to the wave number domain. This procedure yields the number $\tilde{\mathbf{M}}_{cor}(\sigma)$ with

$$\tilde{\mathbf{M}}_{cor}(\sigma) = \mathcal{F}\left\{ \frac{M(x) - \bar{\kappa}_1 \widehat{P_1}(x) - \bar{\kappa}_2 \widehat{P_2}(x)}{2\sqrt{\widehat{P_1}(x)\widehat{P_2}(x)}} \right\} \quad , \tag{B.9}$$

which describes the corrected interferogram in Fourier space.

If there is no piston compensation in a stellar interferometer, the phase information of the interferogram is lost, and one can measure only the modulus $\tilde{M}_{cor}(\sigma)$ of its Fourier transform. The squared modulus $\tilde{M}^2_{cor}(\sigma)$ describes the spectral power density of the corrected interferogram. If the differential piston is sufficiently small, and therefore the Fourier relation between spectral power at a wavenumber σ and the signal form is not disturbed significantly, it can be assumed that some fringe energy is just redistributed in the power spectrum. Yet, the total amount S_M of spectral energy should remain the same:

$$S_M = \int_{Band} \tilde{M}^2_{cor}(\sigma) \mathrm{d}\sigma \quad . \tag{B.10}$$

Up to now, S_M still contains the error signal originating from b_I. Yet, b_I can again be estimated from the background sequences with both beams blocked. For an estimator $\widehat{S}_b$ of the background contribution to S_M one can process each background sequence by the same procedures (B.9) and (B.10) as described for M. All the single power spectra S_b resulting from this treatment are then averaged to one number $\widehat{S_b}$, containing also the photon noise bias (Perrin, 2002). This contribution can be subtracted from S_M which yields the value $\widehat{S}$ with

$$\widehat{S} = S_M - \widehat{S}_b \tag{B.11}$$

as an unbiased estimator for the spectral energy of the fringe signal.

In a last step, the overall measured value $\overline{\mu}$ of the modulus of the coherence factor, integrated over the observation bandpass, has to be deduced. For practical reasons[2], it is more convenient to work with its square $\overline{\mu^2}$. $\overline{\mu^2}$ is the normalised integral of the squared modulus of the coherence factor, scaled by the overall spectral properties of the object and optical properties of the instrument. The normalisation is applied with respect to the integrated product of those properties. It can be shown that the estimator $\widehat{\overline{\mu^2}}$ of $\overline{\mu^2}$ is expressed by

$$\widehat{\overline{\mu^2}} = \frac{4(S_M - \widehat{S}_b)}{\bar{\kappa}_1 \bar{\kappa}_2 F_B} \quad , \tag{B.12}$$

under the assumption that the detector properties are nearly constant in the observation bandpass. In equation (B.12), the constant F_B is called the shape factor and describes the spectrum of the observed object in the observation band. It can be calculated and tabulated for the different object types.

The data analysis as described so far yields a value for $\widehat{\overline{\mu^2}}$ from each interferometric sequence in an observing batch. The resulting set of $\widehat{\overline{\mu^2}}$ shows a distribution due to residual detector noise, photon noise, and atmospheric noise.

---

[2] The modulus of a complex quantity is a biased estimator when additive noise is present. This bias can be removed from the *squared* quantity by subtracting the variance of the noise.

Appendix C

Alignment of Calibration Sources

This is a manual for the alignment of the MIDI calibration sources as they are used at the MPIA in Heidelberg. The sources are placed on the optical table (OT) which will eventually be set up in the Combined Coude Lab (CCL) of the VLTI. Hints for the operation are included. Out of these sources, only the CO_2 laser will be installed at VLTI. An updated installation procedure for the CO_2 laser in the VLTI environment is given by Przygodda and Schuller (2002). Note that there is an additional source on the MIDI table which is not described here.

For the different optical parts described in this chapter, the following abbreviations are used:

Short form	Explanation
ALD	Guiding Laser Diode
BB	Black Body
BD	Beam Dump
BrB	Broad Band Source
BE	Beam Expander, expands beam by factor 10;
BoZ, BaZ, RZ	Bottom Zero, Back Zero, Right Zero; references for OAP alignment
CCL	Combined Coude Lab
EllM	Elliptical Mirror
FiM	Flip-in Mirror
FoM	flat Folding Mirror, adjustable in 24 defined positions
H1, H2, Hc, Hd	holes in inner partitions and output openings respectively
IR	Infra-Red
M1, Mc, Md	flat Mirrors
ND	Neutral Density filters, $T = 1\,\%$
OAP	Off-Axis Paraboloid
PyC	Pyroviewer Camera
SphM	Spherical Mirror
OA	Optical Axis
OT	Optical Table
W1, W2	Wedges, $R_{W1} = 0.5\,\%$ and $R_{W2} = 5.0\,\%$

C.1 CO_2 Laser

For the optical setup of the laser attenuator, refer to fig. C.1.

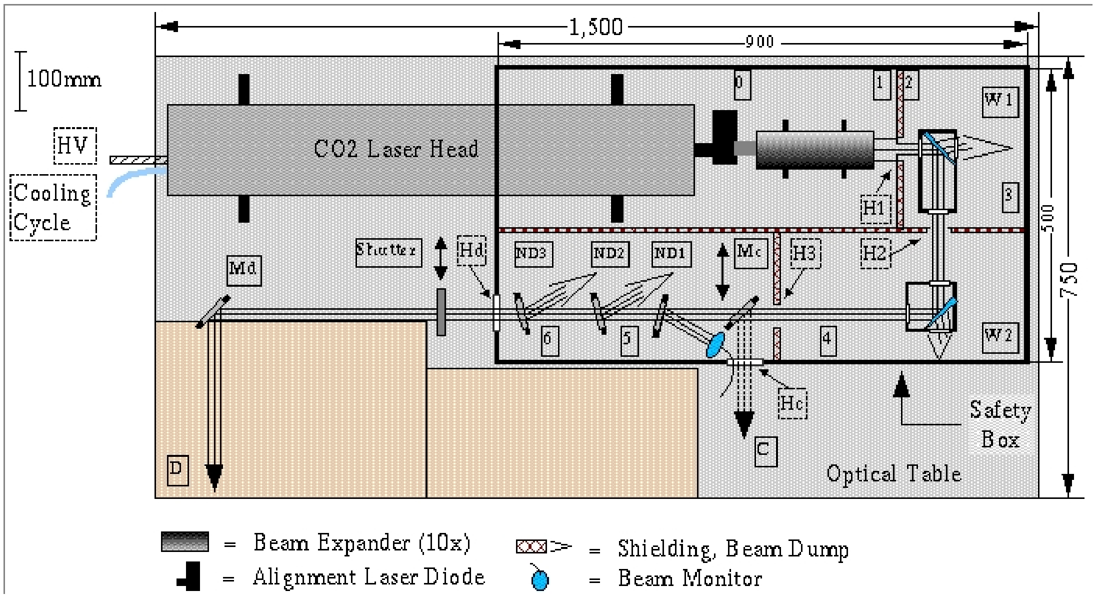

Figure C.1: CO_2 laser and attenuating optics. *cf. Figure 4.13.*

Make sure the visible Alignment Laser Diode (ALD) and the IR laser beam are aligned at all distances.

To align the two beams, use e.g. a separate long optical bench with sliding optical holder and aim on a piece of fire stone or similar material. With a current of 6 mA the IR beam will produce a glowing spot on the stone up to three meters away from laser. Use screws on ALD housing to adjust visible to IR beam in the near and far field respectively.

When the two beams are aligned, one can achieve a good coarse alignment of attenuator optics by using only the visible ALD. Fine alignment of attenuating optics up to W2 can be made later on by using the IR beam and the IR sensitive Pyroviewer Camera (PyC) (see below).

Visual Alignment

- Screw Base Plate (BP) of the laser safety box on the OT so that the upper right fixing hole comes on top of the upper right thread of the OT. The rows of thread holes on the BP are in line with the ones of the OT.

- Place laser head with screws supporting the housing in clamping pieces. Use higher pieces towards cooling system connections, lower pieces towards ALD to compensate for the thickness of BP.

  Adjust screws supporting the laser housing, so that the beam is parallel to optical table. The nominal beam height is 156 mm above the base plate.

- Nominally, the beam follows the rows of thread holes near the middle of each chamber in the box. Screw clamping pieces of laser head accordingly.

- To adjust orientation of Beam Expander (BE), mark the ALD spot where the unexpanded beam hits a screen on the OT. With the BE in the beam, held by 5-axis mount, the centre of the expanded beam must be on the mark at all distances when one slides the screen forth and back.

The focus of the BE must be adjusted later on with the IR beam.

- Place interception protection (not included in fig. 1) between output aperture of ALD and entrance aperture of BE.
- It is possible to align all optics *after* the BE with leaving it in the beam. The centre of the ALD is still visible after reflection at W2 as small red spot.
- Fix W1 ($R = 0.5\,\%$) in housing with space for four additional CaF filters. Place it with centre of reflective surface above thread hole (1). Turn housing such that reflected beam is directed towards thread hole (2).

  Place big Beam Dump (BD) behind W1 so that transmitted IR beam will be dumped there. Remember beam offset and deviation at transmission.
- Fix W2 ($R = 5.0\,\%$) on 3-axis table. Place it with centre of reflective surface above thread hole (2). Adjust W2 such that reflected beam goes along row of thread holes through hole H2 and Hd and hits mirror Md.

  Place small BD behind W2 so that transmitted IR beam will be dumped there. Remember beam offset and deviation at transmission.
- The exact spot for Md is dependent on how the MIDI table and the OT are placed with respect to each other and where exactly the feed through hole in the wall on Paranal will be. Current drawings say there is an overlap of 20 cm regarding the projected edges of the two tables, and the feed through should be right in the middle of the overlap area. Given this, the nominal centre of reflection of Md is 10 cm inwards from the left edge and 31.3 cm from the bottom edge of OT.
- *Now* do IR alignment (see below).
- Fix Neutral Density (ND) filters ND1, ND2, and ND3 in optical mounts. Start inserting them into the beam in reverse order. This allows in each case to place the BDs and the beam monitor correctly. The nominal angle for each ND in respect to the beam direction is 15 degrees.

  When placing the beam monitor, it should possibly not block Hc.
- A word about the safety box: The absorbing coating is quite thick so that the inner parts of the box do not fit that well at times.

IR Alignment

IR alignment of attenuator optics up to W2 and of mirror Md is to be performed *before* installing ND1, ND2, and ND3, using the IR laser beam and the PyC.

- Switch on IR beam and view it with PyC, if possible from MIDI table. Be careful not to focus too much, otherwise it will damage the sensitive layer.
- Without the 20 mm aperture on H1, align beam on W1 so that beam centre is symmetrical with diffraction pattern of housing. Adjust W2 accordingly.
- Centralise 20 mm aperture on beam.
- Adjust telescopic part of BE so that the beam is focused conveniently.

Operation

- Operation of ALD:
  The ALD can be operated independently from the IR laser by turning the switch on the ALD housing.
- Operation of IR laser: For details of operating the CO_2 laser and the water cooler, refer to their respective manuals!
  - Switch on power cord extension. Another extension is tightly fixed to it by which the laser warning lights above the doors of the Experimentierhalle are switched on at the same time.
  - Switch on water cooler for CO_2 laser. Wait a few minutes.
  - Turn on key switch and operate zero start relay to switch on high voltage for CO_2 laser.

C.2 Laser Diode

The task is to focus the Off-Axis Paraboloid (OAP) on the emitting surface of the laser diode.

Remarks

- $f_{OAP} = 40\,\mathrm{mm}$
- One turn of screw with 25 divisions equals 0.25 mm.
- Readings of screws refer to marks *away* from dewar resp. in beam direction.
- Collimated beam runs nominally 60 mm above baseplate and 50 mm inwards from its front short side.
- To be suitable for the MIDI instrument the laser diode must be further attenuated by the neutral density filters ND1, ND2, and ND3. In other words, the laser diode beam corresponds beam 4 in fig. C.1.

Visual aligning

For visual aligning, an eyepiece borrowed from the manufacturer *Mütek* was used.
Once a reference position is found, it is well repeatable. If no major changes are performed, the eyepiece is not needed anymore.

- Make sure that mounting of eyepiece hits pins tightly before tightening screws.
- Looking through the eyepiece, search for little gray block fixed between big white one and shiny wire. Focus z on it by turning z screw. In order to do so, it helps to look for a sharp image of scratch pattern on the front side of the gray block. Mostly, main output area is somewhere between middle in y of gray block and white block. For a start, aim on middle in x.
- A reference position was found as described in the following:

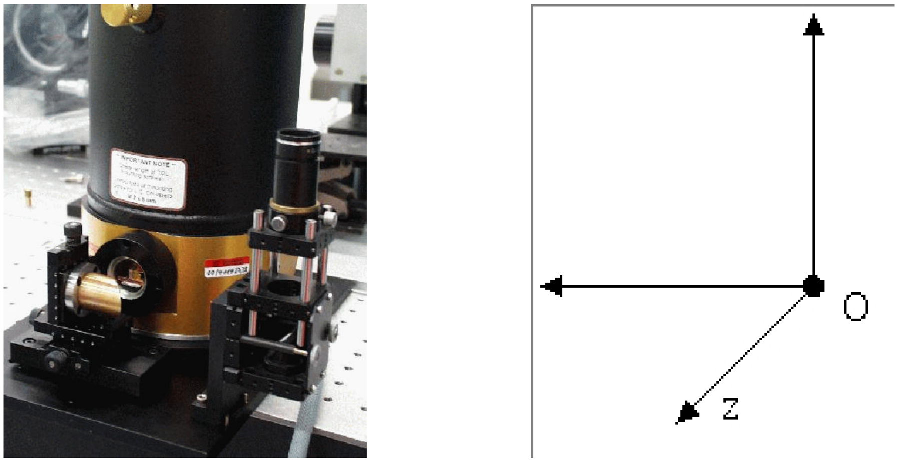

Figure C.2: Alignment of laser diode collimation paraboloid. *The eyepiece was borrowed from the manufacturer (see text).*

- Go to stop at origin of screw coordinate system. For this, turn

  x: counterclock-, y: clock-, z: counterclockwise .

  (Yes, going reversely there is a small hysteresis, but never mind - let stop be reference!)
- in x ($\perp$ baseplate, $\parallel$ output window):
  bottom stop: "20.6"; go up clockwise to "0" ($\hat{=}$ "Bottom Zero (BoZ)");
  upper stop: 22 full turns + 20.5 divisions from BoZ
  standard focus: BoZ + 10 full turns + 3 divisions → "3"
- in y ($\parallel$ baseplate, $\parallel$ output window):
  right stop: "0" ($\hat{=}$ "Right Zero (RZ)");
  left stop: 24 full turns from RZ
  standard focus: RZ + 12 full turns + 15 divisions → "10"
- in z ($\parallel$ baseplate, $\perp$ output window):
  most difficult part! look for sharp image of scratch pattern on gray block;
  back stop: "21.5"; go up clockwise to "0" ($\hat{=}$ "Back Zero (BaZ)");
  front stop: 23 full turns + 20 divisions from BaZ
  standard focus: BaZ + 16 full turns → "0"

Optimise radiation output by IR powermeter. Mind that there might be side modes of diode coupling out at an angle which contribute to total power, but also should degrade quality of interferogram/visibility. Therefore, check also quality of interferogram by interferometer.

Operation

For details of operating the laser diode, refer to respective manuals!

- Fill dewar with l·N_2. Cooling down to operation temperature will take about 5 to 10 minutes.
- Switch on diode electronics.

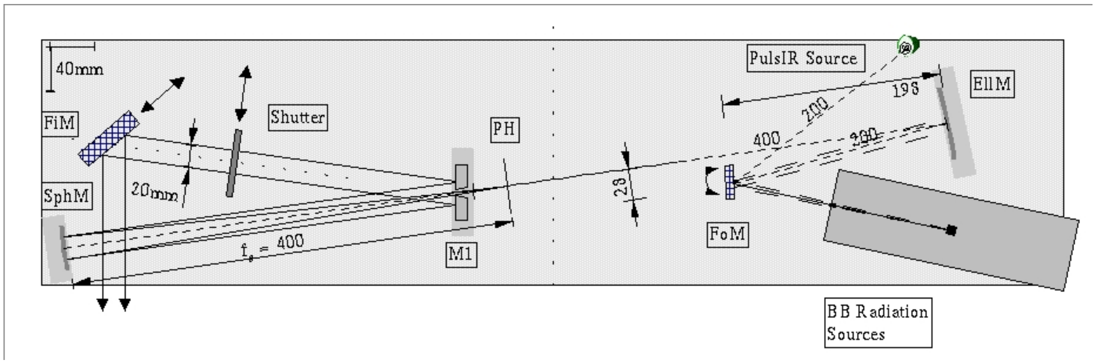

Figure C.3: Broad band source. *cf. Figure 4.16.*

- Select temperature controller by turning knob. Switch on the temperature controller. The operating temperature preset by the manufacturer is $T_{op} = 87\,\mathrm{K}$ and should not be changed usually.
- Select controller for diode current by turning knob. Switch on the current controller. By pressing the "Tune" button one enters a menu where the diode current I_{LD} and so the IR output power can be set. I_{LD} can be selected roughly in the range 0.50...0.95 A. Diode cannot be mistreated, as I_{LD} is controlled by electronics. Press "Esc" button to return to main menu.

C.3 Broad Band Source

For the optical setup of the broad band source (BrB), refer to fig. C.3.

Alignment

For alignment of BrB, use a HeNe laser. Set it up such that beam runs parallel to and 156 mm above base plate of BrB.

- Choose direction of optical axis (OA) on base plate. The nominal axis level is 156 mm above the base plate.
- Centralise Spherical Mirror (SphM) on OA, so that laser beam is retro-reflected.
- Centralise Pin Hole (PH) on OA in focus of SphM. Focal length is $f_S = (400 \pm 3)\,\mathrm{mm}$.
- Place mirror M1 on OA. The central bore is 6 mm wide.
- Currently, after placing M1, SphM is slightly tilted horizontally so that the centre of the collimated beam lies in the middle between central bore and right edge of M1, looking towards PH. This was done to avoid central obscuration of beam, and it is possible since the nominal beam diameter is 20 mm.
- Couple in HeNe laser reversely, so that laser beam is focused on and travels through the PH following the OA.
- Place Elliptical Mirror (EllM) on OA. See fig. C.4 for optical details.

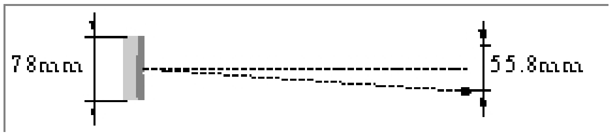

Figure C.4: Optical details of elliptical mirror.

- Place Folding Mirror (FoM) on OA. As it is a kinematic mount for the mirror, the central spot of the laser should be seen in the right third of the mirror when facing the Black Body (BB) and in the left third when facing the PulsIR source.
- Adjust FoM, BB, and PulsIR so that laser is nicely focused on the sources when FoM is turned by two positions.

For a fine alignment, one can use the alignment telescope placed on the Warm Optical Table (see section 3.3.1) and inspect the image of the PH and, respectively, of the radiation sources.

Operation

For details mainly of operating the PulsIR source, refer to respective manual!

- The Flip-in Mirror (FiM) is put in to direct the broad band beam towards MIDI. It is taken out to let the laser beam pass.
- For the BB, switch on controller and set operating temperature by turning knob. Usually, the display shows the current temperature. By pressing button, one can see set temperature.
- For the PulsIR, switch on controller and connect serial cable to PC. Start controller program. Select correct COM port. Reset board. Our current PulsIR sources can be driven as “High Temperature” sources, so select the appropriate option. Set nominal operating temperature. Select operating frequency and duty cycle. There are certain limits to combinations of those two parameters which are controlled by the software.

Bibliography

I. Appenzeller. Das Very Large Telescope. *Physikalische Blätter*, 57(10):35–41, 2001. 2

A. F. Boden. Elementary Theory of Interferometry. 2000. In Lawson (2000). 6, 10

R. v. Boekel, 2002. ESO and University of Amsterdam, private communication. 61

P. Bordé et al. A catalogue of calibrator stars for long baseline interferometry. *Astron. Astrophys.*, 2002. accepted June 2002. 60

Max Born and Emil Wolf. *Principles of Optics: Electromagnetic Theory of Propagation, Interference and Diffraction of Light.* Cambridge Univ. Press, Cambridge, United Kingdom, 7. (expanded) edition, 1999. 9, 12, 87

D. F. Carbon. Model atmospheres for intermediate- and late-type stars. *Ann. Rev. Astron. Astrophys.*, 17:513–549, 1979. 60

G. Chagnon et al. L'-band interferometric observations of evolved stars. *Astronom. J.*, 2002. accepted July 2002. 69

M. A. Chamberlain et al. Mid-Infrared Observing Conditions at the South Pole. *Astrophys. J.*, 535:501–511, May 2000. 82

O. Chesneau, 2001. MPIA, private communication. 53

M. Cohen et al. Spectral Irradiance Calibration in the Infrared. X. A Self-Consistent Radiometric All-Sky Network of Absolutely Calibrated Stellar Spectra. *Astronom. J.*, 117:1864–1889, April 1999. 60

M. M. Colavita. Fringe Visibility Estimators for the Palomar Testbed Interferometer. *Publ. Astron. Soc. Pac.*, 111:111–117, January 1999. 13

M. M. Colavita et al. The Palomar Testbed Interferometer. *Astrophys. J.*, 510:505–521, January 1999. 13

V. Coudé Du Foresto, S. Ridgway, and J.-M. Mariotti. Deriving object visibilities from interferograms obtained with a fiber stellar interferometer. *Astron. Astrophys. Suppl.*, 121:379–392, February 1997. 23, 90

W. C. Danchi et al. Characteristics of dust shells around 13 late-type stars. *Astronom. J.*, 107: 1469–1513, April 1994. 68

F. Delplancke et al. Phase-referenced imaging and micro-arcsecond astrometry with the VLTI. In Léna and Quirrenbach (2000), pages 365–376. 23

F. Derie. VLTI delay lines: design, development, and performance requirements. In Léna and Quirrenbach (2000), pages 25–30. 21

F. Derie et al. VLTI test siderostats: design, development, and performance results. In Léna and Quirrenbach (2000), pages 99–103. 19

R. Donaldson et al. MACAO and its application for the VLT interferometer. In *Adaptive Optical Systems Technology, Peter L. Wizinowich; Ed.*, volume 4007 of *SPIE Proceedings Series*, pages 82–93, July 2000. 22

B. T. Draine and H. M. Lee. Optical properties of interstellar graphite and silicate grains. *Astrophys. J.*, 285:89–108, October 1984. 68

C. W. Engelke. Analytic approximations to the 2-60 microns infrared continua for standard calibration stars - With application to the calibration of spectroscopy and photometry, and the determination of effective temperature and angular size from IR measurements. *Astronom. J.*, 104:1248–1259, September 1992. 60

ESO. Astroclimatology of Paranal, 1999. URL `http://www.eso.org/gen-fac/pubs/astclim/paranal/`. 26

ESO. VLTI General Description and Tutorials, 2001. URL `http://www.eso.org/projects/vlti/general/`. 22

ESO. Outreach Activities, 2002. URL `http://www.eso.org/outreach/`. 19, 20, 21

David Finley and R. Miller Goss, editors. *Radio Interferometry: The Saga and the Science*, Workshop Number 27, Charlottesville, VA, USA, 2000. National Radio Astronomy Observatory. 2

A.-H.-L. Fizeau. In *Comptes Rendus Hebdomadaires des Séances de l'Academie des Sciences*, volume 66, pages 932–934. 1868. reprint in Lawson (1997). 1

A. Glazenborg et al. Optical design of the cold bench. Technical Report VLT-TRE-MID-15821-0101, Issue 2.0, MIDI Consortium to ESO, July 1999. 45

A. Glindemann, 2002. ESO, private communication. 26

A. Glindemann, S. Hippler, T. Berkefeld, and W. Hackenberg. Adaptive Optics on Large Telescopes. *Experimental Astronomy*, 10:5–47, April 2000. 26

P. Gondoin et al. Darwin ground-based European nulling interferometer experiment (GENIE). In *Interferometry for Optical Astronomy II, W. A. Traub; Ed.*, volume 4838 of *SPIE Proceedings Series*, August 2002. 24

I. S. Gradshteyn and M. Ryzhik. *Table of Integrals, Series, and Products*. Academic Press, San Diego London, 6th edition, 2000. 87

Arsen R. Hajian and J. Thomas Armstrong. A Sharper View of the Stars. *Scientific American*, March 2001. 2

D. D. S. Hale et al. The Berkeley Infrared Spatial Interferometer: A Heterodyne Stellar Interferometer for the Mid-Infrared. *Astrophys. J.*, 537:998–1012, July 2000. 2, 68

R. Hanbury Brown et al. The angular diameters of 32 stars. *Mon. Not. R. Astr. Soc.*, 167: 121–136, April 1974. reprint in Lawson (1997). 10

R. Hanbury Brown and R. Q. Twiss. A Test of a New Type of Stellar Interferometer on Sirius. *Nature*, 178:1046–1048, 1956a. reprint in Lawson (1997). 2

R. Hanbury Brown and R. Q. Twiss. Correlation Between Photons in two Coherent Beams of Light. *Nature*, 177:27–29, 1956b. reprint in Lawson (1997). 2

Eugene Hecht. *Optics*. Addison-Wesley, Reading, Mass., USA, 3. edition, 1998. 48, 86, 87

Albert Van Helden. Introduction to Sidereus Nuncius, 1995. URL `http://es.rice.edu/ES/humsoc/Galileo/`. 1

P. Kervella et al. Thermal Light Sources for MIDI. Change Request VLT-CRE-ESO-15810-1966, January 2000a. 48

P. Kervella et al. VINCI: the VLT Interferometer commissioning instrument. In Léna and Quirrenbach (2000), pages 31–42. 22, 48

B. Koehler. VLT Unit Telescope suitability for interferometry: first results from acceptance tests on subsystems. In *Astronomical Interferometry, Robert D. Reasenberg; Ed.*, volume 3350 of *SPIE Proceedings Series*, pages 403–413, July 1998. 17

B. Koehler and C. Flebus. VLTI auxiliary telescopes. In Léna and Quirrenbach (2000), pages 13–24. 17

B. Koehler, Ph. Gitton, et al. Interface Control Document between VLTI and its Instruments. Technical Report VLT-ICD-ESO-15000-1826, Issue 3.0, ESO, January 2002. 17, 21, 22, 23, 26, 81

R. L. Kurucz. Model atmospheres for G, F, A, B, and O stars. *Astrophys. J. Suppl.*, 40:1–340, May 1979. 61

A. Labeyrie. Interference fringes obtained on VEGA with two optical telescopes. *Astrophys. J.*, 196:L71–L75, March 1975. reprint in Lawson (1997). 2

Peter R. Lawson, editor. *Selected Papers on Long Baseline Stellar Interferometry*, volume MS 139 of *SPIE Milestone Series*. SPIE, Bellingham, WA, USA, 1997. 102, 103, 104

Peter R. Lawson, editor. *Principles of Long Baseline Stellar Interferometry*. Number 00-009 07/00 in JPL Publication. NASA/JPL, Michelson Fellowship Program, 2000. URL `http://sim.jpl.nasa.gov/library/coursenotes.html`. 5, 101, 106

C. Leinert et al. 10-μm interferometry on the VLTI with the MIDI instrument: a preview. In Léna and Quirrenbach (2000), pages 43–53. 27

Ch. Leinert. Updated sensitivity estimates for MIDI. Specification VLT-SPE-MID-15828-0111, Issue 2.0, MIDI internal document, September 1999. 82

Ch. Leinert et al. The mid-infrared interferometric instrument for the VLTI. Study group report MIDI-GD-01/1-1997, MIDI Consortium to ESO, July 1997. 26

Pierre Léna, François Lebrun, and François Mignard. *Observational Astrophysics.* Astronomy and Astrophysics Library. Springer-Verlag, Berlin Heidelberg New York, 2., rev. and enl. edition, 1998. 25, 81

Pierre J. Léna and Andreas Quirrenbach, editors. *Interferometry in Optical Astronomy*, volume 4006 of *SPIE Proceedings Series*, Washington, D.C., USA, July 2000. SPIE. 2, 101, 102, 103, 105, 106

B. Lopez et al. Radiative transfer in axisymmetric circumstellar dust shells. *Astron. Astrophys.*, 296:752+, April 1995. 68

B. Lopez et al. Nonspherical Structures and Temporal Variations in the Dust Shell of O Ceti Observed with a Long Baseline Interferometer at 11 Microns. *Astrophys. J.*, 488:807+, October 1997. 68

S. D. Lord. Gemini observatory observing condition. Technical Memor. 103957, NASA, 1992. refered to by ESO, 1999, URL `http://www.eso.org/gen-fac/pubs/astclim/paranal/h2o/`. 25

F. Martin et al. Optical parameters relevant for High Angular Resolution at Paranal from GSM instrument and surface layer contribution. *Astron. Astrophys. Suppl.*, 144:39–44, 2000. 26

R. J. Mathar et al. Instrument Control Software. Technical Report VLT-TRE-MID-15823-0128, Issue 2.1, MIDI Consortium to ESO, November 2001. 35

B. Mennesson et al. Thermal infrared stellar interferometry using single-mode guided optics: first results with the TISIS experiment on IOTA. *Astron. Astrophys.*, 346:181–189, June 1999. 68

B. Mennesson et al. Evidence for very extended gaseous layers around O-rich Miras and M giants. *Astrophys. J.*, 2002. accepted July 2002. 75

A. A. Michelson. Measurement of Jupiter's Satellites by Interference. *Publ. Astron. Soc. Pac.*, 3:274–278, September 1891. reprint in Lawson (1997). 1

A. A. Michelson and F. G. Pease. Measurement of the diameter of alpha Orionis with the interferometer. *Astrophys. J.*, 53:249–259, May 1921. reprint in Lawson (1997). 1

MIDI Science Group. MIDI Guarantied Time Observations, Abstracts and Source List. Technical Report VLT-SCI-MID-15820-0200, Issue 1.0, MIDI Consortium to ESO, November 2001. 68

C. Morossi et al. Cool Stars - Spectral Energy Distributions and Model Atmosphere Fluxes. *Astron. Astrophys.*, 277:173–183, September 1993. 60, 61

G. Niccolini et al. *Astron. Astrophys.*, 2002. submitted June 2002. 68

OLBIN. Optical Long Baseline Interferometry News, 2002. URL `http://olbin.jpl.nasa.gov/`. 2

Francesco Paresce, editor. *Science with the VLT Interferometer.* Springer-Verlag, Berlin Heidelberg New York, 1997. 24

G. Perrin. Subtracting the photon noise bias from single-mode optical interferometers visibilities. *Astron. Astrophys.*, 2002. submitted June 2002. 90, 92

G. Perrin, V. Coude Du Foresto, S. T. Ridgway, J.-M. Mariotti, W. A. Traub, N. P. Carleton, and M. G. Lacasse. Extension of the effective temperature scale of giants to types later than M6. *Astron. Astrophys.*, 331:619–626, March 1998. 23, 70, 90

G. Perrin et al. Interferometric observations of R Leonis in the K band. First direct detection of the photospheric pulsation and study of the atmospheric intensity distribution. *Astron. Astrophys.*, 345:221–232, May 1999. 69, 70

G. Perrin et al. Interferometric observations of α Orionis and α Herculis with FLUOR at IOTA. 2002a. in preparation. 69, 70

G. Perrin et al. Interferometric observations of the semi-regular variable star SW Virginis in the K band. *Astron. Astrophys.*, 2002b. submitted June 2002. 69

R. G. Petrov et al. AMBER: the near-infrared focal instrument for the Very Large Telescope Interferometer. In Léna and Quirrenbach (2000), pages 68–79. 23

E. Pitz, 2000. MPIA, private communication. 50

I. L. Porro et al. Visibility budget for the MIDI instrument. Technical Report VLT-TRE-MID-15820-0109, MIDI Consortium to ESO, July 1999. 81

Irene L. Porro et al. Simulation of the Effects of Atmospheric Turbulence on Mid-Infrared Visibility Measurements with the Mid-Infrared Interferometric Instrument for the Very Large Telescope Interferometer. *Applied Optics-OT*, 39(10):1643–1651, April 2000. 27

W. H. Press, Teukolsky S. A., and W. T. Vetterling. *Numerical Recipes in C.* Cambridge University Press, 2nd edition, 1999. 90

F. Przygodda, 2001. MPIA, private communication. 12, 32, 48, 51

F. Przygodda and P. Schuller. MIDI Laser Table – Assembly and Alignment. Technical Report VLT-PRO-MID-15821-0231, Issue 1.0, MIDI Consortium to ESO, July 2002. 93

A. Quirrenbach. Optical Interferometry. *Ann. Rev. Astron. Astrophys.*, 39:353–401, 2001. 2

A. Quirrenbach et al. Angular diameter measurements of cool giant stars in strong TiO bands and in the continuum. *Astrophys. J.*, 406:215–219, March 1993. 60

A. Richichi and G. Calamai. Infrared high angular resolution measurements of stellar sources. V. Angular diameters of ten late-type stars. *Astron. Astrophys.*, 380:526–532, December 2001. 59

A. Richichi and I. Percheron. CHARM: A Catalog of High Angular Resolution Measurements. *Astron. Astrophys.*, pages 492–503, 2002. 59

M. Robberto and T. M. Herbst. MAX: the new MPIA thermal infrared imager. In *Proc. SPIE Vol. 3354, pages 711-719, Infrared Astronomical Instrumentation, Albert M. Fowler; Ed.*, August 1998. 27

M. Ryle. A new radio interferometer and its application to the observation of weak radio stars. *Proc. Roy. Soc.*, A211:351–375, 1952. 2

Bernhard Schrader, editor. *Infrared and Raman Spectroscopy.* Wiley-VCH, Weinheim, 1995. 51

P. Schuller et al. Safety and Hazard Handling. Technical Report VLT-TRE-MID-15822-0126, Issue 2.0, MIDI Consortium to ESO, July 2000. 43, 46

SIMBAD. SIMBAD Astronomical Database, 2002. URL `http://simbad.u-strasbg.fr/`. 62, 65

C. H. Smith and D. A. Harper. Mid-Infrared Sky Brightness Site Testing at the South Pole. *Publ. Astron. Soc. Pac.*, 110:747–753, June 1998. 81, 82

A. Richard Thompson, James M. Moran, and George W. Swenson. *Interferometry and Synthesis in Radioastronomy.* John Wiley & Sons, New York, NY, USA, 2nd edition, 2001. 2

W. A. Traub et al. Third telescope project at the IOTA interferometer. In Léna and Quirrenbach (2000). 61

Wesley A. Traub. Beam Combination and Fringe Measurement. 2000. In Lawson (2000). 8

Robert K. Tyson. *Principles of Adaptive Optics.* Academic Press, Boston London, 2nd edition, 1998. 25, 85

VDI. *5th International Symposium on Gas Analysis by Tunable Diode Lasers*, number 1366 in VDI-Berichte, 1998. VDI/VDE-Gesellschaft Meß- und Automatisierungstechnik, VDI-Verlag. Symposium held in Freiburg/Germany, 25th/26th February 1998. 47

T. Verhoelst, 2002. Catholic University of Leuven, in preparation. 61

O. von der Lühe et al. The warm optics for MIDI. Technical Report VLT-TRE-MID-15821-0106, MIDI Consortium to ESO, July 1999. 45

A. Wallander et al. Commissioning VLT unit telescopes: methods and results. In *Telescope Structures, Enclosures, Controls, Assembly/Integration/Validation, and Commissioning, Thomas A. Sebring; Torben Andersen; Eds.*, volume 4004 of *SPIE Proceedings Series*, pages 234–245, August 2000. 17

J. Weiner et al. Precision Measurements of the Diameters of α Orionis and o Ceti at 11 Microns. *Astrophys. J.*, 544:1097–1100, December 2000. 76

L. A. Willson. Mass Loss From Cool Stars: Impact on the Evolution of Stars and Stellar Populations. *Ann. Rev. Astron. Astrophys.*, 38:573–611, 2000. 75

Abbreviations and Acronyms

ADC	Analog Digital Converter.
AGB	Asymptotic Giant Branch.
AGN	Active Galactic Nuclei.
AMBER	Astronomical Multiple BEam Recombiner.
AO	Adaptive Optics.
ARAL	ARtificial star and ALignment toolkit.
AT	Auxiliary Telescope.
CCC	Closed Cycle Cooler.
CCD	Charge-Coupled Device.
CONICA	COudé Near-Infrared CAmera.
DAC	Digital Analog Converter.
DC	Direct Current.
DDL	Differential Delay Line.
DL	Delay Line.
ESA	European Space Agency.
ESO	European Southern Observatory.
FINITO	Fringe-tracking Instrument of NIce and TOrino.
FLUOR	Fiber Linked Unit for Optical Recombination.
FOV	Field Of View.
FWHM	Full Width at Half Maximum.
GENIE	Ground-based European Nulling Interferometer Experiment.
HIPPARCOS	HIgh Precision PARallax COllecting Satellite.
IDL	Internal Delay Line.
IOTA	Infrared-Optical Telescope Array.
ISI	Infrared Spatial Interferometer.
LSB	Least Significant Bit.
MACAO	Multiple Application Curvature Adaptive Optics.
MCC	MIDI Calibrator Candidate.

MIDI	MID-infrared Interferometric Instrument.
MPIA	Max-Planck-Institut für Astronomie.
OPD	Optical Path Difference.
P66, P67	the two piezo translation stages.
PC	Personal Computer.
PRIMA	Phase-Referenced Imaging and Microarcsecond Astrometry.
PTI	Palomar Testbed Interferometer.
RMS	Root Mean Square.
SED	Spectral Energy Distribution.
SIM	Space Interferometry Mission.
SNR	Signal to Noise Ratio.
STRAP	System for Tip-tilt Removal with Avalanche Photodiodes.
TIMMI	Thermal Infrared Multimode Instrument.
UD	Uniform Disk.
UT	Unit Telescope.
VINCI	VLT INterferometer Commissionning Instrument.
VISIR	VLT Imager and Spectrometer for the mid-InfraRed.
VLT	Very Large Telescope.
VLTI	Very Large Telescope Interferometer.
VME	Virtual Machine Environment.
YSO	Young Stellar Objects.

At the end ...

... I would like to say to all those who were involved, one way or the other, in the realisation of my thesis: „Danke“, “Thank you”, ≪ Merci ≫, “Grazie”, “Dank u” usw.

Prof. Christoph Leinert took me on board the Heidelberg MIDI team. This gave me the opportunity to work with this exciting project and – even through difficult times (!) – to be part of it almost until completion. The cooperation of all those involved, including our French and Dutch partners, was very instructive. (Proverbs 15:22)

My colleagues at the Max-Planck-Institut für Astronomie were a “(data) base” in many respects. In conversations, discussions, and very practical situations they aided me a lot. I would like especially to mention the staff of the mechanic and electronic workshops and of the technical service who informally and often “just quickly” drilled, wired, or moved something for me. Inspiring conversations were possible with Dr. Eckhart Pitz in “his” Black Laboratory, he shared many insights from his experience. I thank the PhD Advisory Committee represented by Dr. Tom Herbst for advice and insight about the “thesis project” and the time thereafter. (Proverbs 11:14)

Prof. Christoph Leinert and Prof. Wolfgang Duschl kindly agreed to referee my thesis. I thank also Prof. Roland Wielen and Prof. Bernd Jähne as jury members at the defence. (Proverbs 15:23)

Parts of this thesis were made possible by the kind support of external institutions. I thank the companies Bayer AG (Leverkusen), profol GmbH (Halfing), BASF AG (Ludwigshafen), and Röhm GmbH (Darmstadt) for the provision of samples of their polymer foils. The transmission measurements were carried out at the Chemical and Spectroscopical Laboratory at the Astrophysical Institute of the University of Jena, Germany. A Marie Curie Fellowship of the European Commission at the Observatoire Paris-Meudon, France, allowed me to write significant parts of the astrophysical chapter. (Proverbs 3:28)

The stay in Meudon was very enriching. Beginning with the first day, I felt I was part of the FLUOR team at ≪ Table Equatoriale ≫ and could make the first steps into the wonderful world of interferometry and its application in astrophysics. I learned a lot from inspiring discussions. Going together to the canteen and the joint ≪ tea-tim_e ≫ were enjoyable – ≪ c’était vachement cool_e ≫ ! Furthermore, Philippe Salomé from the Observatoire Paris helped me get started with using the modeling code. I received a lot of support from the colleagues in Nice, France, at the Observatoire de la Côte d’Azur. Gilles Niccolini, in particular, was often at the “hotline” and solved many problems from a distance. (Proverbs 1:5)

Many people in my private environment aided and helped me with advice and action, encouragement and admonition, and in material as well as non-material ways:

A number of (former and current) people from my home town did not loose sight of me. Especially in the last phase of my thesis they repeatedly encouraged me, be it by e-mail or by asking directly. My long-time friends Joachim Maier und Markus Hartung assisted many times when it was up to sorting out things of mind or spirit. This was a relief. (2 Kings 4:10)

My "fellow monks" Burkhard Stetter und "Kalle" Schneider not only took care that there was always a bite to eat when I came home at nightly hours. Together with several other former residents of the Friedrich-Hauß-Studienzentrum (a student residence), Schriesheim, they continue to affect my life positively. Also, I would like to mention Inga Neumann who, several times, had to dance with a partner only partly mentally present. (Proverbs 16:24)

Recently, there has been a young lady who enlightened my evening work sessions with her phone calls. Our weekends together were quite restricted recently, but there is a life after the thesis when this will hopefully improve again. (Proverbs 15:30)

My immediate family supported me during all this time in many ways. Even if the geographic distance complicated things, I got a lot of help – from purchasing nice CDs on demand to sponsoring the vehicle. (Proverbs 19:20)

Most of all, I thank Him. (Psalm 136:1)

Zum Schluß ...

... möchte ich allen sagen, die an der Durchführung meiner Doktorarbeit mittelbar und unmittelbar beteiligt waren: „Danke“, “Thank you”, ≪ Merci ≫, “Grazie”, “Dank u” usw.

Prof. Christoph Leinert nahm mich in die Heidelberger MIDI-Mannschaft auf. Dies gab mir die Möglichkeit, mit Beginn der praktischen Arbeiten an diesem spannenden Projekt mitarbeiten und es – auch über manche schwierige Strecke hinweg (!) – fast bis zur Vollendung begleiten zu können. Die Zusammenarbeit der Beteiligten am Projekt, einschließlich unserer französischen und holländischen Partner, war sehr lehrreich. (Sprüche 15, 22)

Meine Kollegen am Max-Planck-Institut für Astronomie waren eine „(Daten-)Bank“ in mancher Hinsicht. Sie haben mir immer wieder in Gesprächen, Diskussionen und ganz praktisch hilfreich zur Seite gestanden. Besonders erwähnen möchte ich die Mitarbeiter der Mechanischen und Elektronischen Werkstätten sowie des Technischen Dienstes, die mir oft in unkomplizierter Weise „g’schwind mal eben schnell“ etwas gebohrt, verdrahtet oder verschoben haben. Sehr anregende Gespräche konnte ich mit Herrn Dr. Eckhart Pitz in „seinem“ Schwarzen Labor führen, er vermittelte mir mache Erkenntnis aus seinem Erfahrungsschatz. Dem PhD Advisory Committee in Person von Dr. Tom Herbst sei gedankt für manche Ratschläge und Einsichten zum „Projekt Doktorarbeit“ und der Zeit danach. (Sprüche 11, 14)

Prof. Christoph Leinert und Prof. Wolfgang Duschl übernahmen freundlicherweise die Begutachtung meiner Doktorarbeit. Ebenso danke ich Prof. Roland Wielen und Prof. Bernd Jähne als Prüfern bei der Disputation. (Sprüche 15, 23)

Teile dieser Arbeit wurden durch die freundliche Unterstützung auswärtiger Einrichtungen ermöglicht. Den Unternehmen Bayer AG (Leverkusen), profol GmbH (Halfing), BASF AG (Ludwigshafen) und Röhm GmbH (Darmstadt) sei gedankt für die Überlassung von Proben ihrer Polymerfolien. Die Transmissionsmessungen daran wurden am Chemischen und Spektroskopischen Labor des Astrophysikalischen Instituts der Universität Jena durchgeführt. Ein Marie-Curie-Stipendium der Europäischen Kommission am Observatoire Paris-Meudon, Frankreich, erlaubte die Erarbeitung großer Teile des astrophysikalischen Kapitels. (Sprüche 3, 28)

Der Aufenthalt in Meudon war überaus bereichernd. Vom ersten Tag an fühlte ich mich als Teil der FLUOR-Gruppe im ≪ Table Equatoriale ≫ und konnte dabei erste Schritte tun in die wunderbare Welt der Interferometrie und deren Anwendung auf die Astrophysik. Bei anregenden Diskussionen habe ich viel gelernt. Die gemeinsamen Kantinengänge und die ≪ tea-tim_*e* ≫ habe ich genossen – ≪ c’était vachement cool_*e* ≫ ! – Darüber hinaus hat mir Philippe Salomé vom

Observatoire Paris beim Einstieg in die Nutzung des Modellierungprogramms geholfen. Sehr viel Unterstützung habe ich erhalten durch die Kollegen in Nizza, Frankreich, am Observatoire de la Côte d'Azur. Besonders Gilles Niccolini war oft an der „Hotline“ und hat viele Probleme auf die Entfernung gelöst. (Sprüche 1, 5)

Viele Menschen in meinem persönlichen Umfeld standen mir in dieser Zeit mit Rat und Tat, aufmunternden und auch ermahnenden Worten sowie in materieller und ideeller Weise zur Seite und waren mir behilflich:

Einige Korntaler und Münchinger (jetzige und ehemalige) haben mich nicht aus den Augen verloren. Gerade in der letzten Phase der Doktorarbeit haben sie mich immer wieder aufgemuntert, sei es per E-Mail oder durch Nachfragen. Meine Freunde Joachim Maier und Markus Hartung waren mir manches Mal eine Hilfe in Dingen des Geistes und der Seele, wenn es galt, diese ein wenig zu sortieren. Das hat gut getan. (2. Könige 4, 10)

Meine „Mitmönche“ Burkhard Stetter und „Kalle“ Schneider sorgten nicht nur dafür, daß es immer eine Kante Brot zum Beißen gab, wenn ich zu nächtlicher Stunde nach Hause kam. Zusammen mit etlichen anderen Ehemaligen des Friedrich-Hauß-Studienzentrum (FHSZ), Schriesheim, berühren sie weiterhin positiv mein Leben. Erwähnen möchte ich auch Inga Neumann, die einige Male mit einem geistig nur halb anwesenden Partner tanzen mußte. (Sprüche 16, 24)

Seit einiger Zeit gibt es eine junge Dame, die mit ihren Anrufen mir die abendlichen Arbeitssitzungen erhellt hat. Unsere gemeinsamen Wochenenden sind zuletzt recht eingeschränkt gewesen, aber es gibt ja auch ein Leben nach der Doktorarbeit, in dem das hoffentlich wieder besser wird. (Sprüche 15, 30)

Mein engster Familienkreis hat mich die gesamte Zeit über vielfach unterstützt. Auch wenn die räumliche Entfernung vieles schwieriger machte, so konnte ich trotzdem manche Hilfe erfahren – vom Kauf netter CDs auf Bestellung bis zum Unterhalt des fahrbaren Untersatzes. (Sprüche 19, 20)

Mein größter Dank aber gilt Ihm. (Psalm 136, 1)

In scarce words:
“The writing of many books is endless,
and excessive devotion to books
is wearying to the body.”
(The Bible, Ecclesiastes 12:12)

Ohne viele Worte:
„Des vielen Büchermachens ist kein Ende,
und viel Studieren macht den Leib müde.“
(Die Bibel, Prediger 12, 12)